ATLAS CONF Note

ATLAS-CONF-2023-052

26th August 2023

Interpretations of the ATLAS measurements of Higgs boson production and decay rates and differential cross-sections in pp collisions at $\sqrt{s} = 13$ TeV

The ATLAS Collaboration

Measurements of the Higgs boson production and decay rates and differential cross-sections have recently been performed by the ATLAS experiment in several decay channels using up to 139 fb^{-1} of proton–proton collision data at $\sqrt{s} = 13$ TeV recorded at the Large Hadron Collider. This note presents multiple interpretations of these Higgs boson measurements. Measurements of production-mode cross-sections, simplified template cross-sections or fiducial differential cross-sections in different decay channels are reparameterised in terms of the impact of Standard Model Effective Field Theory operators, and constraints are reported on the corresponding Wilson coefficients. Production and decay rate measurements are interpreted in UV-complete extensions of the Standard Model, namely the two-Higgs-doublet model (2HDM) near the alignment limit and the Minimal Supersymmetric Standard Model (MSSM) for various MSSM benchmark scenarios. The constraints on the 2HDM parameters $(\cos(\beta-\alpha), \tan\beta)$ and the MSSM parameters $(m_A, \tan\beta)$ are complementary to those obtained from direct searches for additional Higgs bosons.

ATLAS-CONF-2023-052
13 September 2023

Contents

1 Introduction

Since a particle (H) with attributes consistent with those of the Higgs boson [1–6] of the Standard Model (SM) of particle physics was discovered [7, 8] by the ATLAS and CMS experiments, its properties have been measured with proton–proton (pp) collision data produced by the Large Hadron Collider (LHC) at CERN. The ATLAS collaboration recently presented its first results on the combination of Higgs boson production and decay rate measurements with up to 139 fb^{-1} of 13 TeV pp collision data [9], collected during the full LHC Run 2 in the years 2015 through 2018. Two interpretations of these measurements are presented here. The first one is based on an Effective Field Theory (EFT) framework of the Standard Model. The second interpretation relies on specific theories that provide ultraviolet completions of the SM, specifically several benchmark scenarios within the two-Higgs doublet model (2HDM) [10–13] or within a minimal supersymmetric extension of the Standard Model (MSSM) [14–18].

In addition to the production and decay rates mentioned above, the fiducial differential cross-sections for Higgs boson production as a function of selected event kinematics have been measured by the ATLAS collaboration with the same dataset in the $H \to ZZ^* \to 4\ell$ ($\ell = e, \mu$) [19] and $H \to \gamma\gamma$ [20] decay channels, among others [21, 22]. The fiducial differential cross-sections measured as a function of the total transverse momentum[1] of the Higgs boson decay products in the two decay channels, $p_{\text{T}}^{4\ell}$ and $p_{\text{T}}^{\gamma\gamma}$, are used in this note to constrain anomalous Higgs boson couplings to gluons and top quarks, and an anomalous Higgs-gluon-top-antitop quark coupling, within the same EFT framework. These couplings are also probed using the EFT interpretation of Higgs boson production and decay rate measurements; the sensitivities obtained with the two approaches are compared.

Effective field theories provide a model-independent approach, systematically improvable with higher-order perturbative calculations, to parametrise the effects of candidate theories beyond the Standard Model (BSM) that reduce to the Standard Model at low energies. In the SM Effective Field Theory (SMEFT), the effects of BSM dynamics at energy scales Λ that are large in comparison to the vacuum-expectation-value (vev) v of the SM Higgs field ($\Lambda \gg v$) can be parametrised at low energies, $E \ll \Lambda$, in terms of higher-dimensional operators that are built up from the Standard Model fields and respect its symmetries. Measurements of (fiducial) cross-sections can be used to place constraints on the Wilson coefficients associated with the SMEFT operators, corresponding to limits on BSM physics at some fixed scale Λ.

The methodology employed here for the EFT interpretation of the combined measurements of Higgs boson production and decay rates is similar to the one used by the individual analyses. The interpretation is applied in this note to the combined measurements of the Higgs boson production cross-sections times branching ratios in the following decay channels: $H \to ZZ^*(\to 4\ell)$, $H \to \gamma\gamma$, $H \to b\bar{b}$, $H \to \tau\tau$, $H \to WW^*(\to e\nu\mu\nu)$, $H \to Z\gamma$, and $H \to \mu\mu$ [23–33].

A similar approach is used for the interpretation of the fiducial p_{T}-differential cross-sections in the $H \to ZZ^* \to 4\ell$ and $H \to \gamma\gamma$ channels. The method resembles closely that described in Ref. [20] for the joint interpretation of five differential cross-sections in the $H \to \gamma\gamma$ decay channel in terms of a few dimension-6 SMEFT operators, but only the cross-section measurements as a function of $p_{\text{T}}^{4\ell}$ and $p_{\text{T}}^{\gamma\gamma}$ are

[1] ATLAS uses a right-handed coordinate system with its origin at the nominal interaction point (IP) in the centre of the detector and the z-axis along the beam pipe. The x-axis points from the IP to the centre of the LHC ring, and the y-axis points upwards. Cylindrical coordinates (r, ϕ) are used in the transverse plane, ϕ being the azimuthal angle around the z-axis. The pseudorapidity is defined in terms of the polar angle θ as $\eta = -\ln\tan(\theta/2)$. Angular distance is measured in units of $\Delta R \equiv \sqrt{(\Delta\eta)^2 + (\Delta\phi)^2}$. The tranverse momentum p_{T} is the momentum component in the transverse plane.

used, and a smaller number of operators is probed. On the other hand, the joint interpretation with a second decay channel with similar statistical precision increases the sensitivity to the probed BSM operators.

In the interpretations presented in the second part of this note, performed in the context of UV-complete BSM theories, two additional measurements of production and decay rates, based on a partial Run 2 dataset collected in the years 2015 and 2016, are considered: $H \to WW^*$ in the WH and ZH production modes [34], and $H \to$ multileptons in the $t\bar{t}H$ production mode [35]. In a previous publication [36], measurements were interpreted within the hMSSM model [37] in terms of constraints on the mass of the neutral CP-odd boson A (m_A) and on the ratio of the vevs of the Higgs doublets ($\tan\beta$). The use of this model as a benchmark MSSM scenario suffers from theoretical limitations in regions with small m_A or large $\tan\beta$ because its assumptions may not hold in these regions of parameter space [38]. In this note, in addition to the hMSSM model, seven more recent benchmark MSSM scenarios [38, 39] are tested. These include two new scenarios [39] that were recently designed to be compatible with a low value of $\tan\beta$ (< 10). This parameter space region is otherwise excluded in most MSSM scenarios, which predict for $\tan\beta \lesssim 10$ a mass of the lightest neutral Higgs boson significantly lower than the observed Higgs boson mass of 125.09 ± 0.24 GeV [40]. In addition, an interpretation in terms of the parameters $\tan\beta$ and $\cos(\beta-\alpha)$ of the 2HDM near the alignment limit, in which the light neutral Higgs boson of the 2HDM is SM-like, is also reported. These constraints are compared with those inferred from the limits on the SMEFT Wilson coefficients after matching the 2HDM parameters to the SMEFT operators.

The note is structured as follows. Section 2 gives an overview of the Higgs boson production-mode cross-sections and decay rate measurements and of the fiducial differential cross-section measurements that are used to derive the results presented. Section 3, devoted to the EFT interpretation of the measurements, starts with a description of the general approach of deriving limits on Wilson coefficients (Section 3.1). This is followed by the details of the specific choices of Wilson coefficients probed in the interpretations of the combined measurements of Higgs boson production-mode cross-sections and decay rates (Section 3.2) or of the measurements of the fiducial differential cross-sections as a function of p_{T}^{H} (Section 3.3), together with the corresponding constraints. The interpretations in UV-complete extensions of the Standard Model are detailed in Section 4. The approach taken to interpret the Higgs boson production-mode cross-sections and decay rate measurements in terms of constraints on the parameters of the 2HDM or the MSSM, and the derived results, are described in Sections 4.1 and 4.2, respectively. Finally, Section 5 presents the conclusions.

2 Measurements of Higgs boson cross-sections

2.1 Data samples

The results presented in this note are based on pp collision data collected by the ATLAS experiment [41–43] in the years 2015 to 2018, with the LHC operating at a centre-of-mass energy of 13 TeV. The decay channels, targeted production modes and integrated luminosity of the dataset used in each input analysis are summarised in Table 1, where the measurements labeled 'STXS' are identical to those used in Ref. [9]. The uncertainty on the combined 2015–2018 integrated luminosity is 1.7%. It is derived from the calibration of the luminosity scale using x–y beam-separation scans, following a methodology similar to that detailed in Ref. [44], and using the LUCID-2 detector [45] for the baseline luminosity measurements.

Table 1: The decay channels (1st column), targeted production modes (2nd column) and integrated luminosity $\mathcal{L}$ (3rd column) of the dataset used for each analysis included in the combined measurements of Higgs boson production and decay rates, couplings and simplified template cross-sections (labeled as 'STXS' in the 'Binning' column), or in the measurements of fiducial p_{T}-differential cross-sections (labeled as 'differential' in the 'Binning' column). The references for the input analyses (5th column) and information about which input analyses are considered for the SMEFT-based interpretation (6th column) and the interpretations in terms of UV-complete models (7th column) are also provided. The definitions of the binning for the measurements and the corresponding signal yield parametrizations are detailed in Section 2.3. In all the analyses, the tiny expected contribution from associated $b\bar{b}H$ production is applied as a correction to ggF as described in the text.

Decay channel	Analysis / Production mode	$\mathcal{L}$ [fb^{-1}]	Reference	Binning	SMEFT	2HDM and (h)MSSM
$H \to \gamma\gamma$	(ggF, VBF, WH, ZH, $t\bar{t}H$, tH)	139	[24]	STXS-1.2	✓	✓
			[20]	differential	✓(subset)	
$H \to ZZ^*$	($ZZ^* \to 4\ell$: ggF, VBF, $WH+ZH$, $t\bar{t}H+tH$)	139	[23]	STXS-1.2	✓	✓
			[19]	differential	✓(subset)	
	($ZZ^* \to \ell\ell\nu\bar{\nu}/\ell\ell q\bar{q}$: $t\bar{t}H$ multileptons)	36.1	[35]	STXS-0*		✓
$H \to \tau\tau$	(ggF, VBF, $WH+ZH$, $t\bar{t}H+tH$)	139	[30]	STXS-1.2	✓	✓
	($t\bar{t}H$ multileptons)	36.1	[35]	STXS-0*		✓
$H \to WW^*$	(ggF, VBF)	139	[31]	STXS-1.2	✓	✓
	(WH, ZH)	36.1	[46]	STXS-0*		✓
	($t\bar{t}H$ multileptons)	36.1	[35]	STXS-0*		✓
$H \to b\bar{b}$	(WH, ZH)	139	[25, 26]	STXS-1.2	✓	✓
	(VBF)	126	[27]	STXS-1.2	✓	✓
	($t\bar{t}H+tH$)	139	[29]	STXS-1.2	✓	✓
	(boosted Higgs bosons: inclusive production)	139	[28]	STXS-1.2	✓	✓
$H \to Z\gamma$	(inclusive production)	139	[32]	STXS-0*	✓	✓
$H \to \mu\mu$	(ggF + $t\bar{t}H$ + tH, VBF + WH + ZH)	139	[33]	STXS-0*	✓	✓

2.2 Simulation of the Standard Model signal

Monte Carlo (MC) simulated event samples of SM Higgs bosons produced in pp collisions and decaying to the final states considered in this study are generated and normalised to SM predictions calculated for a Higgs boson mass $m_H = 125.09$ GeV. For each Higgs boson decay mode, the branching ratio that is used corresponds to the theoretical calculation at the highest available order of accuracy in perturbation theory [47]. All analyses except $H \to b\bar{b}$ (VBF) use a consistent set of Higgs boson signal samples as described in the following paragraphs. The samples used for $H \to b\bar{b}$ (VBF) are described separately at the end of this section.

Higgs boson production via gluon-gluon fusion is simulated using the Powheg Box [48–51] NNLOPS implementation [52, 53]. The event generator uses HNNLO [54] to reweight the inclusive Higgs boson rapidity distribution produced by the next-to-leading order (NLO) generation of $pp \to H$ + parton events, with the scale of each parton emission determined using the MiNLO procedure [55]. The PDF4LHC15 [56] parton distribution functions (PDFs) are used for the central prediction and uncertainty. The sample is

normalised such that it reproduces the total cross-section predicted by a next-to-next-to-next-to-leading-order (N^3LO) QCD calculation with NLO electroweak corrections applied [47, 57–60]. The NNLOPS generator reproduces the Higgs boson p_T distribution predicted by the NNLO plus next-to-next-to-leading logarithm (NNLL) calculation of HRES2.3 [61], which includes the effects of top- and bottom-quark masses and uses dynamical renormalization and factorization scales.

The VBF and $q\bar{q} \to VH$ ($gg \to ZH$) production processes are simulated at NLO (LO) accuracy in QCD using the POWHEG BOX [62] generator with the PDF4LHC15 set of PDFs, where the simulation of $q\bar{q} \to VH$ relies on improved NLO calculations [63]. The VBF sample is normalised to an approximate-NNLO QCD cross-section with NLO electroweak corrections applied [47, 64–66]. The VH samples are normalised to cross-sections calculated at NNLO in QCD with NLO electroweak corrections [67, 68] and additional NLO QCD corrections [69] for the $gg \to ZH$ subprocess [47].

Higgs boson production in association with a top–antitop quark pair ($t\bar{t}H$), followed by an $H \to \gamma\gamma$ or $H \to ZZ^* \to 4\ell$ decay, is simulated at NLO accuracy in QCD using the POWHEG BOX generator with the PDF4LHC15 set of PDFs. For the generation of $t\bar{t}H$ events in the other Higgs boson decay channels, the MADGRAPH5_AMC@NLO [70] generator is used with the NNPDF3.0 [71] set of PDFs. In both cases, the sample is normalised to a calculation with NLO QCD and electroweak corrections [47, 72–75].

In addition to the primary Higgs boson production modes, lower-rate processes are modeled using separate samples. For the 36 fb^{-1} analyses, Higgs boson production in association with a bottom–antibottom quark pair ($b\bar{b}H$) is simulated using MADGRAPH5_AMC@NLO [76] with the NNPDF2.3LO [77] PDFs, and it is normalised to a cross-section calculated at NNLO accuracy in QCD [47, 78–80]. The sample includes the effect of interference with the ggF production mechanism. Higgs boson production in association with a single top quark and a W boson (tHW) is produced at LO accuracy using MADGRAPH5_AMC@NLO. Finally, Higgs boson production in association with a single top quark in the t-channel (tHq) is generated at LO accuracy using MADGRAPH5_AMC@NLO with the CT10 [81] PDF set. The two tH samples are normalised to NLO QCD calculations [47, 82]. For the 139 fb^{-1} analyses, the PDF used for the $b\bar{b}H$ sample is CT10, and the tH samples are produced at NLO accuracy in QCD using the NNPDF3.0NLO PDF set.

In the VBF $H \to b\bar{b}$ analysis, the POWHEG BOX generator with the NNPDF3.0 set of PDFs is used to simulate the ggF and VBF production processes, and it is interfaced with PYTHIA8 for the modelling of the parton shower. NLO electroweak corrections are calculated using MADGRAPH5_AMC@NLO and applied as a function of the generated Higgs boson transverse momentum. Contributions from VH and $t\bar{t}H$ production are generated with the POWHEG BOX event generator with the NNPDF3.0 set of PDFs.

All parton-level events are input to PYTHIA8 [83] to model the Higgs boson decay, parton showering, hadronization, and multiple parton interactions. The generators are interfaced to PYTHIA8 using the AZNLO [84] or A14 [85] parameter sets.

Particle-level events are passed through a GEANT 4 [86] simulation of the ATLAS detector [87] and reconstructed using the same analysis software as used for the data. Event pileup is included in the simulation by overlaying inelastic pp collisions, such that the distribution of the average number of interactions per bunch crossing reproduces that observed in the data. The inelastic pp collisions are simulated with PYTHIA8 using the MSTW2008LO [88] set of PDFs with the A2 [89] set of tuned parameters, or using the NNPDF2.3LO set of PDFs with the A3 [90] set of tuned parameters.

2.3 Signal yield parametrization

In all analyses listed in Table 1, the likelihood function for each signal region k, with one or more bins r, is modeled as

$$L(\boldsymbol{N_k}|\boldsymbol{\mu},\boldsymbol{\theta}) \quad = \quad \prod_r \text{Poisson}\left(N_{k,r}|s_k(\boldsymbol{\mu},\boldsymbol{\theta})\cdot f_s^{k,r}(\boldsymbol{\theta}) \;+\; b_{k,r}(\boldsymbol{\theta})\right), \tag{1}$$

where $N_{k,r}$ is the observed event count of bin r in region k, s_k is the expected signal count in region k, $f_s^{k,r}$ is the expected fraction of the signal in region k that is contained in bin r, and $b_{k,r}$ represents the expected event count from background processes. The ensemble of *parameters of interest* $\boldsymbol{\mu}$ describes the Higgs boson signal normalisation, while $\boldsymbol{\theta}$ represents the set of *nuisance parameters* taking into account the systematic uncertainties that originate from theoretical and experimental sources, as well as additional degrees of freedom without prior constraints such as background yields or normalisations in some of the input channels. The global likelihood function is then the product of the likelihood functions for each signal region k and of Gaussian or log-normal probability density functions that constrain the nuisance parameters.

Depending on the level of detail implemented in each analysis, the signal yield parameters $\boldsymbol{\mu}$ can be indexed by Higgs boson production process (i), decay mode (X), and fiducial phase space region defined at the particle level (k'). Analysis region k, defined at the reconstruction level, is typically chosen to match the particle-level region k' as closely as possible, in order to reduce the extrapolation uncertainty. As reconstruction-level selections do not generally correspond exactly to particle-level regions, multiple particle-level regions will contribute to the signal yield s_k.

Two distinct signal parametrization strategies are followed for the measurements listed in Table 1 and reported in Eq. (2) and Eq. (3). For those labeled as 'STXS', the signal yield for region k is modeled as a scale factor $\mu_k^{i,k',X}$ applied to the SM Higgs boson production cross-section times branching ratio, for each Higgs boson production process i and decay X, in a fiducial region k' defined at the particle level. Alternatively, for analyses labeled as 'differential', the signal yield is modeled as a cross-section $\sigma_{\text{fid.}}^{k',X}$ describing the sum of all production processes, separately for each Higgs boson decay mode X and fiducial region k' defined at the particle level. The corresponding parametrizations of the signal yield s_k in terms of the parameters of interest $\boldsymbol{\mu_k} = \{\mu_k^{i,k',X}\}$ and $\boldsymbol{\sigma}_{\text{fid.}} = \{\sigma_{\text{fid.}}^{k',X}\}$ and of the nuisance parameters $\boldsymbol{\theta}$ are:

$$s_k^{\text{STXS}}(\boldsymbol{\mu_k},\boldsymbol{\theta}) \quad = \quad \mathcal{L}\times\sum_{i,k',X}\mu_k^{i,k',X}\times(\sigma\times B)^{i,k',X}_{\text{SM,(N(N))NLO}}(\boldsymbol{\theta})\times\epsilon^{i,k',X}_{\text{STXS},k}(\boldsymbol{\theta}), \tag{2}$$

$$s_k^{\text{diff.}}(\boldsymbol{\sigma}_{\text{fid.}},\boldsymbol{\theta}) \quad = \quad \mathcal{L}\times\sum_{k',X}\sigma_{\text{fid.}}^{k',X}\times\epsilon^{k',X}_{\text{diff.},k}(\boldsymbol{\theta}), \tag{3}$$

where $\mathcal{L}$ is the integrated luminosity and $(\sigma\times B)^{i,k',X}_{\text{SM,(N(N))NLO}}$ is the calculation, at the highest available order, of the SM Higgs boson cross-section for the production process i in particle-level region k' multiplied by the SM Higgs boson branching ratio to the final state X. The factors $\epsilon^{i,k',X}_{\text{STXS},k}$ and $\epsilon^{k',X}_{\text{diff.},k}$ represent the products of acceptance times efficiency of the reconstruction-level region k for the particle-level fiducial phase space region k' and Higgs boson decay X (in production mode i for the STXS interpretation).

For each interpretation based on a particular model (SMEFT, 2HDM, or MSSM) with a vector of model parameters $\boldsymbol{\alpha}$, the original signal parameters $\boldsymbol{\mu}$ and $\boldsymbol{\sigma}_{\text{fid.}}$ are replaced with expressions that parameterise the model predictions, e.g. $\sigma_{\text{fid.}}^{k',X} \rightarrow \sigma_{\text{fid.}}^{k',X}(\boldsymbol{\alpha})$, so that the likelihood of Eq. (1) is directly expressed in terms of the parameters $\boldsymbol{\alpha}$. Then, constraints on these parameters can be directly inferred from the modified likelihood expression. The model-specific reparametrizations of the signal parameters are detailed in Sections 3 and 4.

The acceptance factors ϵ_{STXS} and $\epsilon_{\text{diff.}}$, as well as the signal shape factors f_s, are derived under the assumption of SM Higgs boson kinematics. For interpretations of the measurements in physics models that significantly alter kinematic distributions, additional correction factors may be needed to account for changes in the acceptance and signal shape as a function of BSM model parameters. These are discussed when applicable in Sections 3 and 4.

2.3.1 Fiducial differential cross-section measurements

For the interpretation of fiducial differential cross-section measurements in the $H\rightarrow\gamma\gamma$ and $H\rightarrow ZZ^*\rightarrow 4\ell$ analyses, the differential distributions in the transverse momentum of the Higgs boson decay products are considered. The $H\rightarrow ZZ^*\rightarrow 4\ell$ analysis defines 9 analysis regions with boundaries in $p_{\text{T}}^{4\ell}$ at

$$\{0, 10, 20, 30, 45, 60, 80, 120, 200, 300\}\ \text{GeV},$$

whereas the $H\rightarrow\gamma\gamma$ analysis defines a finer granularity with 20 analysis regions with boundaries in $p_{\text{T}}^{\gamma\gamma}$ at

$$\{0, 5, 10, 15, 20, 25, 30, 35, 45, 60, 80, 100, 120, 140, 170, 200, 250, 300, 450, 650, 13000\}\ \text{GeV},$$

resulting in a total of 29 fiducial cross-section measurements that are interpreted in Section 3.3. Further details on these analyses, including the full definitions of the fiducial regions, can be found in Refs. [19, 20].

2.3.2 Production and decay rate and simplified template cross-section measurements

For the interpretations based on the SMEFT framework presented in Section 3, measurements of "simplified template cross-sections" (STXS) of various Higgs boson production processes in the regions of phase space defined within the STXS framework [47, 91–93] are used. The inclusive production process classes defined at "Stage-0" in the STXS scheme are: $b\bar{b}H$ production; $t\bar{t}H$ and tH processes; $qq\rightarrow Hqq$ processes, with contributions from both VBF production and quark-initiated VH production with a hadronic decay of the gauge boson; WH and ZH production, including $gg\rightarrow ZH$, followed by a leptonic decay of the vector boson (V(lep)H); and finally the $gg\rightarrow H$ process, consisting of ggF and $gg\rightarrow ZH$, $Z\rightarrow q\bar{q}$ production. Since the acceptances for $gg\rightarrow H$ and $b\bar{b}H$ production are similar for all input analyses, the $b\bar{b}H$ production mode is modeled as a 1% increase of the $gg\rightarrow H$ yield in each region of production phase space [47]. Theory uncertainties for the $gg\rightarrow H$, $qq\rightarrow Hqq$, and $t\bar{t}H$ processes are defined as in Refs. [23, 24], while those of the V(lep)H process follow the scheme described in Ref. [94].

The analyses listed in Table 1 as using the 'STXS-0*' binning provide measurements of the scale factors $\mu^{i,X}$ for the product of the inclusive cross-section of one or more production modes i, with i=ggF, VBF, WH, ZH,

$t\bar{t}H$, tH[2], and branching ratio of the Higgs boson decay mode X. Analyses of the most sensitive production modes performed with the full Run 2 dataset, labeled 'STXS-1.2' in Table 1, report measurements of signal yield scale factors in the more fine-grained "Stage-1.2" definition of Higgs boson production cross-sections that partitions the Stage-0 regions in particle-level kinematic volumes, such as in a few coarse intervals of Higgs boson transverse momentum (p_{T}^{H}). The ensemble of parameters $\mu^{i,k',X}_{\mathrm{STXS-1.2}}$ describes deviations in differential distributions, with the level of detail controlled by the number of particle-level regions that are defined. The precision with which the more fine-grained set of scale factors $\mu^{i,k',X}_{\mathrm{STXS-1.2}}$ can be measured depends on the design of the analysis as well as the amount of available data. As individual analyses provide only limited sensitivity to some of the Stage-1.2 categories with the current dataset, some of these categories are merged w.r.t. the Stage-1.2 definitions given in Ref. [47]. Details of the merged category definitions in each analysis are provided in references [23–31]. The grouping of the production modes for STXS-0* and STXS-1.2 regions is also shown in the second column of Table 1.

After merging, a total of 78 signal yield parameters are extracted from the STXS measurements listed in Table 1. The kinematic definitions of these 78 STXS signal yield parameters, along with their measured signal strengths (*i.e.* their ratios to the corresponding SM predictions) and uncertainties, are shown in Figures 1–3. While the data underlying the measurements in these figures is the same as that used for the interpretation of the combined Higgs boson measurements shown in Ref. [9], the granularity of the STXS model used here is substantially larger, providing additional constraining power for the parameters of the SMEFT interpretation of the data. The χ^2 for the compatibility between the observed values and the SM hypothesis is 50 for 78 degrees of freedom, corresponding to a p-value of 99.4%.

For the MSSM and tree-level 2HDM interpretations of Section 4, no predictions are available for all production modes for the full STXS Stage-1.2 phase space partitioning. In this case, the interpretation is performed based on the STXS-0* production mode scale factors measured by each input analysis.

[2] The classification of production modes used in this note differs in one respect from the Stage-0 STXS definition: in the STXS definition $qq \to VH(qq)$ production and VBF production are both labeled as a common $qq \to Hqq$ production mode, whereas in this note these production modes are labeled separately.

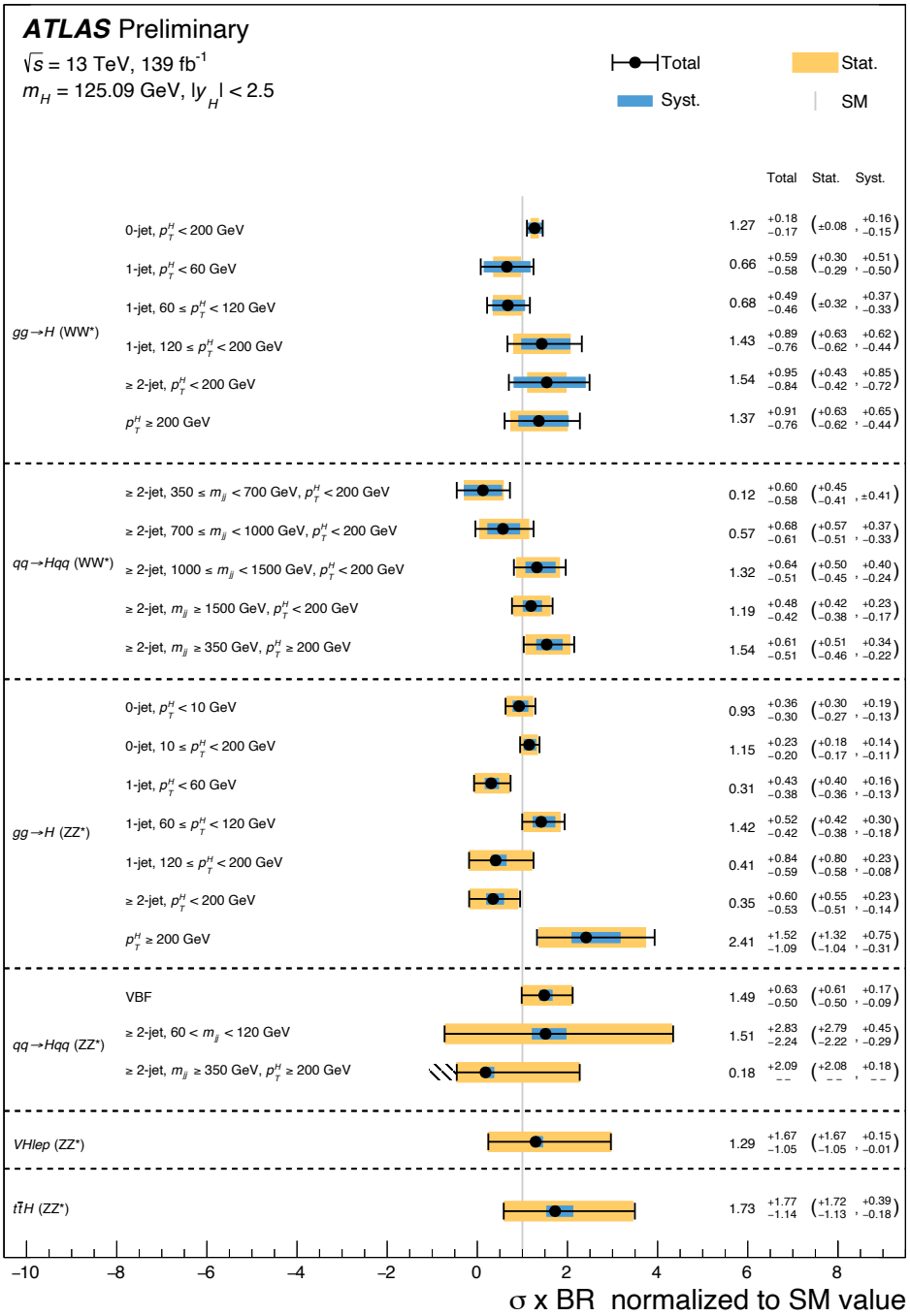

Figure 1: Measured signal strength for each of the $H \to WW^*$ and $H \to ZZ^*$ STXS categories included in the combination. In the $H \to ZZ^*$ analysis, VH production events with the vector boson V decaying to leptons are assigned to the VHlep category. In one category the negative uncertainty is truncated, as indicated by the hatched region, which corresponds to cross-section values for which the total yield prediction in an analysis region is negative. In that case, the negative uncertainty and its breakdown in terms of statistical and systematic components are not reported.

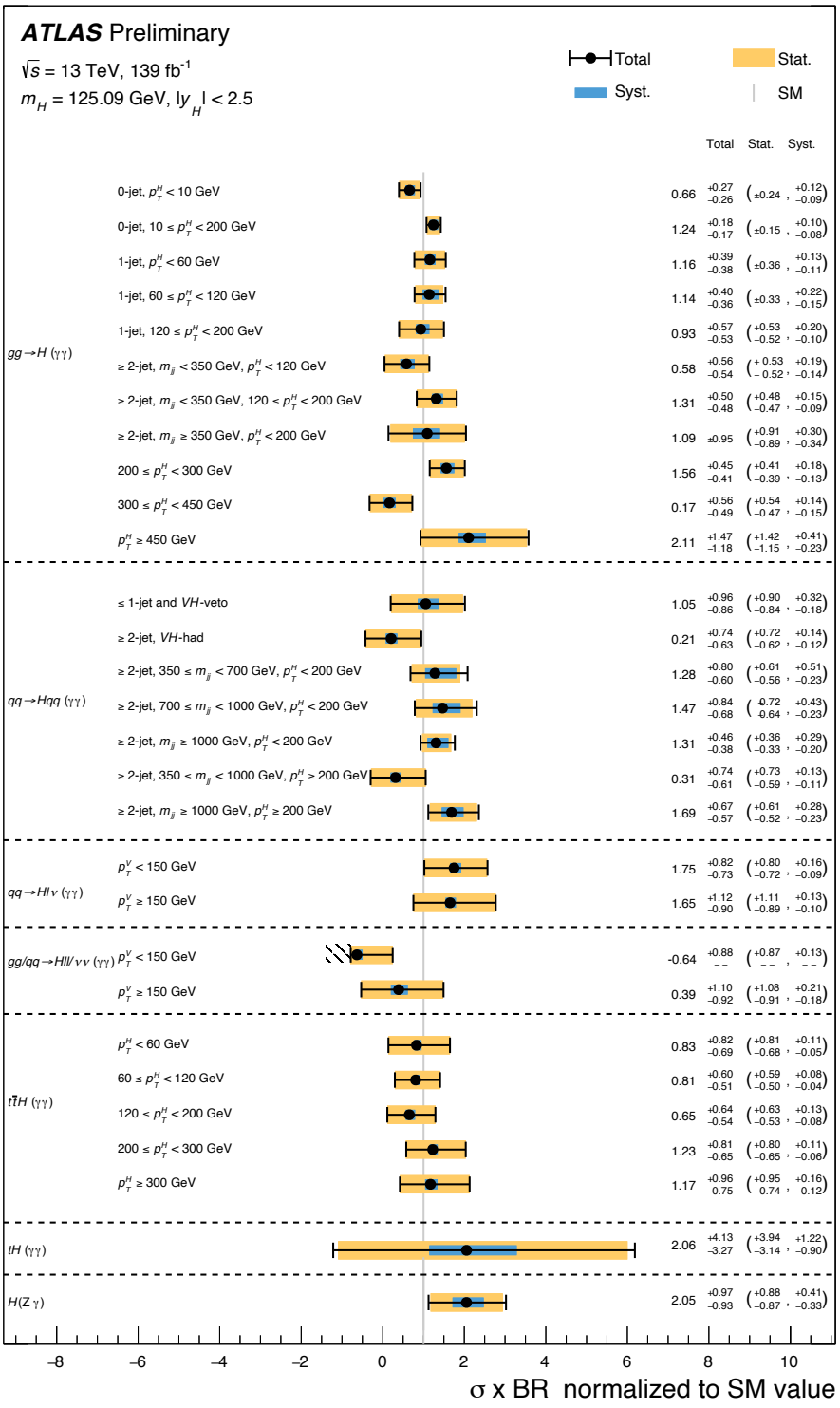

Figure 2: Measured signal strength for each of the $H \to \gamma\gamma$ and $H \to Z\gamma$ STXS categories included in the combination. In the $H \to \gamma\gamma$ analysis, events with two or more particle-level jets are assigned to the VH-veto (VH-had) categories if the leading di-jet invariant mass m_{jj} is in the range $m_{jj} < 60$ GeV or $120 \leq m_{jj} < 350$ GeV ($60 \leq m_{jj} < 120$ GeV). In one category the uncertainty is truncated, as indicated by the hatched region, which corresponds to cross-section values for which the total yield prediction in an analysis region is negative. In that case, the negative uncertainty and its breakdown in terms of statistical and systematic components are not reported.

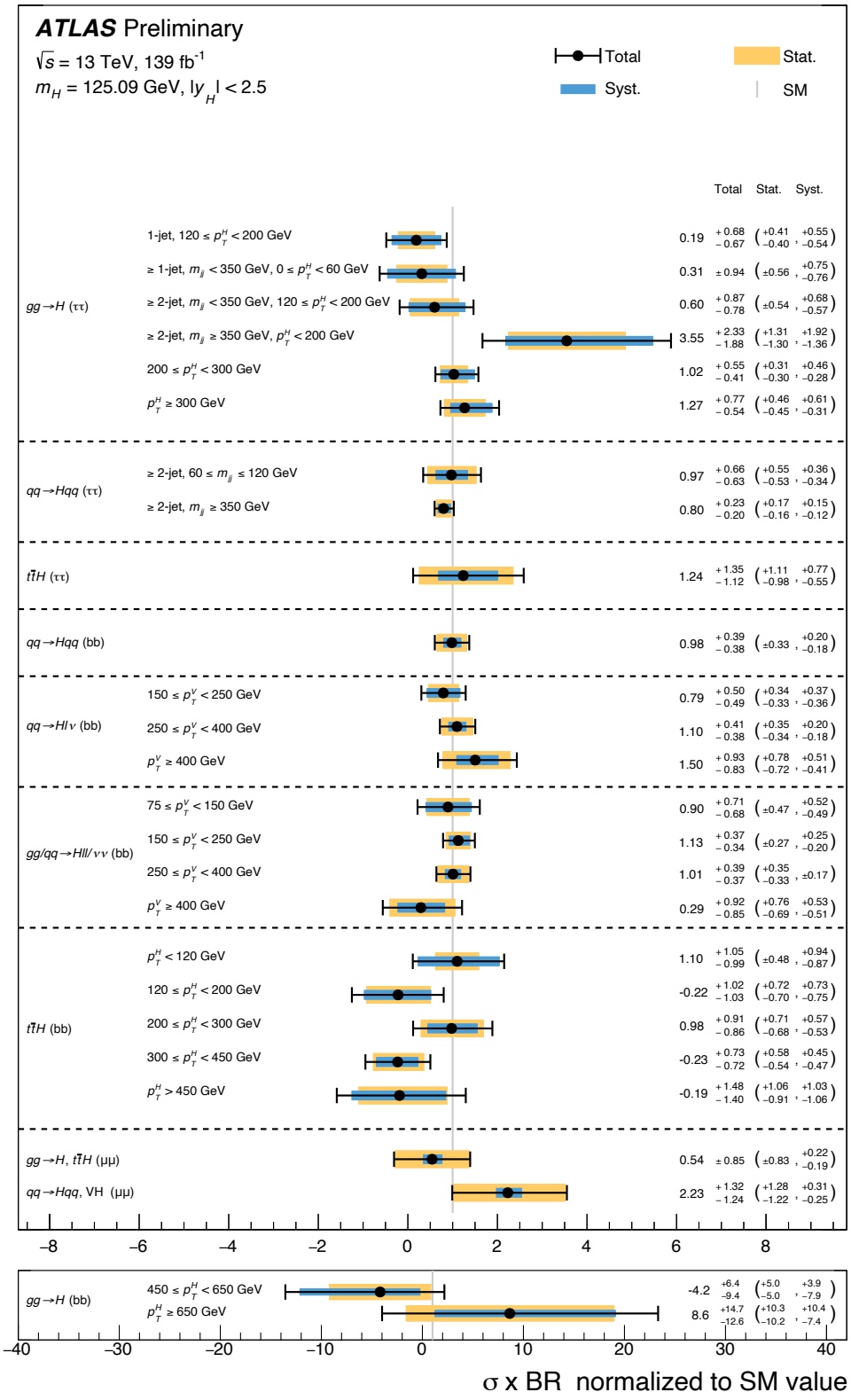

Figure 3: Measured signal strength for each of the $H \to \tau\tau$, $b\bar{b}$, and $\mu\mu$ STXS categories implemented.

3 Interpretations based on SM Effective Field Theory

3.1 Methodology of Effective Field Theory interpretations

The Standard Model Effective Field Theory provides an elegant language to encode the modifications of the Higgs boson properties induced by a wide class of BSM theories. Within the mathematical language of the SMEFT, the effects of BSM dynamics at high energies $\Lambda \gg v$, *i.e.* well above the electroweak scale $v = 246\,\text{GeV}$, can be parametrised at low energies, $E \ll \Lambda$, in terms of higher-dimensional operators built up from the Standard Model fields and respecting its symmetries such as gauge invariance. This yields an effective Lagrangian:

$$\mathcal{L}_{\text{SMEFT}} = \mathcal{L}_{\text{SM}} + \sum_{i}^{N_{d=6}} \frac{c_i}{\Lambda^2} O_i^{(6)} + \sum_{j}^{N_{d=8}} \frac{b_j}{\Lambda^4} O_j^{(8)} + \ldots, \tag{4}$$

where $\mathcal{L}_{\text{SM}}$ is the SM Lagrangian, $O_i^{(6)}$ and $O_j^{(8)}$ represent a complete set of operators of mass-dimensions $d = 6$ and $d = 8$, and c_i, b_j are the corresponding dimensionless Wilson coefficients. Operators with $d = 5$ and $d = 7$ violate lepton and/or baryon number conservation and are not considered in this study. The effective theory expansion in Eq. (4) is robust, fully general, and can be systematically matched to explicit UV-complete BSM scenarios.

The goal of the analysis is to constrain the $d = 6$ Wilson coefficients that correspond to operators that either directly or indirectly impact Higgs boson couplings to SM particles [95, 96]. Contributions of operators of mass-dimension $d = 8$, which are suppressed by $1/\Lambda^2$ with respect to the leading effects from $d = 6$ operators and whose impact on Higgs boson production and decay in the kinematic regions of interest are not fully calculated, are not considered. The "Warsaw" basis [97] is used, which forms a complete set of all $O_i^{(6)}$ operators in Eq. (4) allowed by the SM gauge symmetries. This basis is widely used in EFT constraints in various fields of particle physics.

In this note the 'top' flavour symmetry scheme for EFT operators is assumed, following the recommendation of Ref. [98]. In this scheme, quarks of the first two generations and quarks of the 3rd generation are described by independent fields, a $U(2)^3$ symmetry is imposed on the light quarks, and the quark sector of the EFT is assumed to have no mixing; all lepton generations are modeled independently. Table 2 lists the operators considered in the analysis of STXS data, and their corresponding Wilson coefficients c_i. Only CP-even $d = 6$ operators for which the Λ^{-2}-suppressed contribution to any of the STXS measurements shown in Figures 1–3 exceeds 0.1% with respect to the SM prediction at $c_i = 1$ are listed. The EFT analysis of the differential data only considers a subset of the coefficients listed, c_{HG}, c_{tH} and c_{tG}, due to the more restricted sensitivity of the differential analyses.

Throughout this note, a value of $\Lambda = 1\,\text{TeV}$ is assumed. Coefficients for alternative values of $\Lambda = X$ can be obtained through a scaling of the results presented in this note by a factor $(X/1\,\text{TeV})^2$. All Wilson coefficients are assumed to be real.

3.1.1 Simulation of the impact of SMEFT operators

The impact of the $d = 6$ SMEFT operators listed in Table 2 has been computed with two Universal FeynRules Output (UFO) models of MadGraph [70] normalised to theoretical calculations of production cross-sections and decay branching ratios as follows.

Table 2: Wilson coefficients $\boldsymbol{c}$ and corresponding $d = 6$ SMEFT operators O_j used in this analysis. The operator and coefficient notation follows the convention of Ref. [99].

Wilson coefficient	Operator
c_H	$(H^\dagger H)^3$
$c_{H\Box}$	$(H^\dagger H)\Box(H^\dagger H)$
c_G	$f^{abc} G^{a\nu}_\mu G^{b\rho}_\nu G^{c\mu}_\rho$
c_W	$\epsilon^{IJK} W^{I\nu}_\mu W^{J\rho}_\nu W^{K\mu}_\rho$
c_{HDD}	$\left(H^\dagger D^\mu H\right)^* \left(H^\dagger D_\mu H\right)$
c_{HG}	$H^\dagger H\, G^A_{\mu\nu} G^{A\mu\nu}$
c_{HB}	$H^\dagger H\, B_{\mu\nu} B^{\mu\nu}$
c_{HW}	$H^\dagger H\, W^I_{\mu\nu} W^{I\mu\nu}$
c_{HWB}	$H^\dagger \tau^I H\, W^I_{\mu\nu} B^{\mu\nu}$
$c^{(1)}_{Hl,11}$	$(H^\dagger i\overleftrightarrow{D}_\mu H)(\bar{l}_1 \gamma^\mu l_1)$
$c^{(1)}_{Hl,22}$	$(H^\dagger i\overleftrightarrow{D}_\mu H)(\bar{l}_2 \gamma^\mu l_2)$
$c^{(1)}_{Hl,33}$	$(H^\dagger i\overleftrightarrow{D}_\mu H)(\bar{l}_3 \gamma^\mu l_3)$
$c^{(3)}_{Hl,11}$	$(H^\dagger i\overleftrightarrow{D}^I_\mu H)(\bar{l}_1 \tau^I \gamma^\mu l_1)$
$c^{(3)}_{Hl,22}$	$(H^\dagger i\overleftrightarrow{D}^I_\mu H)(\bar{l}_2 \tau^I \gamma^\mu l_2)$
$c^{(3)}_{Hl,33}$	$(H^\dagger i\overleftrightarrow{D}^I_\mu H)(\bar{l}_3 \tau^I \gamma^\mu l_3)$
$c_{He,11}$	$(H^\dagger i\overleftrightarrow{D}_\mu H)(\bar{e}_1 \gamma^\mu e_1)$
$c_{He,22}$	$(H^\dagger i\overleftrightarrow{D}_\mu H)(\bar{e}_2 \gamma^\mu e_2)$
$c_{He,33}$	$(H^\dagger i\overleftrightarrow{D}_\mu H)(\bar{e}_3 \gamma^\mu e_3)$
$c^{(1)}_{Hq}$	$(H^\dagger i\overleftrightarrow{D}_\mu H)(\bar{q} \gamma^\mu q)$
$c^{(3)}_{Hq}$	$(H^\dagger i\overleftrightarrow{D}^I_\mu H)(\bar{q} \tau^I \gamma^\mu q)$
c_{Hu}	$(H^\dagger i\overleftrightarrow{D}_\mu H)(\bar{u}_p \gamma^\mu u_r)$
c_{Hd}	$(H^\dagger i\overleftrightarrow{D}_\mu H)(\bar{d}_p \gamma^\mu d_r)$
$c^{(1)}_{HQ}$	$(H^\dagger i\overleftrightarrow{D}_\mu H)(\bar{Q} \gamma^\mu Q)$
$c^{(3)}_{HQ}$	$(H^\dagger i\overleftrightarrow{D}^I_\mu H)(\bar{Q} \tau^I \gamma^\mu Q)$
c_{Ht}	$(H^\dagger i\overleftrightarrow{D}_\mu H)(\bar{t} \gamma^\mu t)$
c_{Hb}	$(H^\dagger i\overleftrightarrow{D}_\mu H)(\bar{b} \gamma^\mu b)$

Wilson coefficient	Operator
$c^{(1,1)}_{Qq}$	$(\bar{Q}\gamma_\mu Q)(\bar{q}\gamma^\mu q)$
$c^{(1,8)}_{Qq}$	$(\bar{Q}T^a\gamma_\mu Q)(\bar{q}T^a\gamma^\mu q)$
$c^{(3,1)}_{Qq}$	$(\bar{Q}\sigma^i\gamma_\mu Q)(\bar{q}\sigma^i\gamma^\mu q)$
$c^{(3,8)}_{Qq}$	$(\bar{Q}\sigma^i T^a\gamma_\mu Q)(\bar{q}\sigma^i T^a\gamma^\mu q)$
$c^{(3,1)}_{qq}$	$(\bar{q}\sigma^i\gamma_\mu q)(\bar{q}\sigma^i\gamma^\mu q)$
$c^{(1)}_{tu}$	$(\bar{t}\gamma_\mu t)(\bar{u}\gamma^\mu u)$
$c^{(8)}_{tu}$	$(\bar{t}T^a\gamma_\mu t)(\bar{u}T^a\gamma^\mu u)$
$c^{(1)}_{td}$	$(\bar{t}\gamma_\mu t)(\bar{d}\gamma^\mu d)$
$c^{(8)}_{td}$	$(\bar{t}T^a\gamma_\mu t)(\bar{d}T^a\gamma^\mu d)$
$c^{(1)}_{Qu}$	$(\bar{Q}\gamma_\mu Q)(\bar{u}\gamma^\mu u)$
$c^{(8)}_{Qu}$	$(\bar{Q}T^a\gamma_\mu Q)(\bar{u}T^a\gamma^\mu u)$
$c^{(1)}_{Qd}$	$(\bar{Q}\gamma_\mu Q)(\bar{d}\gamma^\mu d)$
$c^{(8)}_{Qd}$	$(\bar{Q}T^a\gamma_\mu Q)(\bar{d}T^a\gamma^\mu d)$
$c^{(1)}_{tq}$	$(\bar{q}\gamma_\mu q)(\bar{t}\gamma^\mu t)$
$c^{(8)}_{tq}$	$(\bar{q}T^a\gamma_\mu q)(\bar{t}T^a\gamma^\mu t)$
$c_{eH,22}$	$(H^\dagger H)(\bar{l}_2 e_2 H)$
$c_{eH,33}$	$(H^\dagger H)(\bar{l}_3 e_3 H)$
c_{uH}	$(H^\dagger H)(\bar{q} Y^\dagger_u u \widetilde{H})$
c_{tH}	$(H^\dagger H)(\bar{Q}\widetilde{H} t)$
c_{bH}	$(H^\dagger H)(\bar{Q} H b)$
c_{tG}	$(\bar{Q}\sigma^{\mu\nu}T^A t)\widetilde{H}\, G^A_{\mu\nu}$
c_{tW}	$(\bar{Q}\sigma^{\mu\nu} t)\tau^I \widetilde{H}\, W^I_{\mu\nu}$
c_{tB}	$(\bar{Q}\sigma^{\mu\nu} t)\widetilde{H}\, B_{\mu\nu}$
$c_{ll,1221}$	$(\bar{l}_1\gamma_\mu l_2)(\bar{l}_2\gamma^\mu l_1)$

Calculations for Higgs boson production modes with tree-level diagrams have been performed with SMEFTsim [99] under the assumption of the 'top' flavour symmetry scheme, following the recommendation of Ref. [98] and providing as input $G_F = 1.1663787 \times 10^{-5}$ GeV^{-2}, $m_Z = 91.1876$ GeV, and $m_W = 80.387$ GeV, where G_F is the Fermi constant and m_Z and m_W are the Z and W boson masses respectively. Cross-sections have been calculated at NLO accuracy in QCD for ggF, $gg \to ZH$ and $H \to gg$ with SMEFTatNLO [100] and at NLO accuracy in QED for SMEFT-SM interference terms in $H \to \gamma\gamma$ [101] and $H \to Z\gamma$ [102]. Lowest order calculations in QCD for $m_H = 125.09$ GeV are used for all other production and decay modes. SMEFT modifications to the background processes in the included analyses are not considered.

In the simulation, the following requirements are applied at particle level: the minimal jet transverse momentum is $p_T > 20$ GeV, and an angular separation $\Delta R > 0.05$ between two jets or two leptons is required, in order to avoid divergences in the matrix element calculation. For all events, Pythia8 is used for the simulation of parton showering, where the Higgs boson decay is based on the width calculated by MadGraph for the EFT parameters in question. In ggF events a matching is performed with the MLM algorithm [103, 104] to remove phase space overlap between the jets from the matrix element and the shower. For analyses based on the STXS methodology, the Rivet program [105] with the `HiggsTemplateCrossSections` [106] routine is used to analyse the simulated events, compute high-level kinematic quantities and classify the events according to their STXS region.[3]

The cross-section predictions for a specific process, calculated as described above, are estimated as the sum of three terms:

$$\sigma_{\text{SMEFT}} = \sigma_{\text{SM}} + \sigma_{\text{int}} + \sigma_{\text{BSM}}, \tag{5}$$

where σ_{SM} is the SM cross-section, σ_{int} describes the interference between the SMEFT operators (BSM processes) and SM operators, and σ_{BSM} is the cross-section involving exclusively SMEFT operators. When considering only $d = 6$ SMEFT operators, it follows from Eq. (4) that σ_{int} consists of terms involving a single $d = 6$ SMEFT operator, suppressing each term by a factor Λ^{-2}, and that σ_{BSM} contains terms involving products of two $d = 6$ SMEFT operators, suppressing each term by a factor Λ^{-4}. For this reason, the impact of the σ_{BSM} term is generally expected to be small, though its impact may still be non-negligible in certain regions of phase space, e. g. when energy scales are of order Λ.

Additional terms suppressed by a factor Λ^{-4} occur in the general SMEFT expansion of Eq. (4), *i.e.* the lowest-order cross-section terms generated by $d = 8$ operators that involve interference between SM and these operators. As only a subset of Higgs processes have been calculated with $d = 8$ operators [107–109], the list of terms suppressed by a factor Λ^{-4} considered is incomplete and the effect of the missing $d = 8$ terms relative to σ_{BSM} is not known in general. However, their effect may be of a magnitude comparable to that of products of two $d = 6$ SMEFT operators, as the suppression factor is at the same order. For this reason, SMEFT interpretations will be presented both with and without the σ_{BSM} contribution to give a general indication of the sensitivity of the analysis to Λ^{-4} terms.

To reduce the perturbative QCD uncertainty on the extraction of the SMEFT Wilson coefficients, the parametrisation of the predicted cross-section of Eq. (5) is computed as a relative correction to the SM

[3] The Rivet algorithm has been modified to classify events in which a Higgs boson and two leptons arise from the same production vertex as VH production events. This modification ensures the proper classification of events with leptons from off-shell V decays, since MadGraph only saves on-shell intermediate particles. Contributions from off-shell V bosons are small in the SM, but can be enhanced by SMEFT operators.

prediction computed at the highest available order for each process:

$$\sigma_{\text{SMEFT}} = \sigma_{\text{SM}}^{((\text{N})\text{N})\text{NLO}} \times \left(1 + \frac{\sigma_{\text{int}}^{(\text{N})\text{LO}}}{\sigma_{\text{SM}}^{(\text{N})\text{LO}}} + \frac{\sigma_{\text{BSM}}^{(\text{N})\text{LO}}}{\sigma_{\text{SM}}^{(\text{N})\text{LO}}}\right). \tag{6}$$

This calculation strategy assumes that higher-order terms have the same relative effect on σ_{int} and σ_{BSM} as on σ_{SM} [110].

The predictions are further modified by the impact of SMEFT operators on Higgs boson decay branching ratios. Since the Higgs boson is a narrow, scalar particle, and only on-shell production is considered in this analysis, its production cross-section and decay width factorise. The impact of SMEFT operators on production and decay therefore also factorises and can be derived independently. Thus, the cross-section for a given Higgs boson production process i in particle-level region k' and for a given decay mode $H \to X$ is

$$(\sigma \times B)_{\text{SMEFT}}^{i,k',H\to X} = \sigma_{\text{SMEFT}}^{i,k'} \times B_{\text{SMEFT}}^{H\to X} = \left(\sigma_{\text{SM}}^{i,k'} + \sigma_{\text{int}}^{i,k'} + \sigma_{\text{BSM}}^{i,k'}\right) \times \left(\frac{\Gamma_{\text{SM}}^{H\to X} + \Gamma_{\text{int}}^{H\to X} + \Gamma_{\text{BSM}}^{H\to X}}{\Gamma_{\text{SM}}^{H} + \Gamma_{\text{int}}^{H} + \Gamma_{\text{BSM}}^{H}}\right).$$

The factorised SMEFT prediction is calculated with ratios as in Eq. (6) to utilise the SM prediction at the highest available order:

$$(\sigma \times B)_{\text{SMEFT}}^{i,k',H\to X} = (\sigma \times B)_{\text{SM,(N(N))NLO}}^{i,k',H\to X} \left(1 + \frac{\sigma_{\text{int,(N)LO}}^{i,k'}}{\sigma_{\text{SM,(N)LO}}^{i,k'}} + \frac{\sigma_{\text{BSM,(N)LO}}^{i,k'}}{\sigma_{\text{SM,(N)LO}}^{i,k'}}\right)\left(\frac{1 + \frac{\Gamma_{\text{int}}^{H\to X}}{\Gamma_{\text{SM}}^{H\to X}} + \frac{\Gamma_{\text{BSM}}^{H\to X}}{\Gamma_{\text{SM}}^{H\to X}}}{1 + \frac{\Gamma_{\text{int}}^{H}}{\Gamma_{\text{SM}}^{H}} + \frac{\Gamma_{\text{BSM}}^{H}}{\Gamma_{\text{SM}}^{H}}}\right), \tag{7}$$

where the ratios $\sigma_{\text{int}}/\sigma_{\text{SM}}$ and $\Gamma_{\text{int}}/\Gamma_{\text{SM}}$ have a linear dependence on SMEFT operators and are suppressed by a factor Λ^{-2}, and the ratios $\sigma_{\text{BSM}}/\sigma_{\text{SM}}$ and $\Gamma_{\text{BSM}}/\Gamma_{\text{SM}}$ have a quadratic dependence on SMEFT operators and are suppressed by a factor Λ^{-4}. In the analysis, these ratios are parametrised as

$$\frac{\sigma_{\text{int}}^{i,k'}}{\sigma_{\text{SM}}^{i,k'}} = \sum_j A_j^{\sigma_{i,k'}} c_j \qquad \frac{\sigma_{\text{BSM}}^{i,k'}}{\sigma_{\text{SM}}^{i,k'}} = \sum_{j,l\geq j} B_{jl}^{\sigma_{i,k'}} c_j c_l \tag{8}$$

$$\frac{\Gamma_{\text{int}}^{H\to X}}{\Gamma_{\text{SM}}^{H\to X}} = \sum_j A_j^{\Gamma^{H\to X}} c_j \qquad \frac{\Gamma_{\text{BSM}}^{H\to X}}{\Gamma_{\text{SM}}^{H\to X}} = \sum_{j,l\geq j} B_{jl}^{\Gamma^{H\to X}} c_j c_l \tag{9}$$

$$\frac{\Gamma_{\text{int}}^{H}}{\Gamma_{\text{SM}}^{H}} = \sum_j A_j^{\Gamma^{H}} c_j \qquad \frac{\Gamma_{\text{BSM}}^{H}}{\Gamma_{\text{SM}}^{H}} = \sum_{j,l\geq j} B_{jl}^{\Gamma^{H}} c_j c_l, \tag{10}$$

with

$$A_j^{\Gamma^H} = \frac{\sum_X \Gamma_{\text{SM}}^{H\to X} A_j^{\Gamma^{H\to X}}}{\sum_X \Gamma_{\text{SM}}^{H\to X}} \qquad B_{jl}^{\Gamma^H} = \frac{\sum_X \Gamma_{\text{SM}}^{H\to X} B_{jl}^{\Gamma^{H\to X}}}{\sum_X \Gamma_{\text{SM}}^{H\to X}}. \tag{11}$$

In Eq. (11) all Higgs boson decay modes X with up to four final-state particles are included in the sum. All $A_j^{\sigma_{i,k'}}$, $A_j^{\Gamma^{H\to X}}$, $B_{jl}^{\sigma_{i,k'}}$ and $B_{jl}^{\Gamma^{H\to X}}$ coefficients are constant factors obtained from simulation that express the sensitivity of the process to the operators O_j and O_l that correspond to the Wilson coefficients c_j and c_l,

where the indices j, l run over all non-negligible operators. The coefficients A_j and B_{jl} are proportional respectively to Λ^{-2} and Λ^{-4}. The values of all SM Higgs branching ratios that enter Eq. (11) are taken from Ref. [47].

For the interpretation of the differential analyses, where the measured parameters $\sigma_{\text{fid.}}^{k',X}$ do not label individual production processes, the relative fractions of the different processes are predicted according to the SMEFT calculations as in Eq. (6).

Using Eqs. (7)–(10), two statistical models are constructed for the interpretation of the data: a linearised variant that only considers terms suppressed by up to a factor Λ^{-2}, and a linear+quadratic variant that considers all available terms, including those with suppression factor Λ^{-4}.

3.1.2 Cross-section calculation with linear terms

In a scenario where Λ^{-4}-suppressed contributions are ignored, the predicted deviation of the cross-section, partial width and total width from their SM values can each be explicitly linearised as a function of the Wilson coefficients $\boldsymbol{c}$. Ignoring all Λ^{-4}-suppressed BSM terms in Eq. (7), and using the parametrisation of Eqs. (8)–(10), the expression for the cross-section times branching ratio reduces to

$$
\begin{aligned}
(\sigma\times B)^{i,k',H\to X}_{\text{SMEFT}} &= (\sigma\times B)^{i,k',H\to X}_{\text{SM,((N)N)NLO}} \times \left(1 + \frac{\sigma^{i,k'}_{\text{int,(N)LO}}}{\sigma^{i,k'}_{\text{SM,(N)LO}}}\right) \times \left(\frac{1 + \frac{\Gamma^{H\to X}_{\text{int}}}{\Gamma^{H\to X}_{\text{SM}}}}{1 + \frac{\Gamma^{H}_{\text{int}}}{\Gamma^{H}_{\text{SM}}}}\right) \\
&= (\sigma\times B)^{i,k',H\to X}_{\text{SM,((N)N)NLO}} \times \left(1 + \sum_j A_j^{\sigma_{i,k'}} c_j\right) \times \left(\frac{1 + \sum_j A_j^{\Gamma^{H\to X}} c_j}{1 + \sum_j A_j^{\Gamma^{H}} c_j}\right), \\
&= (\sigma\times B)^{i,k',H\to X}_{\text{SM,((N)N)NLO}} \times \left(\frac{1 + \sum_j \left(A_j^{\sigma_{i,k'}} + A_j^{\Gamma^{H\to X}}\right) c_j + O\left(\Lambda^{-4}\right)}{1 + \sum_j A_j^{\Gamma^{H}} c_j + O\left(\Lambda^{-4}\right)}\right),
\end{aligned}
\tag{12}
$$

where all higher order terms in the expansion are suppressed by power Λ^{-4} or beyond.

A subsequent Taylor expansion of the width ratio expression of Eq. (12) and truncation of terms beyond Λ^{-2} would result in a completely linearised expression for $\sigma\times B$. However, as the parametric dependence of a Wilson coefficient in a branching fraction f is effectively of the form $c/(1 + f \cdot c)$, the linearity in c of this expression assumed for small values of c does not hold for large values of c. This effect is particularly pronounced for operators affecting Higgs boson decays with a large branching fraction, e.g. c_{bH}, and operators that have a large measured uncertainty that allows large values of c in the error propagation. For this reason, a full Taylor expansion of the ratio is not performed.

3.1.3 Cross-section calculation with linear and quadratic terms

The SMEFT prediction including the available terms proportional to Λ^{-4} is:

$$
\begin{aligned}
(\sigma\times B)^{i,k',H\to X}_{\text{SMEFT}} &= (\sigma\times B)^{i,k',H\to X}_{\text{SM,((N)NLO}}\left(1+\sum_j A_j^{\sigma_{i,k'}} c_j + \sum_{j,l\geq j} B_{jl}^{\sigma_{i,k'}} c_j c_l\right)\left(\frac{1+\sum_j A_j^{\Gamma^{H\to X}} c_j + \sum_{j,l\geq j} B_{jl}^{\Gamma^{H\to X}} c_j c_l}{1+\sum_j A_j^{\Gamma^{H}} c_j + \sum_{j,l\geq j} B_{jl}^{\Gamma^{H}} c_j c_l}\right), \\
&= (\sigma\times B)^{i,k',H\to X}_{\text{SM,((N)NLO}} \cdot \\
&\left(\frac{1+\sum_j\left(A_j^{\sigma_{i,k'}}+A_j^{\Gamma^{H\to X}}\right)c_j+\sum_{j,l\geq j}\left(B_{jl}^{\sigma_{i,k'}}+B_{jl}^{\Gamma^{H\to X}}+A_j^{\sigma_{i,k'}}A_l^{\Gamma^{H\to X}}+A_l^{\sigma_{i,k'}}A_j^{\Gamma^{H\to X}}\right)c_j c_l+O\left(\Lambda^{-6}\right)}{1+\sum_j\left(A_j^{\Gamma^{H}}\right)c_j+\sum_{j,l\geq j}\left(B_{jl}^{\Gamma^{H}}\right)c_j c_l+O\left(\Lambda^{-6}\right)}\right)
\end{aligned}
\tag{13}
$$

where both numerator and denominator are a second-order Taylor expansion resulting in a linearised expression for terms of order Λ^{-2} and a quadratic expression for terms of order Λ^{-4}. Similar to Eq. (12), and for the same reason, the width ratio expression in Eq. (13) is not subjected to a further Taylor-expansion. While the set of operators proportional to Λ^{-4} considered in Eq. (13) is not complete due to missing $d = 8$ operators, as noted earlier a comparison of results obtained with the linear and linear+quadratic statistical models is indicative of the sensitivity of the measurements to terms suppressed by Λ^{-4}.

Figure 4 illustrates the impact of the linear terms A_j for the three SMEFT operators considered in the interpretation of the fiducial differential cross-section measurements, whereas Figure 5 shows the impact of linear and linear+quadratic terms on production ($A_j^{\sigma_{i,k'}}$) and decay $\left(\frac{1+A_j^{\Gamma^{H\to X}}}{1+A_j^{\Gamma^{H}}}-1\right)$ rates.

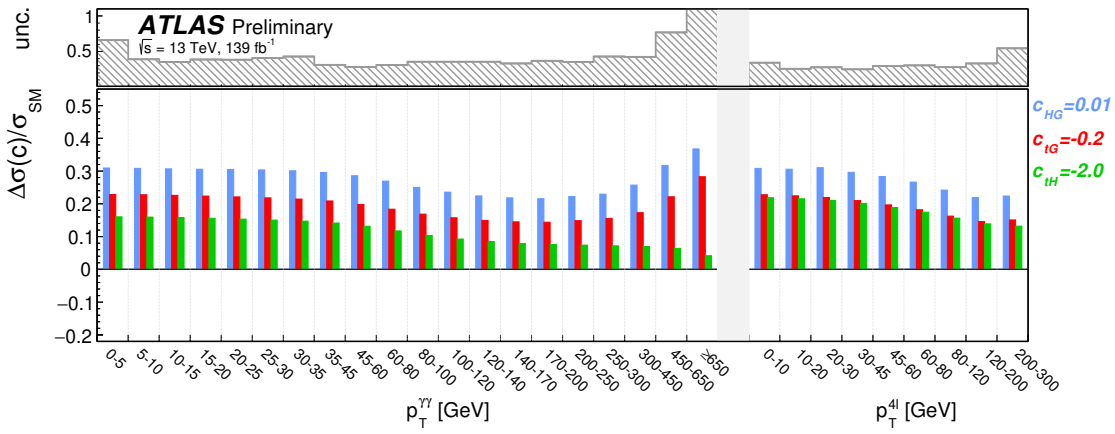

Figure 4: Expected impact of the SMEFT operators on the fiducial differential distributions of the transverse momentum of the Higgs boson decay products in $H\to\gamma\gamma$ and $H\to ZZ^*$ decays, relative to the SM cross-section, under the assumption of the linearised SMEFT model. The values of the Wilson coefficients, specified in the legend, are chosen to show the distribution of the operator impact in the same range as the typical uncertainty of the measurement. To judge the experimental sensitivity to constrain the operators from the data in the listed fiducial regions, the total uncertainty on the measurement in each region is shown in the top panel. For presentational clarity, the uncertainty of low precision regions is clipped off in the plot. The impact of these three operators in the STXS analysis is shown in matching colors in the bottom panel of Figure 5 for coefficient variations of identical magnitude.

The relative importance of the quadratic term increases linearly with the considered variation of the corresponding Wilson coefficient. Figure 5 shows that the quadratic terms have the highest impact in the

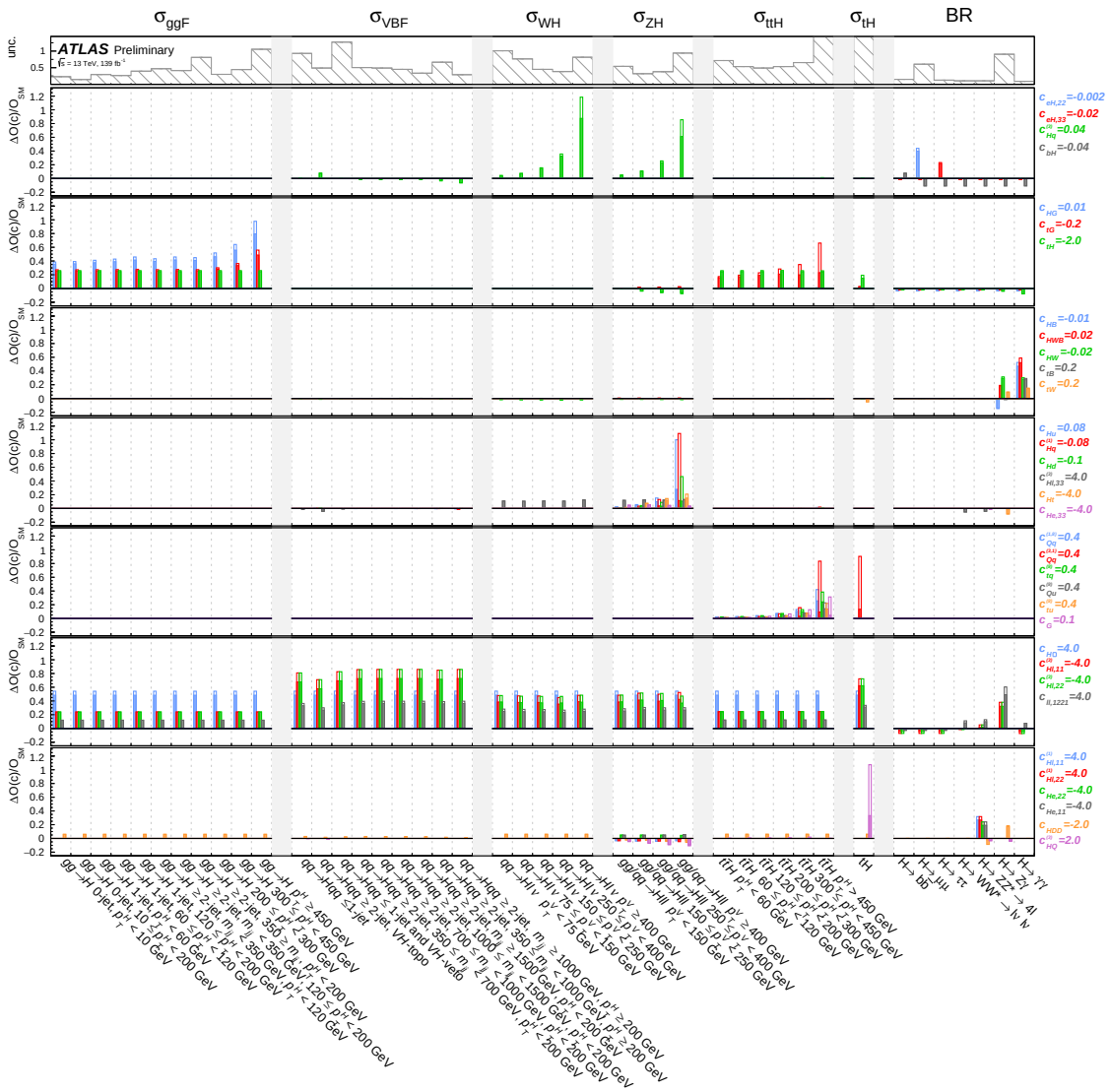

Figure 5: Expected impact of the most relevant SMEFT operators on the observables O (cross sections in STXS-1.2 regions or decay branching ratios), relative to the SM predictions, for the linearised SMEFT model (shaded histogram) and the linear+quadratic SMEFT model (open histogram). The values of the Wilson coefficients, specified in the legend, are chosen to show the distribution of the operator impact in the same range as the typical uncertainty of the measurement. To judge the experimental sensitivity to constrain the operators from the data, the total uncertainty on the measurement of each observable is shown in the top panel. For columns corresponding to multiple measurements of the same observable, the shown uncertainty reflects the uncertainty on the average, under the assumption of uncorrelated uncertainties. For presentational clarity, the uncertainty of low precision measurements is clipped off in the plot.

high-p_{T} regions of VH production for the coefficients $c_{Hq}^{(1)}3, c_{Hq}^{(1)}1, c_{Hd}, c_{Hu}$, on high-$p_{\mathrm{T}}$ (inclusive) $t\bar{t}H$ production for the coefficients c_{tG}, $c_{Qq}^{(1,8)}$, $c_{Qq}^{(3,1)}$, $c_{tq}^{(8)}$, $c_{Qu}^{(8)}$, $c_{tu}^{(8)}$, (c_G), and in the tH channel for the coefficients $c_{HQ}^{(3)}$ and $c_{Qq}^{(3,1)}$.

3.1.4 Assumptions on SM Higgs boson kinematics

With the insertion of the SMEFT cross-section predictions of Eqs. (12) or (13) in Eqs. (2) and (3) describing the expected signal yield s_k for each analysis region k, *i.e.*

$$\mu^{i,k',X} \to \frac{(\sigma\times B)^{i,k',H\to X}_{\mathrm{SM}+\Lambda^{-2,-4}}}{(\sigma\times B)^{i,k',H\to X}_{\mathrm{SM,((N(N))NLO}}} \text{ in Eq. (2)},$$
$$\sigma^{k',X}_{\mathrm{fid.}} \to (\sigma\times B)^{i,k',H\to X}_{\mathrm{SM}+\Lambda^{-2,-4}} \text{ in Eq. (3)},$$

the effect of SMEFT cross-section modifications on the inclusive Higgs boson signal yield for each particle-level region k' is fully taken into account for every reconstruction-level region k. However, the SMEFT operators may also affect other terms of the likelihood, notably the efficiency-times-acceptance factors $\epsilon_k^{i,X,k'}$ occurring in Eqs. (2) and (3), as well as the signal yield distribution inside each region k represented by the factor $f_s^{r,k}$ occurring in Eq. (1).

In both the linear and linear+quadratic SMEFT models, it is assumed that the theoretical systematic uncertainties assigned to the acceptance factors $\epsilon_k^{i,X,k'}$, which are fully taken into account in the SM cross-section prediction, cover the possible acceptance changes induced by SMEFT operators in Higgs boson production through the full validity range of the SMEFT model. This assumption is motivated by the similarity of reconstruction-level analysis regions to STXS and differential fiducial regions, which are designed to be relatively insensitive to acceptance changes induced by SMEFT operators. In addition, the rather fine binning of the Stage-1.2 STXS regions reduces further the possibility of significant variations of the acceptance factors inside each region. The effect of SMEFT operators on other observables used in the definition of the analysis regions, e.g. through multivariate discriminants, is assumed to be negligible.

Conversely, the effect of SMEFT operators on Higgs boson decays can strongly affect the acceptance factors $\epsilon_k^{i,X}$, since decays are not limited to a restricted fiducial phase space in the STXS framework. For 2-body decays, such acceptance effects are generally small. However, the four-body $H\to ZZ^*\to 4\ell$ and $H\to WW^*\to \ell\nu\ell\nu$ decays are significantly impacted by acceptance effects, hence for these decays the impact factors $A_j^{H\to X}$ and $B_{jl}^{H\to X}$ are recalculated including an approximate implementation of the reconstruction-level requirements at the particle level. The impact of acceptance effects is evaluated for all operators in Table 2 that can affect $\Gamma^{H\to ZZ^*}$ or $\Gamma^{H\to WW^*}$, *i.e.* $c_{H\Box}$, c_{HDD}, c_{HW}, c_{HB}, c_{HWB}, $c^{(1)}_{Hl,11}$, $c^{(1)}_{Hl,22}$, $c^{(3)}_{Hl,11}$, $c^{(3)}_{Hl,22}$, $c_{He,11}$, $c_{He,22}$ and $c_{ll,1221}$, and is observed to be non-negligible for four of these, c_{HW}, c_{HB}, c_{HWB}, and $c^{(3)}_{Hl}$. For these, the corresponding recalculated factors $A_j^{H\to X}$, $B_{jl}^{H\to X}(X = WW^*, ZZ^*)$ with approximate acceptance modeling are used in the STXS SMEFT analysis. Figure 6 illustrates the effect of the c_{HW} operator on the acceptance in the $H\to WW^*$ and $H\to ZZ^*$ decay modes. The acceptance correction is not used in the differential analysis of $H\to ZZ^*$, as none of the three operators analyzed for that measurement are affected. For all other Higgs boson decays, the acceptance effects from SMEFT operators are neglected.

Finally, if the signal yield distribution inside an analysis region k deviates from the SM distribution encoded in $f_s^{r,k}$ in Eq. (1), the measured yield s_k may be biased. This effect is expected to be negligible for all regions where the discriminant observable inside the region is the reconstructed invariant mass of the Higgs boson, which is largely unaffected by SMEFT operators. Regions that feature a multivariate discriminant as observable can potentially be more affected by SMEFT induced shape differences, but are only used in regions with low signal yields where it is assumed that any effect induced by signal shape deviations is small compared to the statistical uncertainties. For the high-yield $H\to WW^*$ channel, where the transverse

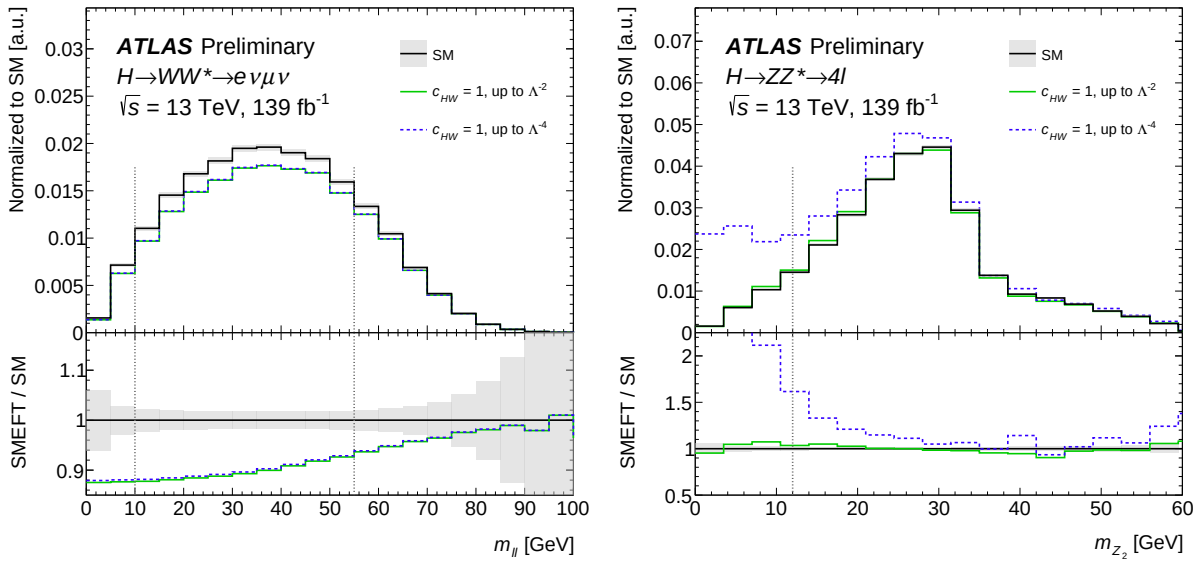

(a) (b)

Figure 6: Illustration of the effect of a variation of the SMEFT coefficient c_{HW} on kinematic observables used in the event selection: (a) impact on the dilepton invariant mass in the $H \to WW^* \to e\nu\mu\nu$ analysis, and (b) impact on the invariant mass of the 3rd and 4th p_{T}-ranked lepton in the $H \to ZZ^* \to 4\ell$ analysis. The vertical dotted lines indicate the selection criteria applied on the corresponding variables by the $H \to WW^*$ analysis ($10 < m_{\ell\ell} < 55$ GeV) and by the $H \to ZZ^*$ analysis ($m_{Z_2} > 12$ GeV). The grey bands show the statistical uncertainty of the SMEFT simulation.

mass m_{T} is used as discriminant observable, which is sensitive to SMEFT operators, it has been verified that the effect of shape variations induced by the SMEFT operators is negligible for the range of coefficient values that are consistent with the observed measurement.

3.2 Constraints from STXS measurements

The aim of the EFT analysis is to obtain constraints on the Wilson coefficients c_j through a maximum likelihood analysis of the Higgs boson STXS measurements shown in Figures 1–3. All signal strength modifiers $\mu^{i,k',X}$ of Eq. (2) are directly expressed in terms of the coefficients c_j:

$$s_k(\boldsymbol{c},\boldsymbol{\theta}) = \sum_{i,k',X} \left(\mu^{i,k',X} \equiv \frac{(\sigma\times B)^{i,k',H\to X}_{\mathrm{SMEFT}}(\boldsymbol{c})}{(\sigma\times B)^{i,k',H\to X}_{\mathrm{SM,(N(N))NLO}}} \right) \times \mathcal{L} \times (\sigma\times B)^{i,k',H\to X}_{\mathrm{SM,(N(N))NLO}}(\boldsymbol{\theta}) \times \epsilon_k^{i,k',X}(\boldsymbol{\theta}),$$

with $\mathcal{L}, \epsilon_k^{i,k',X}(\boldsymbol{\theta})$ and $\boldsymbol{\theta}$ as defined in Eq. (2), and where the signal cross-section $(\sigma\times B)^{i,k',H\to X}_{\mathrm{SMEFT}}(\boldsymbol{c})$ is either taken from the linear model of Eq. (12) or the linear+quadratic model of Eq. (13).

The available data samples contain insufficient information to constrain all coefficients $\boldsymbol{c}$ listed in Table 2 simultaneously, hence a standard numerical joint maximum likelihood estimation of this set of parameters $\boldsymbol{c}$ will not converge. As degrees of freedom left unconstrained by the data do not necessarily correspond to individual coefficients c_j, but may also be linear combinations $\sum_j a_j c_j$, a modified basis is defined and

used in the following, to ensure the convergence of the numerical likelihood maximisation procedure for the largest number of degrees of freedom that can be probed by the current set of measurements.

3.2.1 Sensitivity estimate and choice of parameters

To determine a modified basis $\boldsymbol{c'}$ that can be estimated from the data, the SM expected covariance matrix V_{STXS} of the measurement, expressed in the STXS basis $\{\mu^{i,k',X}\}$, is analysed. From V_{STXS}, the Hessian matrix V^{-1}_{STXS} is obtained, and then rotated to the SMEFT basis $\{c_j\}$:

$$V^{-1}_{\text{SMEFT}} = P^{T}_{(i,k',X)\to(j)}\, V^{-1}_{\text{STXS}}\, P_{(i,k',X)\to(j)}. \tag{14}$$

The expected Jacobian matrix $P_{(i,k',X)\to(j)}$ is based on the linearised SMEFT model of Eq. (12):

$$P_{(i,k',X)\to(j)} = A_j^{\sigma_{i,k'}} + A_j^{\Gamma^{H\to X}} - A_j^{\Gamma^{H}}, \tag{15}$$

where $A_j^{\sigma_{i,k'}}$, $A_j^{\Gamma^{H\to X}}$ and $A_j^{\Gamma^{H}}$ are the constant factors obtained from the simulation.

In the limit of Gaussian STXS measurements, the matrix V^{-1}_{SMEFT} represents the Fisher information matrix of its linearised SMEFT model re-parametrisation, with the additional caveat that for large coefficient variations the representation of V^{-1}_{SMEFT} may be suboptimal, as a consequence of the fully linearized form of Eq. (15) that is only valid in the limit of small coefficient values. An eigenvalue decomposition of the Fisher information matrix yields the eigenvectors $ev^{[i]}$ and their corresponding eigenvalues λ_i and variances $1/\lambda_i$.

Figure 7 lists the eigenvectors obtained from the expected measurements and accounting for the observed values of nuisance parameters, ranked by eigenvalue and truncated to eigenvalues $\lambda_i \geq 0.01$, corresponding to a truncation at an estimated uncertainty of $\sigma(ev^{[i]}) \leq 10$, well beyond the validity range of the Wilson coefficients of $O(1)$.

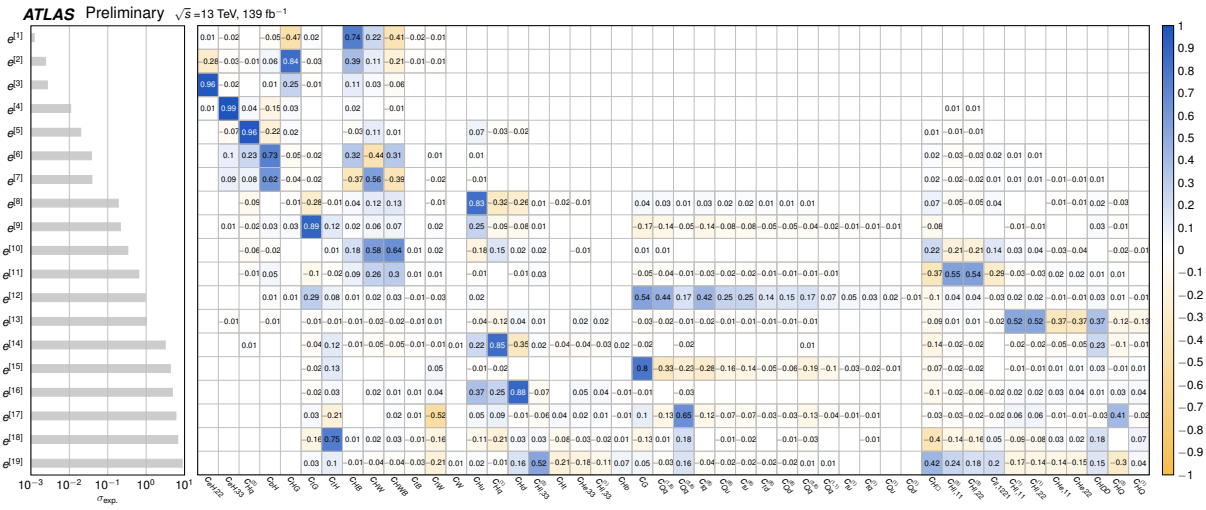

Figure 7: Eigenvectors of the inverse EFT covariance matrix obtained by propagating the SMEFT parameterisation to the covariance matrix V_{STXS} and requiring a significant (≥ 0.01) eigenvalue λ. The corresponding expected uncertainty $\sigma_{\text{exp.}} = 1/\sqrt{\lambda}$ for each eigenvector is also shown.

From the ranking shown in Figure 7 and a survey of the sensitivity of the STXS regions to the Wilson coefficients in the linearised model, as shown in Figure 5, the following observations are made:

- The coefficients $c_{eH,33}$, $c_{eH,22}$, and c_{bH}, representing the Yukawa coupling modifiers of the $H \to \tau\tau$, $H \to \mu\mu$, and $H \to b\bar{b}$ decays respectively, can be individually measured from the corresponding Higgs channels that enter the combination. There are weak correlations of these operators with other SMEFT operators, primarily for c_{bH}, through their contribution to the total Higgs boson width.
- The coefficient $c_{Hq}^{(3)}$ affects both the WH and ZH production modes with an increasing impact as a function of the transverse momentum p_{T}^{V} of the W and Z bosons, and is constrained almost exclusively by the VH, $H \to b\bar{b}$ analysis.
- The coefficients c_{HG}, c_{tG} and c_{tH} are constrained by ggF and $t\bar{t}H$ production. As the uncertainties of the constrained directions span more than two orders of magnitude, it is beneficial to represent them by decorrelated parameters, even though the rotation matrix required to decorrelate them is close to an identity matrix.
- The coefficients c_{HB}, c_{HW}, c_{HWB}, c_{tB} and c_{tW} are constrained in two directions through their impacts on the branching ratios of the $H \to \gamma\gamma$ and $H \to Z\gamma$ decays. There is an additional small impact of these operators on VBF and VH production, mildly constraining a third direction in this parameter group.
- The coefficients c_{Hu}, $c_{Hq}^{(1)}$, c_{Hd}, $c_{Hl,33}^{(3)}$, c_{Ht}, $c_{He,33}$, $c_{Hl,33}^{(1)}$ and c_{Hb} mainly affect the W and Z vertices with third generation fermions, as well as the neutral current interactions with quarks. They are primarily constrained by the VH, $H \to b\bar{b}$ analysis.
- The coefficients of the four-fermion operators involving the top-quark, *i.e.* $c_{Qq}^{(1,8)}$, $c_{Qq}^{(3,1)}$, $c_{tq}^{(8)}$, $c_{Qu}^{(8)}$, $c_{tu}^{(8)}$, $c_{td}^{(8)}$, $c_{Qd}^{(8)}$, $c_{Qq}^{(3,8)}$, $c_{Qq}^{(1,1)}$, $c_{tu}^{(1)}$, $c_{tq}^{(1)}$, $c_{Qu}^{(1)}$, and $c_{Qd}^{(1)}$, as well as the trilinear gluon coupling c_G, affect the $t\bar{t}H$ and tH production modes and are largely degenerate. The p_{T}^{H} spectrum measured in the $H \to \gamma\gamma$ and $H \to b\bar{b}$ channels constrains two linear combinations of these 14 coefficients. The separate constraint on tH production in the $H \to \gamma\gamma$ analysis weakly constrains a third direction in this group.
- The coefficients $c_{ll,1221}$, $c_{Hl,11}^{(3)}$, and $c_{Hl,22}^{(3)}$ primarily effectuate a shift in the Fermi constant, resulting in an overall normalisation factor across different production modes. The coefficient $c_{H\Box}$ only affects the measurements through a Higgs propagator correction and thus acts similarly as an overall scale factor in the observed cross-sections. Only a single linear combination of these four operators can be constrained from the data.
- The coefficients $c_{Hl,11}^{(1)}$, $c_{Hl,22}^{(1)}$, $c_{He,11}$ and $c_{He,22}$ introduce anomalous $HZee$ and $HZ\mu\mu$ vertices and are mainly constrained by the branching ratio of the Higgs boson decay to four leptons (electrons or muons), together with c_{HDD} (responsible for an anomalous HZZ vertex) and $c_{HQ}^{(3)}$, $c_{HQ}^{(1)}$ (leading to $HZtt$ and $HZbb$ couplings that modify the Z boson propagator).

Based on these observations, a new fit basis $\boldsymbol{c'}$ is defined that achieves both fit stability and a reasonable interpretability of the fit parameters. This basis $\boldsymbol{c'}$ is expressed in terms of single Warsaw basis coefficients c_j whenever possible, and in terms of linear combinations (denoted with e) of coefficients when necessary:

$$
\begin{aligned}
\boldsymbol{c} = \{&c_{eH,22}\} \cup \\
&\{c_{eH,33}\} \cup \\
&\{c_{Hq}^{(1)}3\} \cup \\
&\{c_{bH}\} \cup \\
&\{c_{HG}, c_{tG}, c_{tH}\} \cup \\
&\{c_{HB}, c_{HW}, c_{HWB}, c_{tB}, c_{tW}\} \cup \\
&\{c_{Hu}, c_{Hq}^{(1)}, c_{Hd}, c_{Hl,33}^{(3)}, \\
&\qquad c_{Ht}, c_{He,33}, c_{Hl,33}^{(1)}, c_{Hb}\} \cup \\
&\{c_G, c_{Qq}^{(1,8)}, c_{Qq}^{(3,1)}, c_{tq}^{(8)}, c_{Qu}^{(8)}, c_{tu}^{(8)}, c_{td}^{(8)}, \\
&\qquad c_{Qd}^{(8)}, c_{Qq}^{(3,8)}, c_{Qq}^{(1,1)}, c_{tu}^{(1)}, c_{tq}^{(1)}, c_{Qu}^{(1)}, c_{Qd}^{(1)}\} \cup \\
&\{c_{H\Box}, c_{Hl,11}^{(3)}, c_{Hl,22}^{(3)}, c_{ll,1221}\} \cup \\
&\{c_{Hl,11}^{(1)}, c_{Hl,22}^{(1)}, c_{He,11}, c_{He,22}, c_{HDD}, c_{HQ}^{(3)}, c_{HQ}^{(1)}\}
\end{aligned}
\qquad
\begin{aligned}
\boldsymbol{c}' = \{&c_{eH,22}\} \cup \\
&\{c_{eH,33}\} \cup \\
&\{c_{Hq}^{(1)}3\} \cup \\
&\{c_{bH}\} \cup \\
\rightarrow\ &\{e_{\text{ggF}}^{[1]}, e_{\text{ggF}}^{[2]}, e_{\text{ggF}}^{[3]}\} \cup \\
\rightarrow\ &\{e_{H\gamma\gamma,Z\gamma}^{[1]}, e_{H\gamma\gamma,Z\gamma}^{[2]}, e_{H\gamma\gamma,Z\gamma}^{[3]}\} \cup \\
\rightarrow\ &\{e_{ZH}^{[1]}, e_{ZH}^{[2]}, e_{ZH}^{[3]}, e_{ZH}^{[4]}\} \cup \\
\rightarrow\ &\{e_{\text{ttH}}^{[1]}, e_{\text{ttH}}^{[2]}, e_{\text{ttH}}^{[3]}\} \cup \\
\rightarrow\ &\{e_{\text{glob}}^{[1]}\} \cup \\
\rightarrow\ &\{e_{Hllll}^{[1]}\}.
\end{aligned}
$$

Only subgroup eigenvectors with an expected uncertainty ≤ 10 are retained as model parameters, while the coefficients of the eigenvectors with larger expected uncertainties are fixed to zero in the likelihood function. The subgroup eigenvector directions relative to the Warsaw basis are shown in Figure 8. The names of the eigenvectors have been chosen to reflect the production or decay process that dominates the experimental sensitivity of the parameter group, as shown in Figure 5, although single parameters within some of the groups sometimes have a dominant sensitivity to another process.

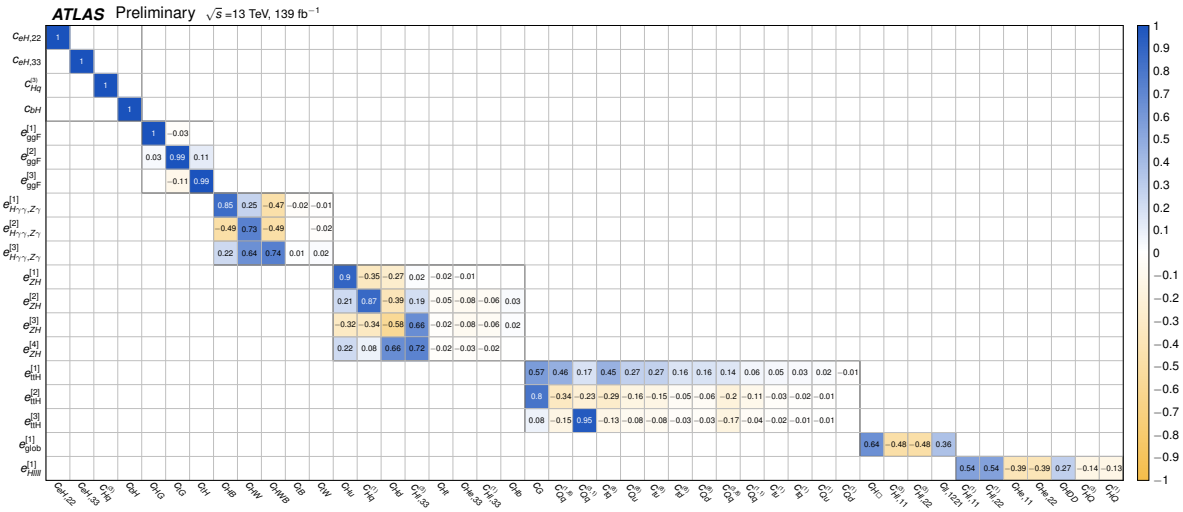

Figure 8: Definition of the fit basis coefficients $\boldsymbol{c}'$ in terms of the Warsaw basis coefficients $\boldsymbol{c}$.

No separate optimisation of the parameter basis $\boldsymbol{c}'$ is performed for the linear+quadratic SMEFT model of Eq. (13) as the non-linear effects of this model are expected to vanish for small c_j, and thus to asymptotically

yield the same rotation matrix as Eq. (15).

The impacts of the variations of the coefficients of the rotated basis $\boldsymbol{c'}$ on the STXS regions and Higgs boson branching ratios are shown in Figure 9, with the same parameter grouping as shown in Figure 5. The figure clearly demonstrates that the basis $\boldsymbol{c'}$ represents impact variations across regions that are much less correlated than those represented by the Warsaw basis $\boldsymbol{c}$. The magnitude of the parameter variations shown in Figure 9 are set to the *expected uncertainty* for each parameter in the linear SMEFT model, thus giving a realistic indication of the magnitude of variations that can be constrained from the data. For completeness, the impact of the quadratic terms for the same values of the parameter basis is overlaid, indicating the relative magnitude of the quadratic terms at the expected sensivity level of the linear model.

3.2.2 Results

Linear model Figure 10 compares the expected and observed results obtained using the linearised SMEFT model, showing good agreement of the observed data with the SM expectation, corresponding to a p-value of 94.5%. The parameter value ranges shown in the bottom panel correspond to 68% and 95% confidence level (CL) intervals, where all other coefficients and nuisance parameters are profiled. The observed uncertainties are generally about 10% smaller than the expected uncertainties, due to the fact that the assumed Higgs boson width, when computed with the observed parameter values, is smaller than its SM expection value. This effect is mostly driven by a high observed value of c_{bH}, which corresponds to a reduced value of $\Gamma^{H\to b\bar{b}}$. This reduction of the observed linear model uncertainties is comparable to that of the reduced observed uncertainties in the κ model analysis of the same data reported in Ref. [9], due to an equivalently low measurement of κ_b.

Figure 10 also shows the contributions of each measured Higgs decay or production mode to the sensitivity of each measurement of the coefficients of the rotated basis. The contribution of a measurement i to the sensitivity for a coefficient c'_j is determined from the ratio of the Fisher information $\mathcal{I}_i(c'_j)$ of that measurement to the sum of the Fisher information of all contributing components, i.e. $\sum_k \mathcal{I}_k(c'_j)$, where in all cases the Fisher information is estimated as the inverse of the covariance matrix V_{SMEFT}, as defined in Eq. (14). This breakdown reveals that six parameters are (almost) exclusively measured by a single decay mode: the Yukawa coefficients $c_{He,22}$ and $c_{He,33}$ by the decay modes $H\to\mu\mu$ and $H\to\tau\tau$ respectively; the coefficient $c^{(3)}_{Hq}$ by $H\to b\bar{b}$; coefficients $e^{[1]}_{H\gamma\gamma,Z\gamma}$ and $e^{[2]}_{H\gamma\gamma,Z\gamma}$ by $H\to\gamma\gamma$ and $H\to Z\gamma$ respectively; the coefficient $e^{[1]}_{Hllll}$ by $H\to ZZ^*$. Due to its large effect on the Higgs boson width, the measurement of the Yukawa coefficient c_{bH} is not dominated by $H\to b\bar{b}$, but instead constrained by a combination of measured decays. Similarly, five parameters are measured (almost) exclusively by a single production mode: coefficient $e^{[1]}_{\text{ggF}}$ by ggF production, $e^{[1]}_{ZH}$ by ZH production, $e^{[1]}_{\text{ttH}}$ and $e^{[2]}_{\text{ttH}}$ by ttH production at high-p_{T} and medium-p_{T} respectively, and $e^{[3]}_{\text{ttH}}$ by tH production. No measured coefficient is predominantly sensitive to $H\to WW^*$ decays, or to the VBF or WH production modes.

Analysis of parameter uncertainty sources Figure 11 illustrates the relative importance of the various uncertainty components on the coefficients measured in the linearised model, where the top panel shows the relative contributions of the statistical and systematic components, and the bottom panel shows the relative contributions of the experimental, signal theory and background theory contributions to the total systematic uncertainty, where signal theory systematic uncertainties include both total cross-section uncertainties and acceptance uncertainties.

For parameters $c_{He,33}$, $e^{[1]}_{\text{glob}}$ and $e^{[1]}_{Hlll}$, the fractional contribution of systematic uncertainties is close to 50%; for parameters $e^{[1]}_{\text{ggF}}$, $e^{[2]}_{\text{ggF}}$, $e^{[1]}_{\text{ttH}}$ and $e^{[2]}_{\text{ttH}}$, the fractional contribution of systematic uncertainties is around 40%; the remaining parameters have smaller relative systematic uncertainties. In particular, the uncertainties in the $c_{He,22}$ and $e^{[3]}_{\text{ttH}}$ parameters, probed by the measurements the rare processes of $H \to \mu\mu$ decay and tH production, respectively, are almost completely dominated by the statistical component. The total systematic uncertainty of most parameters is dominated by experimental systematic uncertainties, with the exception of $e^{[1]}_{\text{ggF}}$ and $e^{[1]}_{\text{glob}}$, where signal theory systematic uncertainties dominate, and $e^{[2]}_{\text{ggF}}$, $e^{[1]}_{\text{ttH}}$ and $e^{[2]}_{\text{ttH}}$, where background theory systematic uncertainies dominate. The breakdown of the uncertainty components, including a breakdown of the systematic uncertainty into experimental, signal theory and background theory components, is also given in Tables 3 and 4.

The expected and observed correlation matrices are shown in Figure 12, and show a reasonably good decorrelation achieved between the fit basis parameters: over half of the off-diagonal elements are smaller than 0.1 and over 85% are smaller than 0.3 in both the observed and expected matrix. A few exceptions stand out, notably the correlation between $e^{[2]}_{\text{ggF}}$ and $e^{[1]}_{\text{ttH}}$ and between $e^{[3]}_{\text{ggF}}$ and $e^{[1]}_{H\gamma\gamma,Z\gamma}$, which are caused by a common sensitivity to $t\bar{t}H$ production and ggF $H \to \gamma\gamma$, respectively.

Linear+quadratic model Figure 13 compares the expected and observed results obtained using the SMEFT model including quadratic terms, showing again good agreement of the observed data with the SM expectation, corresponding to a p-value of 98.2%. For most parameters, the observed uncertainty is noticeably smaller than the expected uncertainty. The cause of this discrepancy is related to appearance of quadratic parameter terms in the cross-section predictions, which cause the likelihood function to generally have multiple minima in each parameter. In the expected result, most close-by minima that are exactly degenerate with the global minimum merge into a single wider uncertainty interval. Conversely, in the observed result, the generally non-zero observed coefficient values lift some of these minima to become local minima, thereby resulting in a narrower interval around the remaining global minimum. This effect can be clearly seen in more detail in the profile likelihood scans of each parameter, shown in Figures 14 and 15. Most secondary minima are raised by 1-2 units in $-2\log L$, thus narrowing the 68% confidence intervals, which are based on a unit threshold, but less so the 95% confidence intervals based on a 3.84 unit threshold. For all parameters with multiple solutions, the global minimum in the observed result resolves to the minimum closest to a coefficient value of zero, with the exception of parameter $e^{[1]}_{H\gamma\gamma,Z\gamma}$, where the minimum furthest from zero becomes the global minimum. For the parameter $c_{eH,22}$, there are two exactly degenerate minima. In that case, the minimum closest to that of the interpretation with the linear model is quoted as the best-fit result.

Almost all profile likelihood functions exhibit Gaussian behavior to a good approximation within the 95% CL range of each parameter, although this is masked by the appearance of degenerate solutions. The only exception is the expected profile likelihood for the $e^{[3]}_{\text{ttH}}$ parameter in the linearised model, where a boundary occurs at $e^{[3]}_{\text{ttH}} = -10$, just before the likelihood threshold of the 95% CL is reached. Here, the yield prediction in the high-p_{T} region of the $t\bar{t}H$, $H\to\gamma\gamma$ channel becomes negative for very negative values of $e^{[3]}_{\text{ttH}}$, rendering the likelihood undefined beyond that point. The 95% CL interval for $e^{[3]}_{\text{ttH}}$ shown in Figures 10 and 16 has been truncated at this boundary, resulting in a small undercoverage.

Comparison between the linearised and the linear+quadratic models Figure 16 compares the results for the linearised model and the model with quadratic terms for the observed data and shows that for several

of the coefficients the constraints from the model with the quadratic terms are significantly stronger than those observed for the linear model. In most cases the stronger constraints arise from the relatively weak impact of the BSM-SM interference term on the cross-section compared to the quadratic BSM terms in specific production or decay modes.

Figure 9 illustrates the impact of both the linear model and the model with quadratic terms, where the impact strength visualised for *both* models corresponds to the expected 68% uncertainty of each fit basis parameter c' under the linear model. Comparatively larger impacts of the linear+quadratic model at these chosen parameter values identify STXS regions where quadratic terms outweigh the linear terms at the measured scale and thus identify regions that predominantly provide the extra constraining power of the linear+quadratic models. The strongest observed sensitivity enhancements occur in $e^{[3]}_{\text{ggF}}$, $e^{[2]}_{\text{ttH}}$ and $e^{[3]}_{\text{ttH}}$. For coefficient $e^{[3]}_{\text{ggF}}$, the quadratic term significantly increases sensitivity in the ggF, ZH and $t\bar{t}H$ production modes as well as in the $H \to \gamma\gamma$ decay mode. For coefficients $e^{[2]}_{\text{ttH}}$ and $e^{[3]}_{\text{ttH}}$, the quadratic term enhances sensitivity in high-p_{T} $t\bar{t}H$ production and tH production, respectively. Conversely, for the coefficients $e^{[2]}_{\text{ggF}}$ and $e^{[3]}_{H\gamma\gamma,Z\gamma}$, the effect of the increased impacts of the quadratic terms is limited, and the strong reduction in uncertainties is mostly driven by the lifting of degenerate solutions, as visible in the profile likelihood scans in Figure 14.

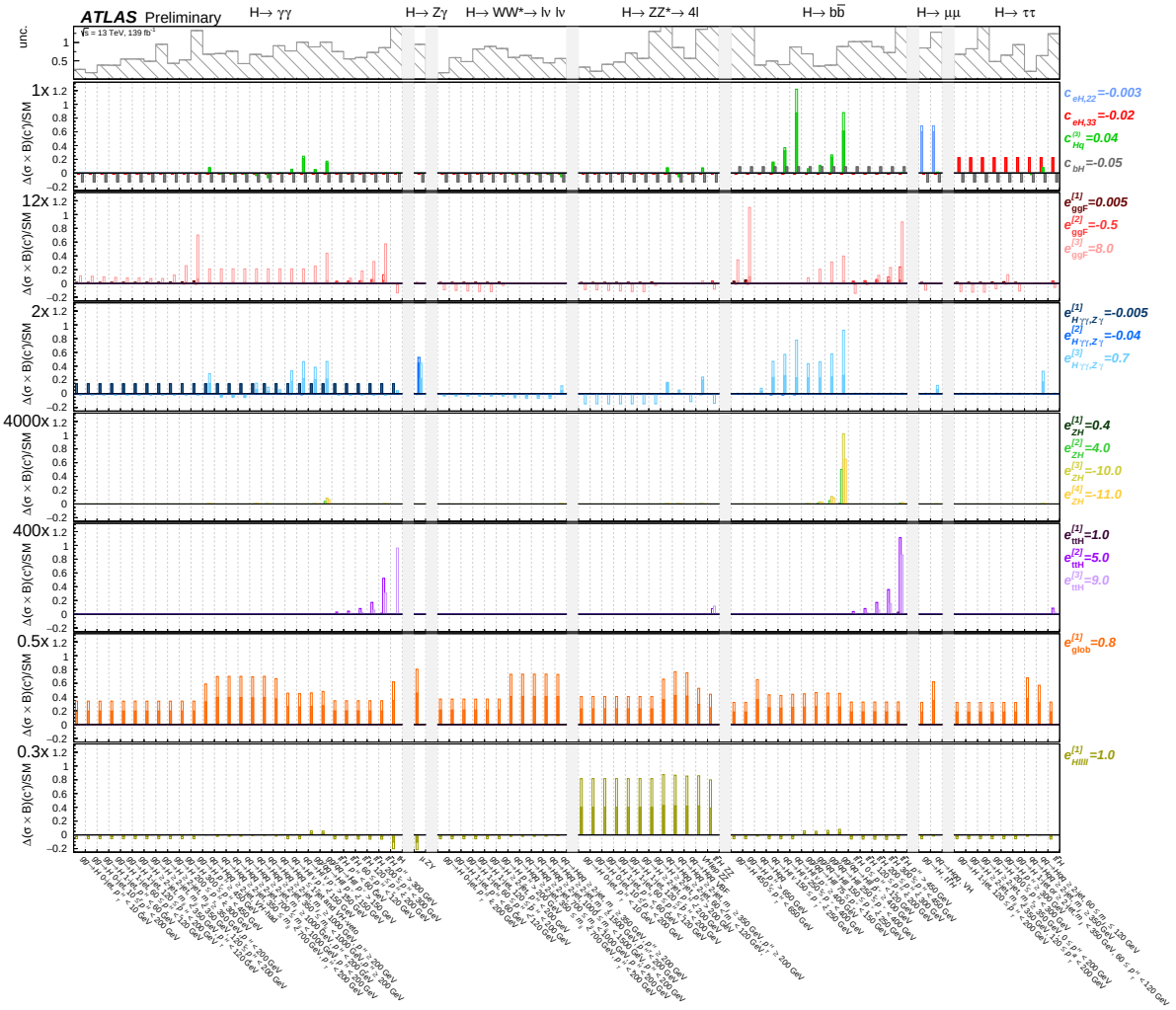

Figure 9: Impact of coefficients of the rotated basis $\boldsymbol{c'}$ on the STXS regions, relative to the SM cross-section, under the assumption of the linearised SMEFT model (shaded histogram) and the linear+quadratic SMEFT model (open histogram). For all coefficients, a variation equal to the expected uncertainty when using the linearised model is shown. Groupings in this figure are consistent with those in Figure 5, but vertical axis scales differ in order to completely show all quadratic impact terms, which can occasionally be very large. To judge the experimental sensitivity to constrain the operators from the data in the listed STXS regions, the total uncertainty on the corresponding regions is shown in the top panel. For presentational clarity, the uncertainty of low precision STXS regions is clipped off in the plot.

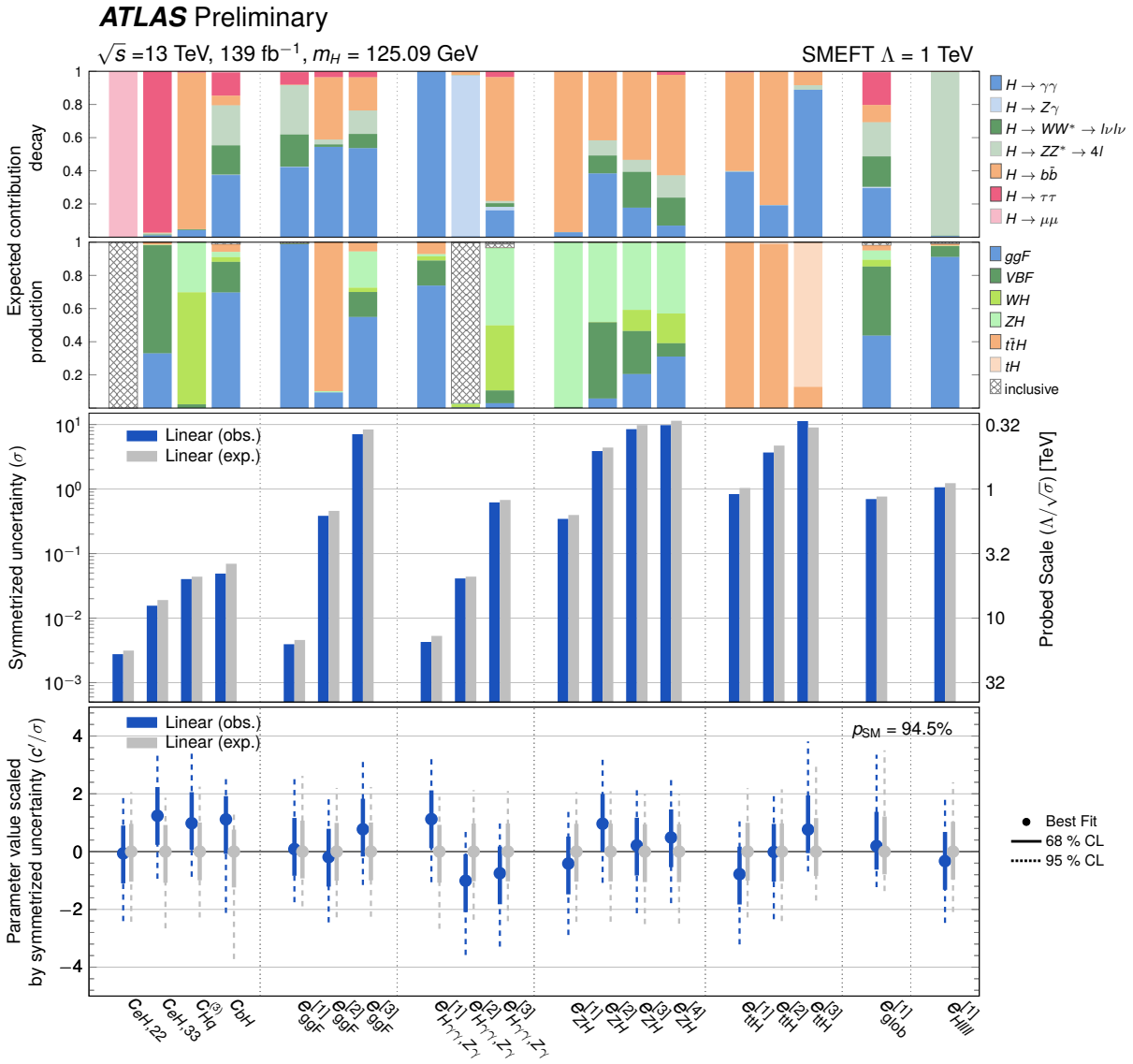

Figure 10: Comparison of the expected (gray) and observed (blue) parameters of the rotated basis $\boldsymbol{c}'$ with the SMEFT linearised model, where all other coefficients and nuisance parameters are profiled. The middle panel shows the symmetrised 68% CL uncertainty σ of each parameter measurement (left vertical axis) and the corresponding energy scale $\Lambda/\sqrt{s}$, $\Lambda = 1$ TeV that is probed (right vertical axis). The bottom panel shows the measured parameter value (dot), 68% (solid line) and 95% (dashed line) CL intervals, divided by the symmetrised uncertainty shown in the middle panel. The p-value for the compatibility of the data with the Standard Model expectation (all coefficients vanishing) is 94.5%. The top panel shows the expected breakdown of contributions to the sensitivity of each measurement from the various measured Higgs boson decay and production modes. Green shades represent production and decay modes with Higgs boson couplings to vector bosons, red shades represent modes with Higgs boson couplings to fermions, and blue shades represent modes with loop couplings. The production category labeled 'inc' collects final states for which the breakdown into production modes is not available ($H \to \mu\mu$ and $H \to Z\gamma$). The 95% CL interval for $e^{[3]}_{\mathrm{ttH}}$ has been truncated at the boundary at which the logarithm of the likelihood function becomes undefined, resulting in a small undercoverage.

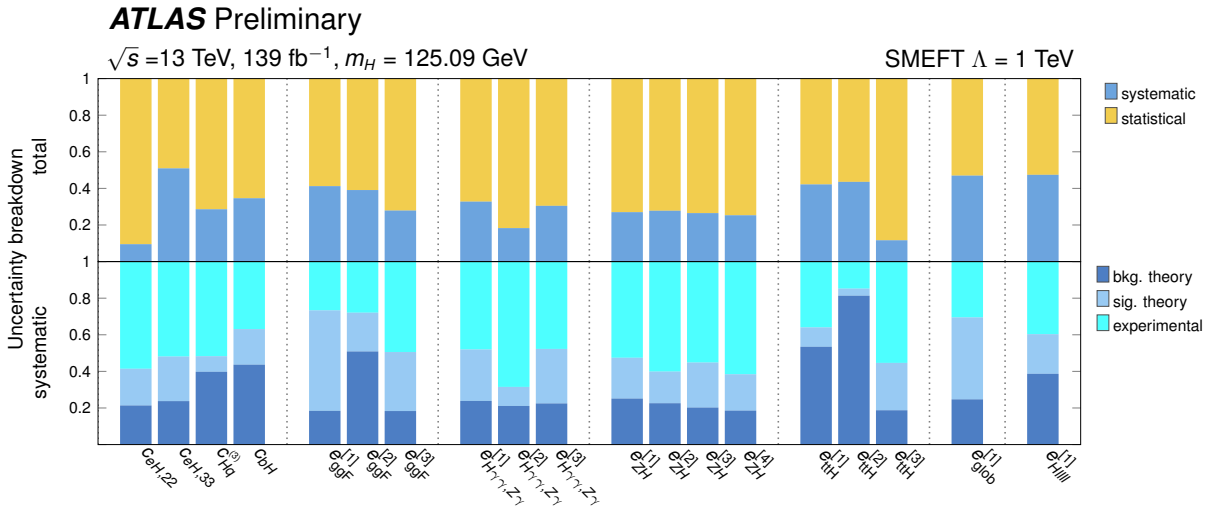

Figure 11: Expected fractional contributions of the statistical (orange) and systematic (blue) uncertainties to the total uncertainty on the measurements of the parameters of the rotated basis $\boldsymbol{c}'$ with the SMEFT linearised model (top panel), and the corresponding expected fractional contributions of experimental (cyan), signal theory (light blue) and background theory (dark blue) uncertainties to the total systematic uncertainty (bottom panel).

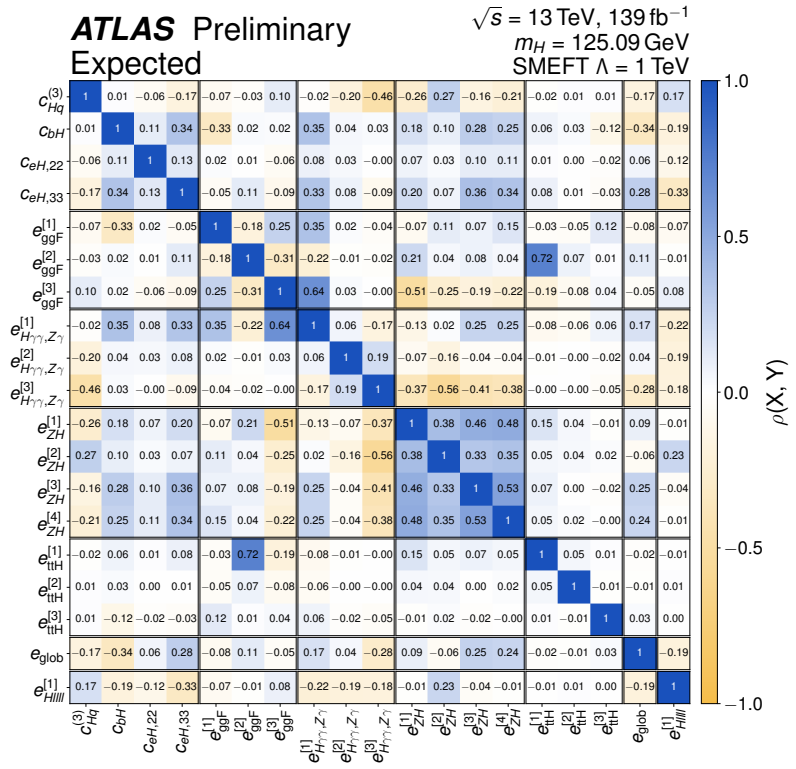

(a)

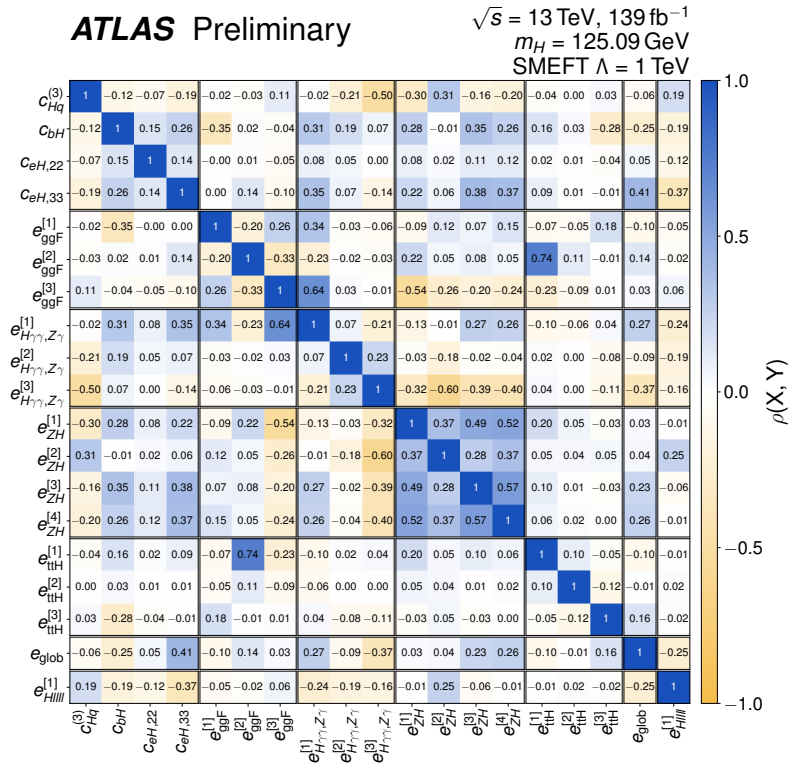

(b)

Figure 12: The (a) expected and (b) observed correlation matrix for the parameters of the rotated basis $\boldsymbol{c}'$ obtained from a fit to the linearised SMEFT model.

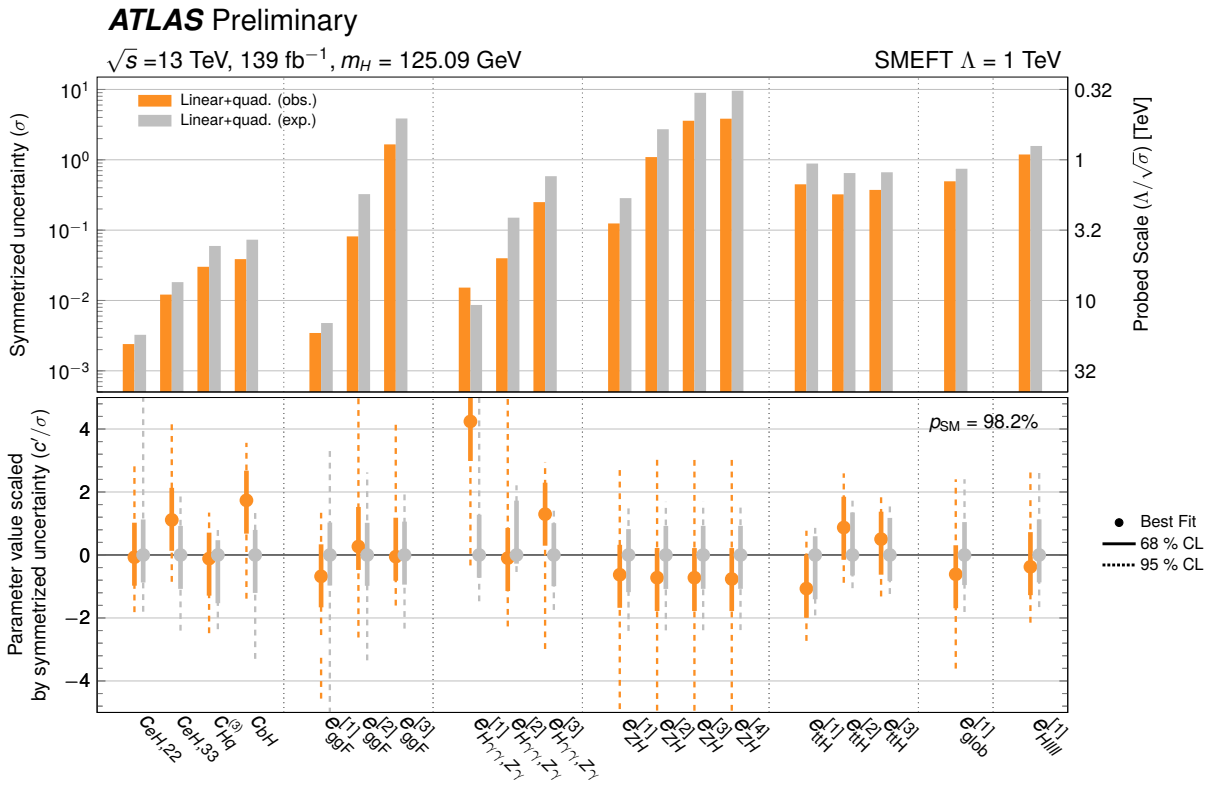

Figure 13: Comparison of the expected (gray) and observed (blue) parameters of the rotated basis $\boldsymbol{c}'$ with the SMEFT model with quadratic terms, where all other coefficients and nuisance parameters are profiled. The top panel shows the symmetrised 68% uncertainty σ of each parameter measurement (left vertical axis) and the corresponding energy scale $\Lambda/\sqrt{\sigma}$, $\Lambda = 1$ TeV that is probed (right vertical axis). The bottom panel shows the measured parameter value, 68% (solid) and 95% (dashed) CL intervals, divided by the symmetrised uncertainty shown in the top panel. Some of the observed intervals shown are clipped off. Due to multiple minima the likelihood curves from which these CL intervals are derived are non parabolic. For the parameter $c_{eH,22}$, for which there are two degenerate minima in the interpretation with the model including quadratic terms, the point corresponds to the best-fit value that is closest to that of the interpretation with the linear model.

Operators in Warsaw basis: $c_{eH,22}$, $c_{eH,33}$, $c^{(3)}_{Hq}$ and c_{bH}

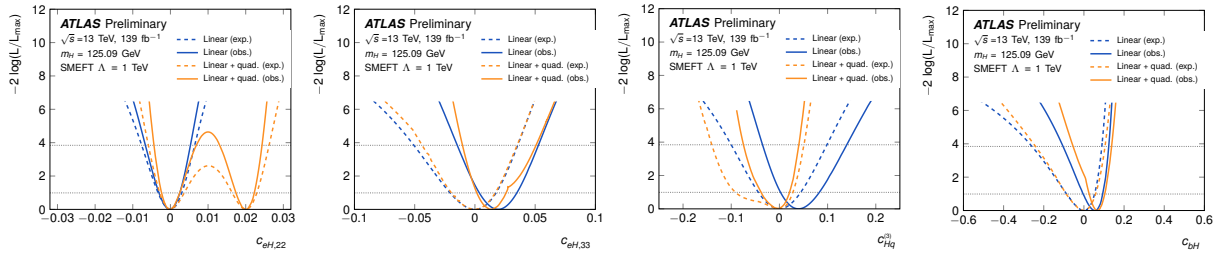

(a) (b) (c) (d)

Eigenvector group ggF

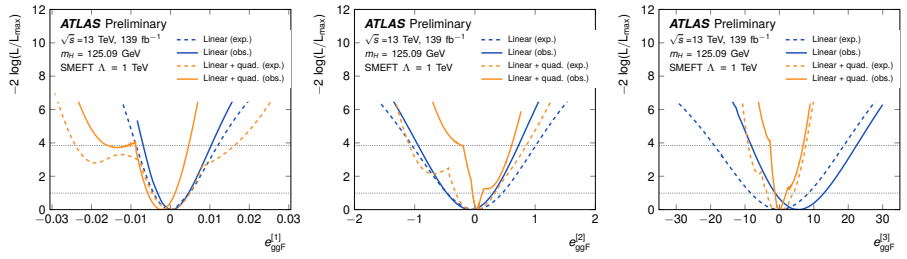

(e) (f) (g)

Eigenvector group $H \to \gamma\gamma, Z\gamma$

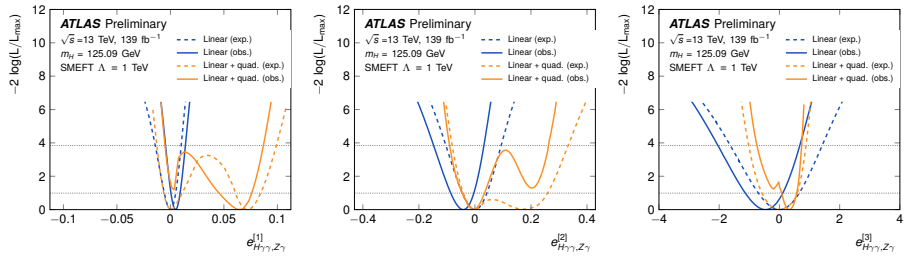

(h) (i) (j)

Eigenvector group ZH

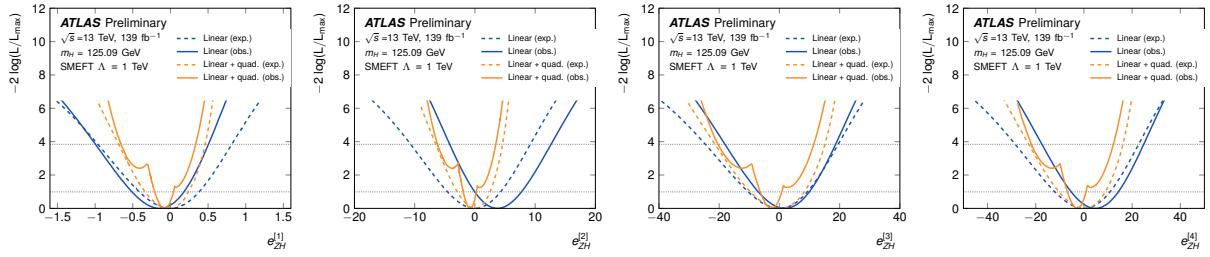

(k) (l) (m) (n)

Figure 14: Profile likelihood scans of the fitted coefficients of the rotated basis $\boldsymbol{c'}$ obtained from fits to the SM expection (dashed lines) and to the observed data (solid lines), based on the SMEFT linearised model (blue) and the SMEFT model with quadratic terms (orange). The horizontal dashed lines in each plot correspond to the asymptotic threshold values for 68% and 95% CL intervals. The profile likelihood scans of the SMEFT model with quadratic terms can exhibit two minima in the scanned parameter, whereas the scans of the linearised model have one minimum per parameter. Multiple minima in the coefficients that are profiled in each scan may furthermore result in discontinuous derivatives in the profile likelihood (e.g. prominently visible in the observed data in (e) and (l)).

Eigenvector group *top*

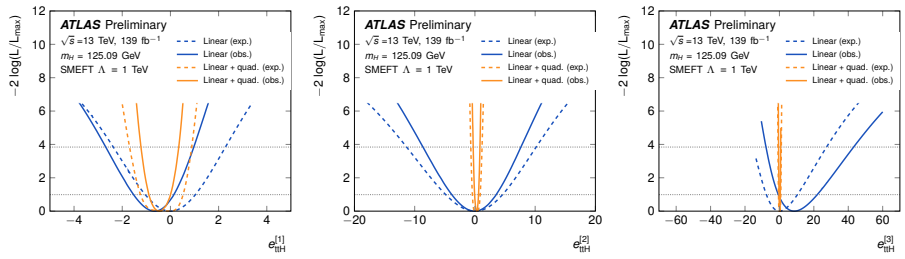

(a) (b) (c)

Eigenvector group *overall normalization*

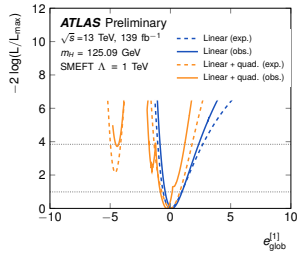

(d)

Eigenvector group $H \to ZZ^*$

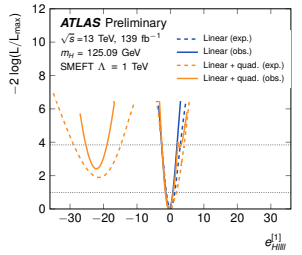

(e)

Figure 15: Profile likelihood scans of the fitted coefficients of the rotated basis $\boldsymbol{c}'$ obtained from fits to the SM expected (dashed lines) and to the observed data (solid lines), based on the SMEFT linearised model (blue) and the SMEFT model with quadratic terms (orange). The horizontal dashed lines in each plot correspond to the asymptotic threshold values for 68% and 95% CL intervals. The profile likelihood scans of the SMEFT model with quadratic terms can exhibit two minima in the scanned parameter, whereas the scans of the linearised model can only have one minimum per parameter. Multiple minima in the coefficients that are profiled in each scan may furthermore result in discontinuous derivatives in the profile likelihood (e.g. prominently visible in the observed data in (d)).

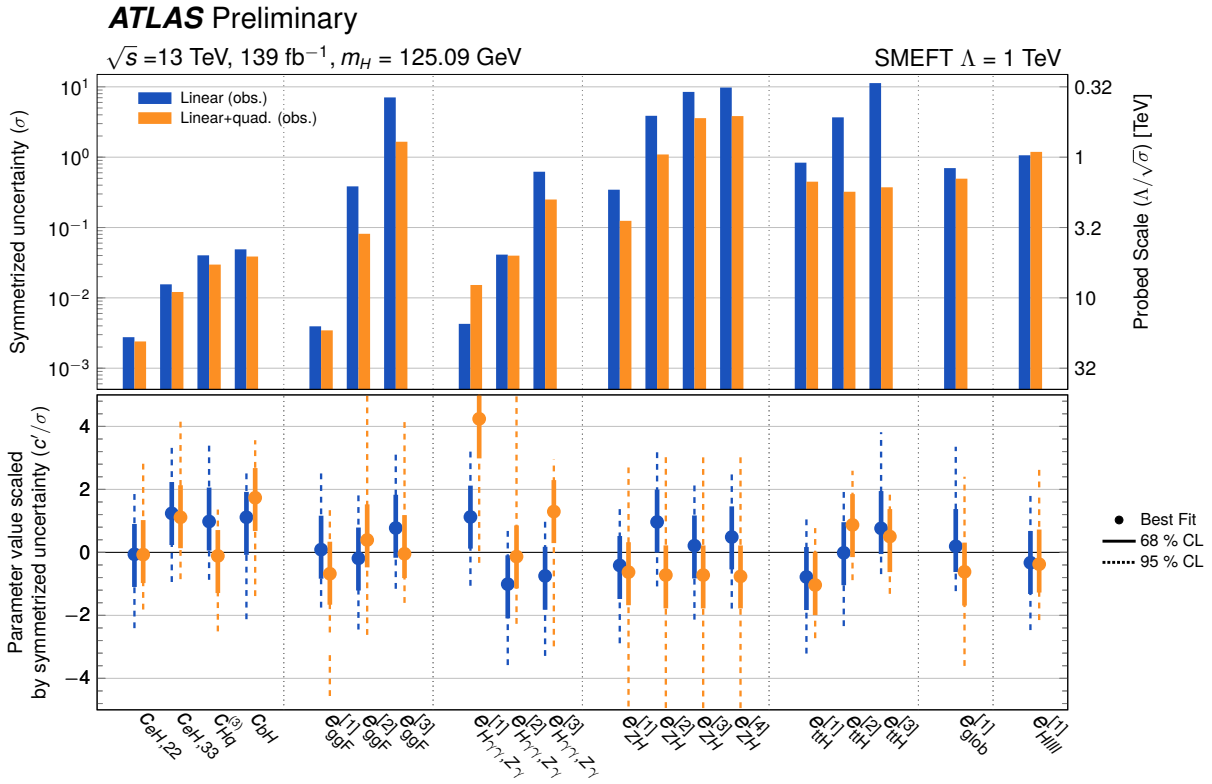

Figure 16: Comparison of the observed parameters of the rotated basis $\boldsymbol{c}'$ with the SMEFT linearised model (blue) and the model including quadratic terms (orange), where all other coefficients and nuisance parameters are profiled. The top panel shows the symmetrised 68% CL uncertainty σ of each parameter measurement (left vertical axis) and the corresponding energy scale $\Lambda/\sqrt{s}$, Λ = 1 TeV that is probed (right vertical axis). The bottom panel shows the measured parameter value, 68% (solid) and 95% (dashed) CL intervals, divided by the symmetrised uncertainty shown in the top panel. Some of the intervals shown for the model with quadratics terms are clipped off. Due to multiple minima the likelihood curves from which these CL intervals are derived are non parabolic. The 95% CL interval for $e^{[3]}_{\text{ttH}}$ has been truncated at the boundary at which the log likelihood becomes undefined, resulting in a small undercoverage. For the parameter $c_{eH,22}$, for which there are two degenerate minima in the interpretation with the model including quadratic terms, the point corresponds to the best-fit value that is closest to that of the interpretation with the linear model.

Table 3: Summary of the observed measurements of the parameters of the rotated basis $\boldsymbol{c}'$ in the SMEFT linearised model, with a breakdown of the total uncertainty into statistical and systematic components. A further breakdown of the systematic uncertainty into experimental and theoretical uncertainties on the signal and background is also listed. All MC statistical uncertainties are classified as experimental systematic uncertainties in the breakdown. All uncertainties correspond to 68% CL intervals. The sum in quadrature of the systematic uncertainty components may differ from the total systematic uncertainty due to correlations.

Parameter	Value	σ_{tot}	σ_{stat}	σ_{syst}	$\sigma_{\text{syst}}^{\text{exp}}$	$\sigma_{\text{syst}}^{\text{th.sig}}$	$\sigma_{\text{syst}}^{\text{th.bkg}}$
$c_{eH,22}$	-0.0002	0.0028	0.0026	0.0009	0.0006	$^{+0.0005}_{-0.0003}$	0.0005
$c_{eH,33}$	0.019	0.016	0.011	0.011	0.008	0.005	0.006
$c_{Hq}^{(3)}$	0.039	0.040	0.034	0.021	0.015	0.012	$^{+0.005}_{-0.011}$
c_{bH}	0.055	$^{+0.058}_{-0.039}$	$^{+0.045}_{-0.032}$	$^{+0.037}_{-0.023}$	$^{+0.022}_{-0.014}$	$^{+0.025}_{-0.013}$	0.015
$e_{\text{ggF}}^{[1]}$	0.0003	0.0039	0.0029	0.0026	0.0013	$^{+0.0008}_{-0.0013}$	0.0021
$e_{\text{ggF}}^{[2]}$	-0.07	0.38	0.29	0.25	0.13	0.18	0.11
$e_{\text{ggF}}^{[3]}$	5.5	7.1	5.8	4.0	2.7	1.6	$^{+2.1}_{-2.8}$
$e_{H\gamma\gamma,Z\gamma}^{[1]}$	0.0048	0.0043	0.0034	0.0026	0.0017	0.0012	0.0015
$e_{H\gamma\gamma,Z\gamma}^{[2]}$	-0.042	0.041	0.037	$^{+0.022}_{-0.015}$	0.014	$^{+0.010}_{-0.006}$	$^{+0.011}_{-0.006}$
$e_{H\gamma\gamma,Z\gamma}^{[3]}$	-0.47	0.62	0.51	0.35	0.24	0.16	0.20
$e_{ZH}^{[1]}$	-0.14	0.34	0.29	0.19	0.16	$^{+0.11}_{-0.08}$	0.09
$e_{ZH}^{[2]}$	3.7	3.9	3.3	2.1	1.6	1.0	0.9
$e_{ZH}^{[3]}$	1.8	8.5	7.2	4.5	3.4	2.0	2.2
$e_{ZH}^{[4]}$	4.8	9.8	8.2	5.2	4.0	2.2	2.5
$e_{\text{ttH}}^{[1]}$	-0.65	0.84	0.64	0.54	0.31	0.41	0.17
$e_{\text{ttH}}^{[2]}$	-0.05	3.7	2.8	2.4	0.94	2.2	$^{+0.3}_{-0.6}$
$e_{\text{ttH}}^{[3]}$	8.6	$^{+9.2}_{-13.4}$	$^{+8.8}_{-12.1}$	$^{+2.9}_{-5.7}$	$^{+2.1}_{-3.9}$	$^{+1.2}_{-2.0}$	$^{+1.5}_{-3.8}$
$e_{\text{glob}}^{[1]}$	0.13	$^{+0.57}_{-0.83}$	$^{+0.42}_{-0.57}$	$^{+0.38}_{-0.60}$	$^{+0.20}_{-0.30}$	$^{+0.17}_{-0.29}$	$^{+0.29}_{-0.42}$
$e_{Hllll}^{[1]}$	-0.35	1.1	0.76	0.74	0.44	0.46	0.38

Table 4: Summary of the expected measurements of the parameters of the rotated basis $\boldsymbol{c}'$ with the SMEFT linearised model, with a breakdown of the total uncertainty into a statistical and systematic component. A further breakdown of the systematic uncertainty into experimental and theoretical uncertainties on the signal and background respectively is also listed. All MC statistical uncertainties are classified as experimental systematic uncertainties in the breakdown. All uncertainties correspond to 68% CL intervals. The sum in quadrature of the systematic uncertainty components may differ from the total systematic uncertainty due to correlations.

Parameter	Value	σ_{tot}	σ_{stat}	σ_{syst}	$\sigma_{\text{syst}}^{\text{exp}}$	$\sigma_{\text{syst}}^{\text{th.sig}}$	$\sigma_{\text{syst}}^{\text{th.bkg}}$
$c_{eH,22}$	0.0	0.0031	0.0030	0.0010	0.0007	$^{+0.0006}_{-0.0004}$	$^{+0.0005}_{-0.0004}$
$c_{eH,33}$	0.0	0.019	0.013	0.014	0.010	0.007	0.007
$c_{Hq}^{(3)}$	0.0	0.044	0.037	0.023	0.017	0.015	0.007
c_{bH}	0.0	$^{+0.09}_{-0.05}$	$^{+0.07}_{-0.04}$	$^{+0.06}_{-0.03}$	$^{+0.033}_{-0.02}$	$^{+0.04}_{-0.02}$	$^{+0.02}_{-0.01}$
$e_{\text{ggF}}^{[1]}$	0.0	0.0046	0.0035	0.0029	0.0015	$^{+0.0011}_{-0.0015}$	0.0022
$e_{\text{ggF}}^{[2]}$	0.0	0.46	0.36	0.29	0.15	0.20	0.13
$e_{\text{ggF}}^{[3]}$	0.0	8.4	7.1	4.4	3.1	1.9	2.5
$e_{H\gamma\gamma,Z\gamma}^{[1]}$	0.0	0.0057	0.0043	0.0030	0.0021	$^{+0.0018}_{-0.0012}$	0.0016
$e_{H\gamma\gamma,Z\gamma}^{[2]}$	0.0	0.044	0.040	0.019	0.016	0.009	$^{+0.007}_{-0.005}$
$e_{H\gamma\gamma,Z\gamma}^{[3]}$	0.0	0.68	0.56	0.37	0.25	0.17	$^{+0.15}_{-0.25}$
$e_{ZH}^{[1]}$	0.0	0.40	0.34	0.21	0.15	0.10	0.10
$e_{ZH}^{[2]}$	0.0	4.4	3.7	2.3	1.8	1.10	0.96
$e_{ZH}^{[3]}$	0.0	9.8	8.4	5.0	3.7	2.3	2.5
$e_{ZH}^{[4]}$	0.0	11	9.9	5.7	4.5	2.5	2.6
$e_{\text{ttH}}^{[1]}$	0.0	1.0	0.79	0.68	0.40	0.49	0.22
$e_{\text{ttH}}^{[2]}$	0.0	4.7	3.5	3.1	1.2	2.8	0.61
$e_{\text{ttH}}^{[3]}$	0.0	$^{+7.6}_{-10.4}$	$^{+7.0}_{-10.0}$	3.02	2.25	$^{+1.51}_{-0.97}$	$^{+1.30}_{-1.79}$
$e_{\text{glob}}^{[1]}$	0.0	$^{+0.60}_{-0.93}$	$^{+0.46}_{-0.64}$	$^{+0.39}_{-0.67}$	0.28	$^{+0.18}_{-0.35}$	$^{+0.23}_{-0.49}$
$e_{Hllll}^{[1]}$	0.0	1.23	0.89	0.85	0.54	0.53	0.39

3.3 Constraints from fiducial differential measurements

Anomalous couplings of the Higgs boson to gluons and top quarks, as well as between gluons and top-quarks, can affect the total Higgs boson production cross-section and its dependence on the Higgs boson transverse momentum. The expected deviations from the SM predictions due to these anomalous couplings can be relatively large in high Higgs boson p_{T} regions, which are also characterised by a better signal-to-background ratio, making the p_{T}^{H}-differential cross-section measurement more sensitive to these effects compared to a measurement of the inclusive rate.

3.3.1 Sensitivity estimate and choice of parameters

In this study, constraints on anomalous Higgs boson couplings to gluons and top quarks are set from the observed transverse momentum differential spectra of the Higgs boson decay products in the $H\to ZZ^{*}\to 4\ell$ and $H\to\gamma\gamma$ decay channels. The constraints are inferred using an EFT approach in which the SM Lagrangian is augmented with the three dimension-6 SMEFT operators O_{HG} (Higgs-gluon point-like contact term), O_{tH} (top quark Yukawa coupling modifier) and O_{tG} (chromomagnetic dipole operator), that are defined in Table 2. The operator O_{HG} introduces an Hgg contact interaction that modifies the value and p_{T}-dependence of the ggF production cross-section, as well as the $H\to gg$ partial decay width, thus affecting indirectly the $H\to ZZ^{*}\to 4\ell$ and $H\to\gamma\gamma$ branching ratios. The operator O_{tH} modifies the $t\bar{t}H$ vertex and thus affects Higgs boson production through top-quark-loop mediated gluon-gluon fusion or in association with a $t\bar{t}$ pair, as well as the top-quark-loop amplitude contributing to the $H\to\gamma\gamma$ partial width. The operator O_{tG} introduces a $t\bar{t}Hg$ vertex that leads to additional contributions to the amplitude for ggF or $t\bar{t}H$ Higgs boson production, as well as for $H\to gg$ decays, affecting in turn the branching ratios for both $H\to\gamma\gamma$ and $H\to ZZ$.

The study presented in this section is performed in the scenario in which only the SM-BSM interference effects, linear in the Wilson coefficients, are considered. For simplicity, due to the statistical precision of the data sample and the very large correlations between the estimators for the three Wilson coefficients, the constraints are initially set on one Wilson coefficient at a time, while the values of the remaining coefficients are assumed to be equal to zero. Subsequently, similar to the approach presented in Section 3.2.1, a rotation in the parameter space is performed to define a new set of coefficients which are decorrelated and can be probed simultaneously. The new basis is formed by the three eigenvectors $ev^{[i]}$ (i = 1..3) of the Fisher information matrix, that are related to the three Wilson coefficients by the following rotation:

$$\begin{aligned} ev^{[1]} &= 0.999c_{HG} - 0.035c_{tG} - 0.003c_{tH}, \\ ev^{[2]} &= 0.035c_{HG} + 0.978c_{tG} + 0.205c_{tH}, \\ ev^{[3]} &= -0.005c_{HG} - 0.205c_{tG} + 0.979c_{tH}. \end{aligned}$$

The impact of the operators defining the new basis on the fiducial differential cross-sections is shown in Figure 17.

3.3.2 Results

The statistical interpretation is performed using a joint likelihood model of the data in the two decay channels, built, as described in Section 2.3, from the observed and expected values of the fiducial differential

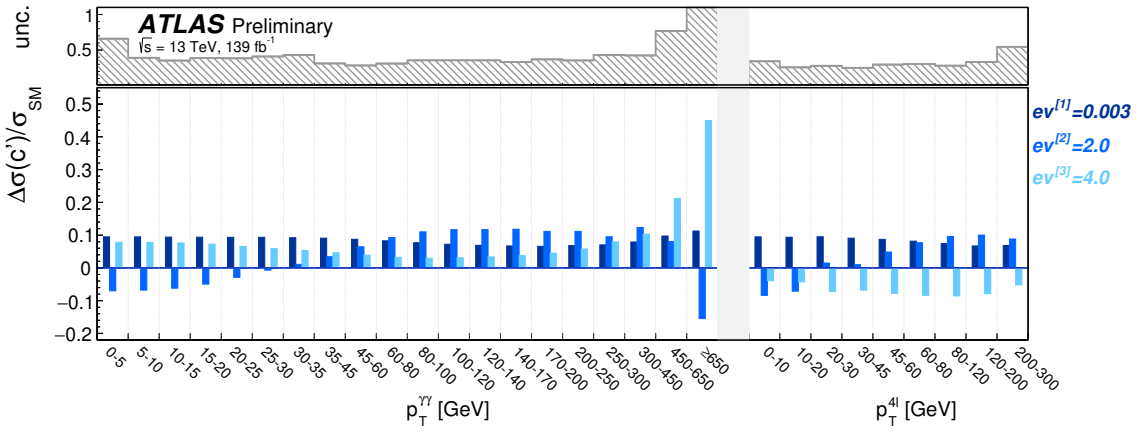

Figure 17: Impact of the rotated SMEFT operators on the fiducial cross-section differential in p_{T}^{H} in $H\to\gamma\gamma$ and $H \to ZZ^*$ decays, relative to the SM cross-section, under the assumption of the linearised SMEFT model. To judge the experimental sensitivity to constrain the operators from the data in the listed fiducial regions, the total uncertainty on the corresponding regions is shown in the top panel. For presentational clarity, the uncertainty of low precision fiducial regions is clipped off in the plot.

cross-sections in each bin of the transverse momentum of the Higgs boson decay products for both $H \to 4\ell$ and $H \to \gamma\gamma$ decays. In the likelihood function, the theoretical prediction for each decay channel and transverse momentum interval is parametrised as a function of the Wilson coefficients, as summarised in Section 3.1. The procedure assumes common higher-order corrections for the SMEFT and SM processes. The theoretical uncertainties are taken from the SM calculations in Section 2.2, with the uncertainty associated with the SMEFT scaling of those assumed to be negligible.

The 68% CL one-dimensional intervals for the three Wilson coefficients c_{HG}, c_{tG} and c_{tH}, obtained from the linearised model and when fixing the other two Wilson coefficients to zero, are summarised in Table 5. The constraints are $O(0.1\%)$, $O(10\%)$ and $O(1)$, respectively. Statistical and systematic uncertainties are of the same order of magnitude.

Table 5: Observed (second and third columns) and expected (fourth and fifth columns) 68% CL intervals for three Wilson coefficients (1st column) affecting the differential $p_{\mathrm{T}}^{4\ell}$ and $p_{\mathrm{T}}^{\gamma\gamma}$ spectra. The intervals are reported when all uncertainties (2nd and 4th columns) or only statistical uncertainties (3rd and 5th columns) are considered. The results for each parameter are obtained using the model linearised in the Wilson coefficients, fixing all the other coefficients to zero.

Parameter	Observed 68% CL interval		Expected 68% CL interval	
	stat. + syst.	stat. only	stat. + syst.	stat. only
c_{HG}	$0.000^{+0.003}_{-0.003}$	$0.000^{+0.002}_{-0.002}$	$0.000^{+0.003}_{-0.003}$	$0.000^{+0.002}_{-0.002}$
c_{tG}	$0.00^{+0.08}_{-0.09}$	$0.00^{+0.05}_{-0.05}$	$0.00^{+0.08}_{-0.09}$	$0.00^{+0.05}_{-0.05}$
c_{tH}	$0.1^{+1.0}_{-1.1}$	$0.1^{+0.7}_{-0.7}$	$0.0^{+1.0}_{-1.1}$	$0.0^{+0.7}_{-0.7}$

Table 6 shows the 68% CL one-dimensional intervals in the linearised model for the rotated parameters $ev^{[i]}$ with the other two parameters profiled. The constraint on the first rotated parameter, which is almost

aligned with c_{HG}, is of the order of 1%, while the constraints on the other two rotated parameters are $O(1)$. These constraints are shown in Figure 18, where they are compared to those obtained from the STXS measurements performed with the same decay channels using the linearised model.

Table 6: Observed (second and third columns) and expected (fourth and fifth columns) 68% CL intervals for the eigenvectors of the rotated basis of operators (1st column) affecting the differential $p_{\mathrm{T}}^{4\ell}$ and $p_{\mathrm{T}}^{\gamma\gamma}$ spectra. The intervals are reported when all uncertainties (2nd and 4th columns) or only statistical ones (3rd and 5th columns) are considered. The results for each parameter are obtained using the model linearised in the Wilson coefficients, profiling the other parameters.

Parameter	Observed 68% CL interval		Expected 68% CL interval	
	stat. + syst.	stat. only	stat. + syst.	stat. only
$ev^{[1]}$	$0.000^{+0.003}_{-0.003}$	$0.000^{+0.002}_{-0.002}$	$0.000\ ^{+0.003}_{-0.003}$	$0.000\ ^{+0.002}_{-0.002}$
$ev^{[2]}$	$0.3^{+2.1}_{-1.9}$	$0.3^{+1.4}_{-1.3}$	$0.0\ ^{+2.2}_{-1.9}$	$0.0\ ^{+1.4}_{-1.4}$
$ev^{[3]}$	$1.2^{+3.9}_{-3.9}$	$1.2^{+3.0}_{-3.2}$	$0.0\ ^{+3.8}_{-3.9}$	$0.0\ ^{+3.0}_{-3.1}$

Figure 18 illustrates that the differential cross-section measurements, which have a finer granularity compared to the STXS measurements but probe the distribution of a single observable inclusively in production mode, have less constraining power than the STXS measurements, which use information on the particles produced with the Higgs boson decay products to separate the different production modes whose cross-sections are affected in different ways by the different operators, as shown in Figure 5.

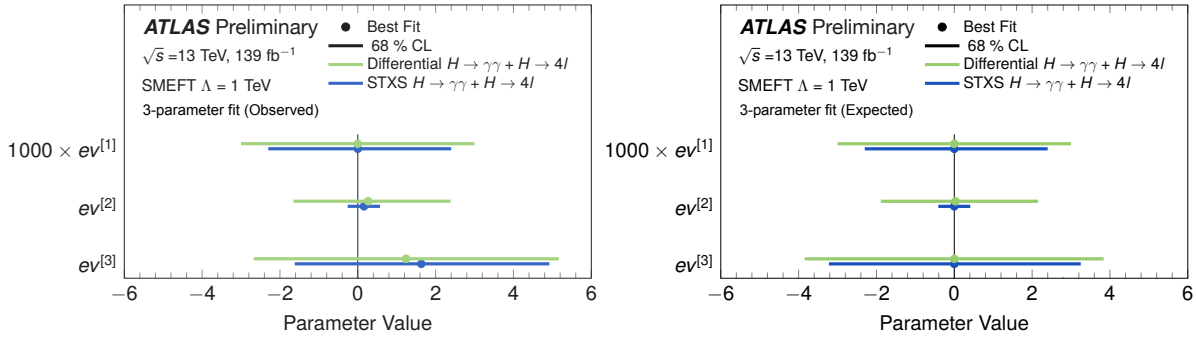

(a) (b)

Figure 18: The (a) observed and (b) expected 68% CL intervals on the three rotated parameters $ev^{[i]}$ obtained with the SMEFT linearised model using either STXS (blue) or fiducial p_{T}-differential cross-section measurements (green) in the $H \to \gamma\gamma$ and $H \to 4\ell$ decay channels. The parameter $ev^{[1]}$ is almost aligned with c_{HG}, which mainly affects ggF production, while the parameters $ev^{[2]}$ and $ev^{[3]}$ are close to c_{tG} and c_{tH} respectively, which impact both ggF and $t\bar{t}H$ production.

4 Interpretations based on UV-complete BSM models

In this section, the measurements of Higgs boson cross-sections and decay rates are interpreted in two UV-complete extensions of the Standard Model: a two-Higgs-doublet model near the alignment limit (Section 4.1), and eight benchmark scenarios of the minimal supersymmetric extension of the Standard Model (Section 4.2).

4.1 Constraints on two-Higgs-doublet models

In two-Higgs-doublet models, the SM Higgs sector with one doublet of scalar complex fields Φ_1 is extended by introducing a second doublet Φ_2 [10–12]. The models considered here assume CP conservation and a (softly-broken) Z_2 discrete symmetry that forbids quartic terms of the scalar field potential $V(\Phi_1, \Phi_2)$ that contain odd powers of either Φ_1 or Φ_2. The vacuum-expectation-values $v_{1,2}$ of the scalar doublets $\Phi_{1,2}$ that minimise V are related by the sum rule $v_1^2 + v_2^2 = v^2$. These can be assumed to be both real and non-negative without loss of generality. Electroweak symmetry breaking leads to five physical scalar Higgs fields: two neutral CP-even Higgs bosons h and H, one neutral CP-odd Higgs boson A, and two charged Higgs bosons $H^\pm$. For the results presented in this section, the observed Higgs boson is identified with the light CP-even neutral scalar particle h.

The Z_2 symmetry of the potential forbids tree-level flavour-changing neutral currents [111, 112], which are strongly constrained by existing data, and implies that all fermions with the same quantum numbers couple to only one Higgs doublet. Depending on which Higgs doublets couple to the three groups of elementary fermions (up-type and down-type quarks, and leptons), four types of 2HDM are defined:

- Type I: All fermions couple to the same Higgs doublet.
- Type II: One Higgs doublet couples to up-type quarks while the other one couples to down-type quarks and charged leptons.
- Lepton-specific: One Higgs doublet couples to leptons while the other one couples to up- and down-type quarks.
- Flipped: One Higgs doublet couples to down-type quarks while the other one couples to up-type quarks and leptons.

The Higgs sector of these models contains seven free physical parameters: four Higgs boson masses (m_h, m_H, m_A and $m_{H^\pm}$), two mixing angles α and β, and the coefficient m_{12}^2 of the $(\Phi_1^\dagger\Phi_2 + \Phi_2^\dagger\Phi_1)$ term in the Higgs field potential that softly breaks the Z_2 symmetry. The angle β is defined as $\tan\beta = \frac{v_2}{v_1}$ and can be assumed to be in the first quadrant. The mixing angle α between the two neutral CP-even Higgs states is defined modulo a phase equal to π. It can thus be assumed that $0 \leq \beta - \alpha \leq \pi$.

The values of α and β determine the couplings of the Higgs fields to the vector bosons and to the fermions. In this section, the *decoupling limit* is assumed, in which $m_H \gg v$. This in turn implies the *alignment limit*, $|\cos(\beta-\alpha)| \ll 1$, in which the light scalar Higgs boson h has SM-like couplings. The mass of the light Higgs boson m_h is assumed to be close to 125 GeV, while all other Higgs bosons are assumed to be significantly heavier (and their masses are assumed to be degenerate, $m_A \sim m_{H^\pm} \sim m_H \sim M$). Near the alignment limit, *i.e.* for $|\cos(\beta-\alpha)|$ small, the modifications of the tree-level couplings of the h boson with respect to the SM predictions follow the expressions summarised in Table 7 [12].

Table 7: Multiplicative factors predicted in the four 2HDM scenarios near the alignment limit, as a function of $\tan\beta$ and $\cos(\beta-\alpha)$, for the Higgs boson couplings to up-type quarks (1st row), down-type quarks (2nd row), charged leptons (3rd row), vector bosons (4th row), and to itself (5th row). The symbol $c_{\beta-\alpha}$ stands for $\cos(\beta-\alpha)$, while $s_{\beta-\alpha}$ stands for $\sin(\beta-\alpha)$. The definition of the parameter $\bar{m}$ is given in the text.

Coupling	Type I	Type II	Lepton-specific	Flipped
u, c, t	$s_{\beta-\alpha} + c_{\beta-\alpha}/\tan\beta$			
d, s, b	$s_{\beta-\alpha} + c_{\beta-\alpha}/\tan\beta$	$s_{\beta-\alpha} - c_{\beta-\alpha} \times \tan\beta$	$s_{\beta-\alpha} + c_{\beta-\alpha}/\tan\beta$	$s_{\beta-\alpha} - c_{\beta-\alpha} \times \tan\beta$
e, μ, τ	$s_{\beta-\alpha} + c_{\beta-\alpha}/\tan\beta$	$s_{\beta-\alpha} - c_{\beta-\alpha} \times \tan\beta$	$s_{\beta-\alpha} - c_{\beta-\alpha} \times \tan\beta$	$s_{\beta-\alpha} + c_{\beta-\alpha}/\tan\beta$
W, Z	$s_{\beta-\alpha}$			
H	$s^3_{\beta-\alpha} + \left(3 - 2\frac{\bar{m}^2}{m_h^2}\right) c^2_{\beta-\alpha} s_{\beta-\alpha} + 2\cot(2\beta)\left(1 - \frac{\bar{m}^2}{m_h^2}\right) c^3_{\beta-\alpha}$			

In addition to the impact of the tree-level coupling modifications, the production and decay rates of the h boson are modified through next-to-leading-order electroweak corrections involving the trilinear hhh coupling λ [113]. In the 2HDM framework, this self-coupling is modified with respect to the SM expectation λ_{SM} by the scale factor (denoted as κ_λ) shown in the last row of Table 7 [114]. The parameter $\bar{m}$ is $\bar{m}^2 = \frac{m_{12}^2}{\sin\beta\cos\beta} = m_A^2 + \lambda_5 v^2$, where λ_5 is the coefficient of the $(\Phi_1^\dagger\Phi_2)^2$ term of the Higgs potential. Near the alignment limit considered, the value of $\bar{m}$ is close to that of m_A ($\lambda_5 v^2 \ll m_A^2$), and a value $\bar{m} = m_A = 1$ TeV ($\lambda_5 = 0$) is assumed in this section in all scenarios in which the effect of the self-coupling is considered in the calculation of limits on $\cos(\beta-\alpha)$ and $\tan\beta$.

In the following sections, limits on the 2HDM parameters $\cos(\beta-\alpha)$ and $\tan\beta$ are inferred from studies of the ensemble of Higgs boson production and decay rate measurements in two distinct scenarios: first by comparing the measured rates for each production mode with inclusive 2HDM predictions expressed in the so-called κ-framework, and then by comparing the more fine-grained measurements described in Section 2 with the 2HDM predictions expressed in the linearised statistical model of the EFT-based parametrisation described in Section 3.

4.1.1 Constraints based on the κ-framework

In the κ-framework [13], the Higgs boson production-mode cross-sections and decay branching ratios are parametrised in terms of multiplicative coupling strength modifiers κ [9]. In the model considered in this study, the loop-induced processes (gluon-gluon fusion $gg \to H$ and $gg \to ZH$ production, as well as $H \to \gamma\gamma$, $H \to Z\gamma$ and $H \to gg$ decays) are expressed in terms of the strength factors for the couplings to the SM particles inside the loop. The model also assumes that there are no invisible or undetected Higgs boson decays beyond the SM. The impact of the trilinear hhh coupling modifier κ_λ on the Higgs boson production and decay rates via NLO electroweak corrections to the LO amplitudes is also included in the parametrisations. In the likelihood function in Eq. (1) the signal strengths $\mu_k^{i,X}$ are reparametrised as $\mu_k^{i,X} = \mu^{i,X}(\{\boldsymbol{\kappa}(\tan\beta, \cos(\beta-\alpha))\})$, using the relations listed in Table 7. Confidence regions for $\tan\beta$ and $\cos(\beta-\alpha)$ can thus be inferred from the combined measurements of Higgs boson production and decay rates.

The resulting 95% CL contours in the $(\tan\beta, \cos(\beta-\alpha))$ plane are shown in Figure 19. All models exhibit similar exclusion regions in the $(\tan\beta, \cos(\beta-\alpha))$ plane at low values ($\lesssim 1$) of $\tan\beta$, where only a narrow region of $\cos(\beta-\alpha)$ around zero is consistent with the measured values of the Higgs boson production and

decay rates. The interval of allowed values of $\cos(\beta-\alpha)$ increases in size with $\tan\beta$, up to a total width of about 0.1–0.2 for $\tan\beta = 1$, depending on the model. For higher values of $\tan\beta$, in the models in which at least one of the coupling strength modifiers is enhanced by a factor $\tan\beta$, *i.e.* all models except type-I, the allowed range of $\cos(\beta-\alpha)$ around zero shrinks as $\tan\beta$ gets larger. For the type-I model, the allowed range of $\cos(\beta-\alpha)$ further increases with $\tan\beta$, reaching a width of around 0.5 for $\tan\beta = 10$. This starts to cover regions of the parameter space that deviate significantly from the alignment-limit hypothesis. When the constraint from the trilinear hhh coupling is included, the width of the 95% CL interval for $\cos(\beta-\alpha)$ at large $\tan\beta$ for the type-I model is reduced by about 50%. An additional feature of the type-I model result is that in the large $\tan\beta$ region, for positive $\cos(\beta-\alpha)$, the observed exclusion region is significantly larger than the expected one. This derives from the fact that the ATLAS measurement of Higgs boson production and decay rates favours values of the coupling strength modifiers to b, t quarks and τ leptons smaller than one and of the couplings to W, Z bosons larger than one ($\kappa_F = 0.95 \pm 0.05$ and $\kappa_V = 1.035 \pm 0.031$ when assuming that all fermions share the same modifier κ_F and that $\kappa_W = \kappa_Z = \kappa_V$ [9]). In this scenario the model predicts $\sin(\beta-\alpha) = \kappa_V \approx 1$ and $\cos(\beta-\alpha) = \tan\beta(\kappa_F - \sin(\beta-\alpha) \approx \tan\beta(\kappa_F - 1)$, disfavouring positive values of $\cos(\beta-\alpha)$ for $\kappa_F < 1$.

A second small region of allowed $\tan\beta$ and $\cos(\beta-\alpha)$ values for large $\tan\beta$ and $\cos(\beta-\alpha) \approx 0.2$ is present in type-II, lepton-specific, and flipped models. This corresponds to regions with $\cos(\beta+\alpha) \approx 0$, for which some of the fermion couplings have the same magnitude as in the SM but the opposite sign. In particular, this corresponds to a negative sign of the lepton couplings in the lepton-specific model, of the down-type quark couplings in the flipped model, or both in the type-II model. Since the sign of these couplings is not sufficiently constrained by the current experimental measurements, this region is not excluded. The same region is however not allowed in type-I models, in which down-type quarks and leptons coupling strength modifiers have the same sign (and value) as for up-type quarks. In that case, a negative sign of the top-quark coupling strength modifier κ_t is experimentally excluded by the measurement of $H \to \gamma\gamma$ decays, whose branching ratio depends linearly on $\kappa_t\kappa_W$ as a consequence of the interference between W-boson- and top-quark-mediated loop amplitudes.

4.1.2 Constraints using an EFT-based approach

The modifications to the tree-level Higgs boson couplings to fermions near the alignment limit described in Section 4.1 can be generated by the dimension-6 O_{bH}, O_{tH} and $O_{\tau H}$ operators of the SMEFT Lagrangian, with the following matching between the Wilson coefficients and the 2HDM parameters [115]:

$$\frac{v^2 c_{bH}}{\Lambda^2} = -Y_b \eta_b \frac{\cos(\beta-\alpha)}{\tan\beta}, \tag{16}$$

$$\frac{v^2 c_{tH}}{\Lambda^2} = -Y_t \frac{\cos(\beta-\alpha)}{\tan\beta}, \tag{17}$$

$$\frac{v^2 c_{\tau H}}{\Lambda^2} = -Y_\tau \eta_\tau \frac{\cos(\beta-\alpha)}{\tan\beta}. \tag{18}$$

In these formulae, computed to first order in $\cos(\beta-\alpha)$, $Y_i = \sqrt{2}m_i/v$ are the SM Higgs boson couplings and the values of η_i depend on the type of model ($\eta_b = -\tan^2\beta$ in type-II and flipped models, as is η_τ in type-II and lepton-specific models; $\eta_{b,\tau} = 1$ otherwise). The corrections to the HVV vertices are quadratic

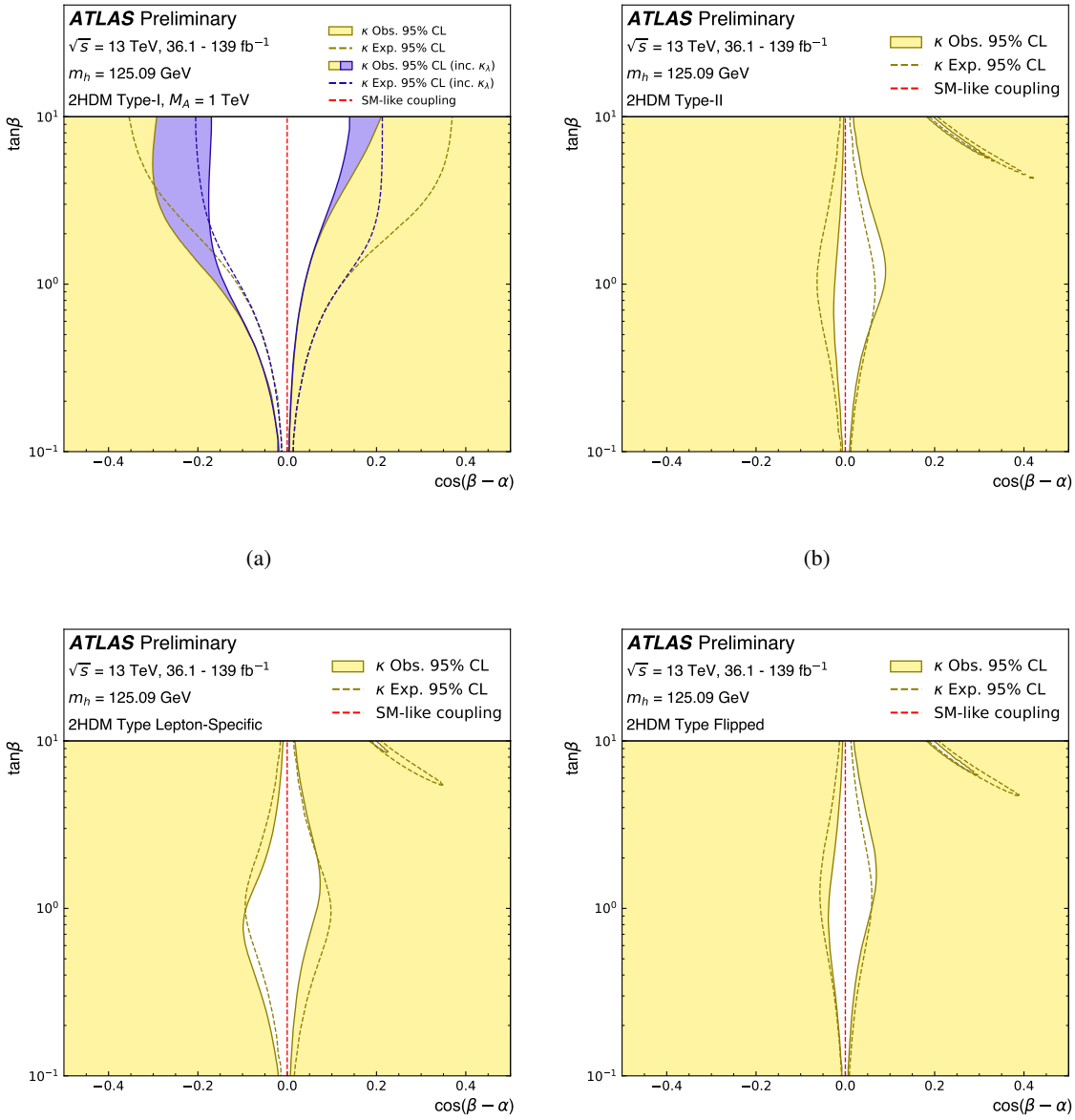

Figure 19: Regions of the 2HDM ($\tan\beta$, $\cos(\beta-\alpha)$) parameter plane excluded at 95% CL (light yellow filled regions) in the κ-framework-based approach by the measured rates of Higgs boson production and decays in (a) type I, (b) type II, (c) lepton-specific and (d) flipped models. The dark yellow dashed lines show the borders of the corresponding expected exclusion regions for the SM hypothesis. For type-I models, the observed and expected regions excluded at 95% CL when the κ_λ constraint is considered are also shown (solid and dashed blue lines). Results are derived assuming $|\cos(\beta-\alpha)| \ll 1$, near the alignment limit represented by the red dashed lines, and that the masses of the non-SM-like Higgs bosons are large compared with the SM vev.

in $\cos(\beta-\alpha)$ and are neglected. It should be noted that for the EFT to be valid, $\Lambda \gg v$ and therefore $|\cos(\beta-\alpha)| \propto \frac{v^2}{\Lambda^2}$ should be small, close to the alignment limit.

The operator $O_{\mathcal{H}}$ is also generated in the models under study, with a coefficient that scales with $\cos^2(\beta-\alpha)$ but which can be significantly enhanced if the other scalar states are much heavier than the SM-like Higgs boson. In that case, $O_{\mathcal{H}}$ is proportional to $(M/v)^2$ [115]:

$$\frac{v^2 c_H}{\Lambda^2} = \cos(\beta-\alpha)^2 \left(\frac{M}{v}\right)^2 .$$

Non-zero values of c_H modify the trilinear hhh coupling λ by a scale factor [116]:

$$\kappa_\lambda = 1 - \frac{v^2 c_H}{\lambda_{\text{SM}}\Lambda^2} = 1 - \frac{\cos(\beta-\alpha)^2}{\lambda_{\text{SM}}} \left(\frac{M}{v}\right)^2 .$$

In the following, a value of $M = 1$ TeV is assumed for the masses of the heavy scalar particles, and thus $\kappa_\lambda \approx 1 - (11\cos(\beta-\alpha))^2$ for $\Lambda = 1$ TeV. The constraint on κ_λ will affect the Type-I 2HDM interpretation, while exclusion limits for all other types will be unaffected.

Constraints on the values of $\tan\beta$ and $\cos(\beta-\alpha)$ can thus be inferred from those set on c_{bH}, c_{tH}, $c_{\tau H}$ and c_H by the SMEFT interpretation of the combined measurement of production and decay rates and STXS. The likelihood model defined in Section 3.2 is used, expressing the four Wilson coefficients c_{bH}, c_{tH}, $c_{\tau H}$ and c_H in terms of the 2HDM parameters as in Eqs. (16)–(18) and fixing all the other Wilson coefficients to zero. The results are shown in Figure 20.

A comparison between the excluded regions from the two approaches is shown in Figure 21. In the regions where the assumptions used in this study are valid, the excluded regions are very similar in the two approaches. In the type-I model for large values of $\tan\beta$, the EFT-based approach, which does not exploit constraints from the HVV couplings, which only enter at dimension-8 in the SMEFT expansion and are not considered here, and retains only terms of $O(\cos(\beta-\alpha))$ in the expansion of κ_λ, leads to looser constraints on $\cos(\beta-\alpha)$ than the κ-framework-based approach, in which $\kappa_V = \sin(\beta-\alpha)$ and the full dependence of κ_λ on $\cos(\beta-\alpha)$ is considered. However, part of the allowed region of parameter space in this case is inconsistent with the alignment limit hypothesis of $|\cos(\beta-\alpha)| \ll 1$.

A significant difference between the $\tan\beta$, $\cos(\beta-\alpha)$ constraints from the approach presented in this section and those obtained using the κ-framework-based approach is the absence here of the second small allowed region around $\tan\beta \approx 10$, $\cos(\beta-\alpha) \approx 0.2$. This difference follows from the fact that in the EFT-based approach only dimension-6 terms are considered in the SMEFT Lagrangian and a linear expansion of $\sigma \times B$, which does not include terms of second order in the Wilson coefficients, is performed. The likelihood function in the EFT-based approach is thus Gaussian and has a single maximum. [117] As a consequence, the region with flipped coupling sign does not appear.

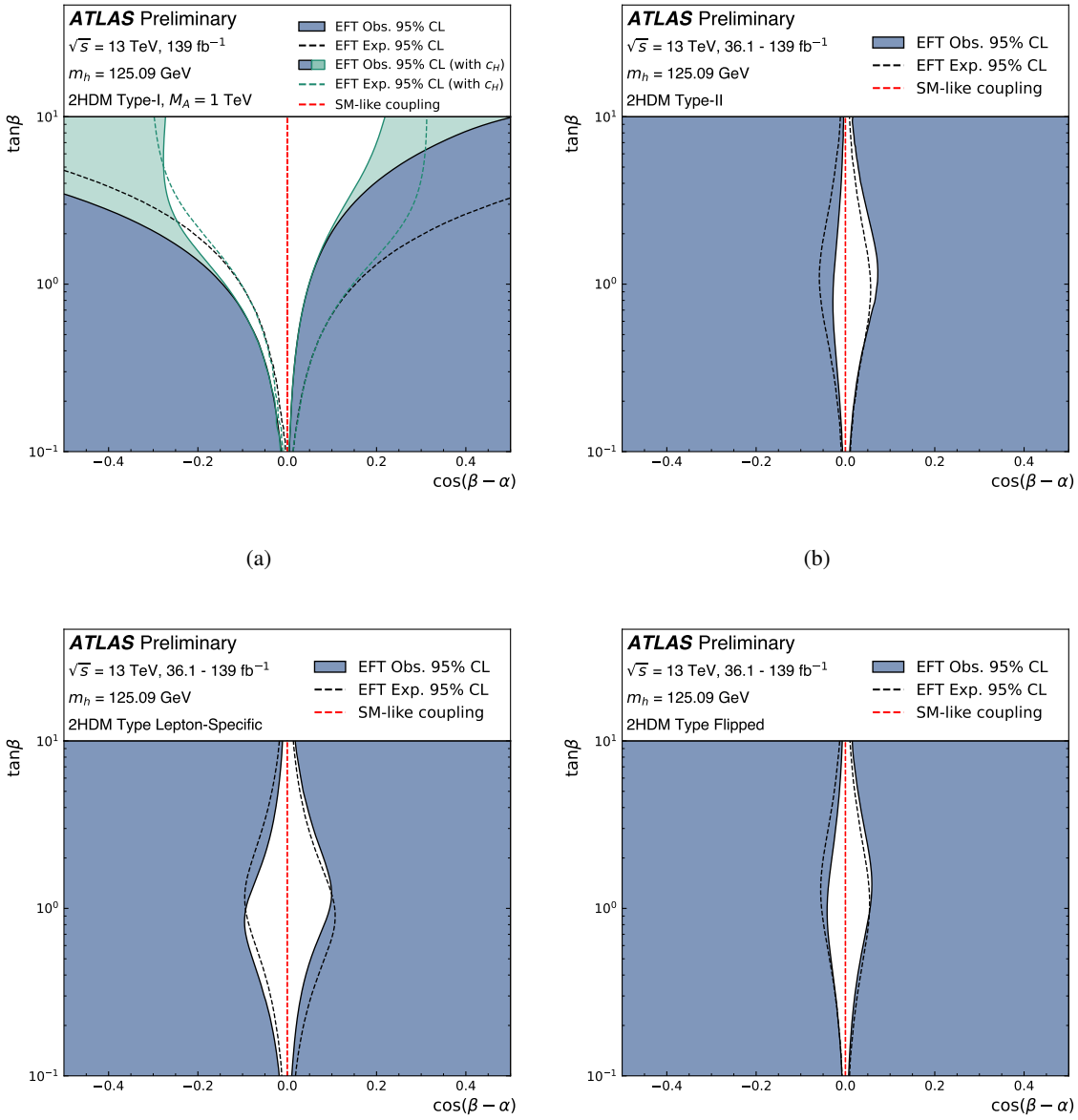

Figure 20: Regions of the 2HDM ($\tan\beta$, $\cos(\beta-\alpha)$) parameter plane excluded at 95% CL (blue filled regions) in the EFT-based approach by the measured rates of Higgs boson production and decays in (a) type-I, (b) type-II, (c) lepton-specific and (d) flipped models. The dashed black lines show the borders of the corresponding expected exclusion regions for the SM hypothesis. For type-I models, the observed and expected regions excluded at 95% CL when the c_H constraint is considered are also shown (solid and dashed green lines). Results are derived assuming $|\cos(\beta-\alpha)| \ll 1$, near the alignment limit represented by the red dashed lines, and that the masses of the non-SM-like Higgs bosons are large compared with the SM vev.

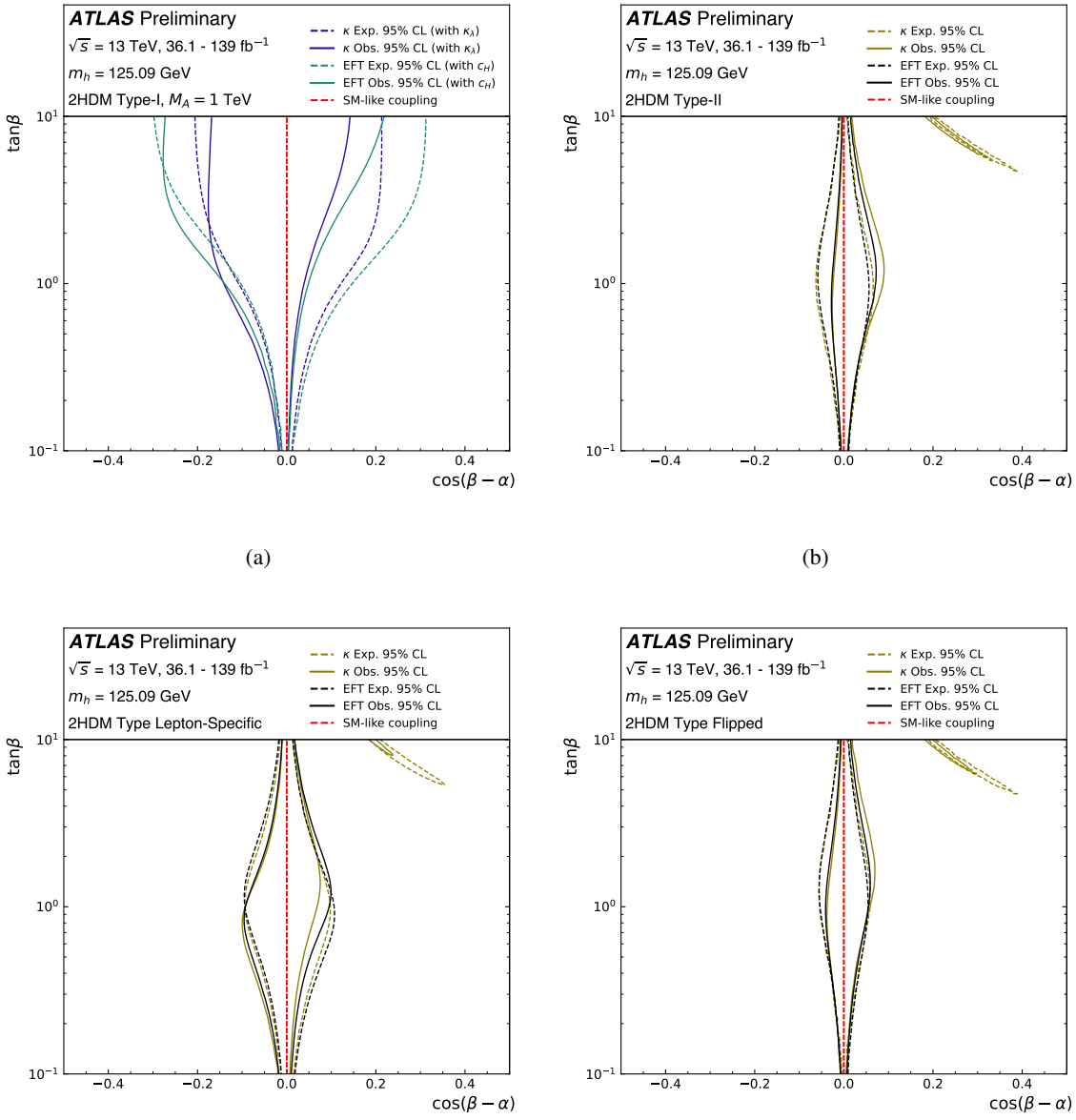

Figure 21: Comparison of the constraints from the approaches based on the κ- and EFT-frameworks in the ($\tan\beta$, $\cos(\beta-\alpha)$) plane in 2HDM for (a) type-I, (b) type-II, (c) lepton-specific and (d) flipped models. The κ_λ constraint is included in the type-I model intepretation. Solid (dashed) lines indicate the observed (expected) constraints. Results are derived assuming $|\cos(\beta-\alpha)| \ll 1$, near the alignment limit represented by the red dashed lines, and that the masses of the non-SM-like Higgs bosons are large compared with the SM vev.

4.2 Constraints on the MSSM

Supersymmetry (SUSY) [118–126], a theoretically motivated framework for extending the Standard Model, was conceived to address some of the Standard Model's unanswered questions. In particular, SUSY offers a solution to the hierarchy problem [127–130], which is related to the fine tuning needed to obtain the correct mass for the observed Higgs boson. Supersymmetry can also provide credible dark matter candidates [131, 132] and can improve the unification of the electroweak and strong interactions [133–141].

The minimal supersymmetric extension of the Standard Model is the so-called MSSM [14–18]. The Higgs sector of the MSSM is a 2HDM with type-II Yukawa couplings. At tree level, all Higgs boson masses and couplings can be expressed in terms of two parameters, usually chosen to be $\tan\beta$ and the mass of the pseudoscalar Higgs boson, m_A. Radiative corrections, including contributions from amplitudes mediated by loops of SM particles and their superpartners, lead to modifications of the tree-level relations and can raise the lightest CP-even Higgs boson mass m_h, bounded at tree-level by $m_h \leq m_Z|\cos 2\beta|$, to the level of the mass of the Higgs boson discovered by the ATLAS and CMS collaborations. The MSSM predicts a supersymmetric partner for each SM state. In addition to the supersymmetric spin-one partners of the SM fermions (sfermions) and spin-half partners of the gluons (gluinos), there are a total of eight spin-half partners of the electroweak gauge and Higgs bosons: the neutral bino (superpartner of the $U(1)$ gauge field); the winos, which are a charged pair and a neutral particle (superpartners of the W bosons of the $SU(2)_L$ gauge fields), and the higgsinos, which are two neutral particles and a charged pair (superpartners of the Higgs fields). Mixing between the bino, the neutral wino and the neutral higgsinos leads to four neutralinos, while charginos arise from mixing between the charged winos and the charged higgsinos.

The MSSM has over a hundred parameters that describe the pattern of sparticle masses and their decays, and the values of the quantum corrections that they induce vary significantly as a function of these parameters. The parameter space is thus too large to be probed exhaustively through a relatively small set of Higgs boson production and decay rate measurements. Therefore, several *benchmark scenarios* have been proposed in which the values of the MSSM parameters other than $\tan\beta$ and m_A are fixed to alternative sets of values that lead to significantly different phenomenologies of the MSSM Higgs sector. With only two free parameters left, $\tan\beta$ and m_A, an MSSM interpretation of the Higgs boson production and decay rate measurements is simplified.

4.2.1 MSSM benchmark scenarios

In this study, the measured production and decay rates of the observed Higgs boson with mass close to 125 GeV are compared to the predictions of seven MSSM benchmark scenarios, under the assumption that the observed boson is the light CP-even Higgs boson h of the MSSM. In each benchmark scenario, constraints are set on m_A and $\tan\beta$ after fixing the values of all the other MSSM parameters. The seven benchmark scenarios that are considered are the following [38, 39]:

- $\boldsymbol{M_h^{125}}$ **scenario:** All superparticles are assumed to be so heavy that they affect the production and decay rates of the MSSM Higgs bosons very mildly. The loop-induced contributions to the couplings of the light CP-even scalar are small. The largest ones, enhanced with $\tan\beta$, affect the bottom-quark Yukawa coupling but cancel out in the decoupling limit $m_A \gg m_Z$.
- $\boldsymbol{M_h^{125}(\tilde{\tau})}$ **scenario:** The parameters related to the stop, sbottom and gluino masses are the same as in the previous case, but the soft-SUSY-breaking masses and trilinear interaction term for the staus are significantly smaller. The resulting light staus and light wino-like charginos can alter the amplitude

for the decay of the SM-like Higgs boson to photons, with contributions that scale as $1/\tan\beta$ or $\tan^2\beta$, respectively. As in the previous scenario, at low m_A the hbb coupling is enhanced, leading to a suppression of the branching ratios for all the other decay channels of the SM-like Higgs boson.

- $\boldsymbol{M_h^{125}(\tilde{\chi})}$ **scenario:** The SUSY parameters in this scenario leads to all charginos and neutralinos being relatively light, with significant higgsino-gaugino mixing, and to a compressed electroweakino mass spectrum. The $\tan\beta$-enhanced corrections to the hbb coupling are suppressed. At low values of $\tan\beta$, the partial width for the SM-like Higgs boson decay to two photons is significantly increased. The corresponding branching ratio for low $\tan\beta$ is larger (smaller) than the SM prediction for large (small) values of m_A.

- $\boldsymbol{M_h^{125}}$**(alignment) scenario:** In the "alignment without decoupling" scenario, for a given value of $\tan\beta$, one of the two neutral CP-even scalars has SM-like couplings independently of the mass spectrum of the remaining Higgs bosons. In particular, for $\tan\beta \approx 7$ the lighter scalar Higgs boson h is SM-like, for relatively low values of m_A.

- $\boldsymbol{M_{h_1}^{125}}$**(CPV) scenario:** This scenario is characterised by CP violation in the Higgs sector, where mixing between the neutral CP-even scalar states h and H and the CP-odd scalar state A is induced by a non-zero phase ϕ_{A_t} in the soft-SUSY-breaking Higgs-stop interaction term. This causes significant interference effects in the production and decay of the two heavier neutral states, which leads to weaker constraints from the searches of resonances decaying to $\tau^+\tau^-$. The relevant parameters are chosen such that the strongest interference region is located near the exclusion contour of the corresponding scenario with real parameters, the mass of the SM-like scalar is near the observed value, and all electric dipole moments are within the allowed ranges.

- $\boldsymbol{M_{h,\mathrm{EFT}}^{125}}$ **scenario:** In the previous scenarios, the sfermions have masses close to the TeV scale. As a consequence, values of $\tan\beta < 5$ are automatically excluded as they would lead to values of the Higgs boson mass m_h that are significantly lower than the experimental value of 125 GeV. To circumvent this problem, in this scenario all supersymmetric particles, including sfermions, are relatively heavy, with a mass close to the SUSY scale m_{SUSY}, which is adjusted dynamically from 6 TeV to 10^{13} TeV to yield a Higgs boson mass of 125 GeV for values of $\tan\beta$ between one and ten. As all supersymmetric particles are so heavy that production and decays of the MSSM Higgs bosons are only mildly affected by their presence, their contribution to the Higgs boson properties is calculated with an effective field theory. As in most of the previous scenarios, for low values of m_A the hbb coupling is enhanced with respect to the SM prediction and reduces to the SM value for large m_A. At very small $\tan\beta$, the model predicts a small suppression of the htt coupling, leading in turn to a slight suppression of the ggF production cross-section.

- $\boldsymbol{M_{h,\mathrm{EFT}}^{125}(\tilde{\chi})}$ **scenario:** Similarly to the previous scenario, the SUSY scale is adjusted dynamically to yield a light Higgs boson mass of $m_h \approx 125$ GeV at each point of the SUSY parameter space. In contrast to the $M_{h,\mathrm{EFT}}^{125}$ scenario, however, this scenario features relatively light neutralinos and charginos. As a consequence, loop-induced amplitudes mediated by these light states can induce modifications of the light Higgs boson properties such as an enhancement of its partial decay width to two photons, in particular for low $\tan\beta$. The model therefore predicts a branching ratio for $h \to \gamma\gamma$ significantly larger than the SM prediction for large m_A and low $\tan\beta$. At low values of m_A, the enhancement of the hbb coupling leads instead to an increase of the $h \to b\bar{b}$ branching ratio and a decrease of the $h \to \gamma\gamma$ branching ratio with respect to their SM expectations.

In addition, an eighth simplified scenario, called hMSSM [37], is considered. In this scenario, the light Higgs boson h is assumed to be the particle discovered by the ATLAS and CMS collaborations in 2012. Its

mass m_h is assumed to be equal to the experimental value of 125.09 GeV, and it is used to fix the value of the dominant radiative corrections to the CP-even Higgs mass matrix from the stop-top sector. This hypothesis determines all other parameters of the Higgs sector, including α, m_H, $m_{H^\pm}$, and the couplings between the Higgs bosons and the other particles, in terms of only the two parameters m_A and $\tan\beta$. Due to its assumptions, the hMSSM is a good approximation of the MSSM only for moderate values of $\tan\beta$, $1 \lesssim \tan\beta \lesssim 10$ [36].

4.2.2 Interpretation procedure

Since Higgs boson production cross-sections in the MSSM are not calculated for the full STXS Stage-1.2 phase space partitioning of production cross-sections, only inclusive production-mode cross-sections are used in this analysis. The signal strength modifiers $\mu^{i,X}$ in the signal yield expression of Eq. (2) are then written as:

$$\mu^{i,X}(m_A, \tan\beta) = \frac{\sigma^i_{\text{(h)MSSM}}(m_A, \tan\beta)}{\sigma^i_{\text{SM}}} \cdot \frac{B^X_{\text{(h)MSSM}}(m_A, \tan\beta)}{B^X_{\text{SM}}} \equiv r^i(m_A, \tan\beta) \cdot r^X(m_A, \tan\beta), \quad (19)$$

where the index i enumerates the production processes (ggF, $b\bar{b}H$, $t\bar{t}H$, VBF, $qq/qg{\to}ZH$, $gg{\to}ZH$, $qq{\to}WH$).

The values of the production cross-section scale factors r^i and branching ratio scale factors r^X are obtained from the calculations detailed in Refs. [142, 143]. For all scenarios except the hMSSM, Higgs boson masses and mixing (and effective Yukawa couplings) are calculated with `FeynHiggs` [144–150]. In the hMSSM branching ratios are solely computed with HDECAY [151, 152], while all other scenarios combine the most precise estimates of FeynHiggs, HDECAY [151, 152] and PROPHECY4F [153, 154]. Inclusive cross-sections for ggF production are obtained with SusHi [155, 156], which includes NLO QCD corrections [157], NNLO QCD corrections for the top-quark contribution in the effective theory of a heavy top quark [158–162] and electroweak corrections involving light quarks [163, 164]. For the SM-like Higgs boson, SusHi adds N3LO corrections in the effective theory of a heavy top quark in a threshold expansion [58, 165, 166]. Cross-sections for bottom-quark-initiated Higgs boson production rely on matched predictions [167–170], which are based on the five flavour NNLO QCD calculation [80] and the four flavour NLO QCD calculation [78, 79]. The values of the cross-sections of rare production modes, such as $gg \to Zh$, $pp \to thW$ and $pp \to thq$, which are not calculated in Refs. [142, 143], are determined through their relations, within the κ-framework, to κ_t, κ_b, κ_W, κ_Z, that are determined as either $\kappa_t^2 = \sigma^{t\bar{t}h}_{\text{MSSM}}/\sigma^{t\bar{t}H}_{\text{SM}}$ or $\kappa_x^2 = \Gamma^{h\to xx}_{\text{MSSM}}/\Gamma^{h\to xx}_{\text{SM}}$, where $x = b, W, Z$:

$$\begin{aligned} r^{gg\to Zh} &= 2.456\kappa_Z^2 + 0.456\kappa_t^2 - 1.903\kappa_Z\kappa_t - 0.011\kappa_Z\kappa_b + 0.003\kappa_t\kappa_b, \\ r^{thW} &= 2.909\kappa_t^2 + 2.310\kappa_W^2 - 4.220\kappa_t\kappa_W, \\ r^{thq} &= 2.633\kappa_t^2 + 3.578\kappa_W^2 - 5.211\kappa_t\kappa_W. \end{aligned}$$

As the cross-section and branching ratio scale factors r^i and r^X are only calculated for a discrete set of points in the two-dimensional benchmark parameter space, a likelihood based on Eq. (19) is not differentially expressed in terms of its theory parameters $(m_A, \tan\beta)$. Instead, the values of the profile likelihood ratio are calculated at fixed points in the $(m_A, \tan\beta)$ plane, profiling only the nuisance parameters, and then numerically interpolated. Regions of the benchmark scenario parameter space for which the mass m_h of the light CP-even Higgs boson h predicted by the MSSM differs from the experimental value of 125.09 GeV

by more than 3 GeV, which is the estimated bound of allowed values of the calculated Higgs boson mass in `FeynHiggs` [146, 171], are considered as excluded.

4.2.3 Results

Figure 22 shows the observed and expected 95% CL exclusion limits of the MSSM in the two-dimensional plane (m_A, $\tan\beta$) for the M_h^{125}, $M_h^{125}(\tilde{\chi})$, $M_h^{125}(\tilde{\tau})$, and M_h^{125}(alignment) benchmark scenarios. For all four scenarios, the regions excluded by the Higgs mass requirement ($|m_h - 125.09\ \text{GeV}| < 3\ \text{GeV}$) are separately indicated with gray shaded areas. For completeness, the constraints from previous searches for $H/A \to \tau\tau$ [172] and $H^+ \to t\bar{b}$ [173] are also overlaid.

In the M_h^{125} and $M_h^{125}(\tilde{\chi})$ scenarios, the low m_A region, in which an enhancement of the $h \to b\bar{b}$ branching ratio and a suppression of the branching ratios of the other decay modes such as $h \to \gamma\gamma$ are predicted, is disfavoured. Since the data marginally prefer $B(h \to b\bar{b})/B_{\text{SM}}(h \to b\bar{b}) < 1$ and $B(h \to \gamma\gamma)/B_{\text{SM}}(h \to \gamma\gamma) > 1$, the observed constraints are tighter than those expected under the SM hypothesis. In the $M_h^{125}(\tilde{\tau})$ scenario, the region at low m_A and $\tan\beta < 53$ is excluded for the same reason. The region $\tan\beta > 53$, in which the $\tilde{\tau}$ loop reduces the hbb coupling, leading to an enhanced prediction of $B(h \to \gamma\gamma)$, is also largely excluded. In the M_h^{125}(alignment) scenario, the limit of alignment without decoupling is only realised for $\tan\beta \approx 7$ and $m_A \sim 200$ GeV. For larger values of m_A, MSSM couplings are more similar to SM couplings, causing the allowed $\tan\beta$ region to broaden.

In all four benchmark scenarios, the MSSM analysis generally excludes the low m_A regime for most of the scanned $\tan\beta$ range, while the requirement $|m_h - 125.09\ \text{GeV}| < 3\ \text{GeV}$ excludes the low $\tan\beta$ range for all scanned values of m_A, a range not covered by the direct searches for $H/A \to \tau\tau$ and $H^+ \to t\bar{b}$ decays.

Figure 23 shows the observed and expected 95% CL exclusion limits on the MSSM in the two-dimensional plane of $m_{H^\pm}$ vs $\tan\beta$ for the $M_{h_1}^{125}$(CPV) scenario and of m_A vs $\tan\beta$ for the $M_{h,\text{EFT}}^{125}$, $M_{h,\text{EFT}}^{125}(\tilde{\chi})$ and hMSSM scenarios.

The condition $|m_h - 125.09\ \text{GeV}| < 3\ \text{GeV}$ excludes values of $\tan\beta \lesssim 6$ for all values of $m_{H^\pm}$ in the $M_{h_1}^{125}$(CPV) scenario, while no part of the parameter space is excluded in the $M_{h,\text{EFT}}^{125}$ and $M_{h,\text{EFT}}^{125}(\tilde{\chi})$ benchmark scenarios, in which $m_h = 125.09$ GeV can be achieved irrespectively of the values of $\tan\beta$ and m_A through the flexible m_{SUSY} scale.

In these four models, the low m_A region, where an enhancement of the hbb coupling is predicted, is excluded, and the excluded region is larger than expected in the SM hypothesis for the same reason as for the previous four models.

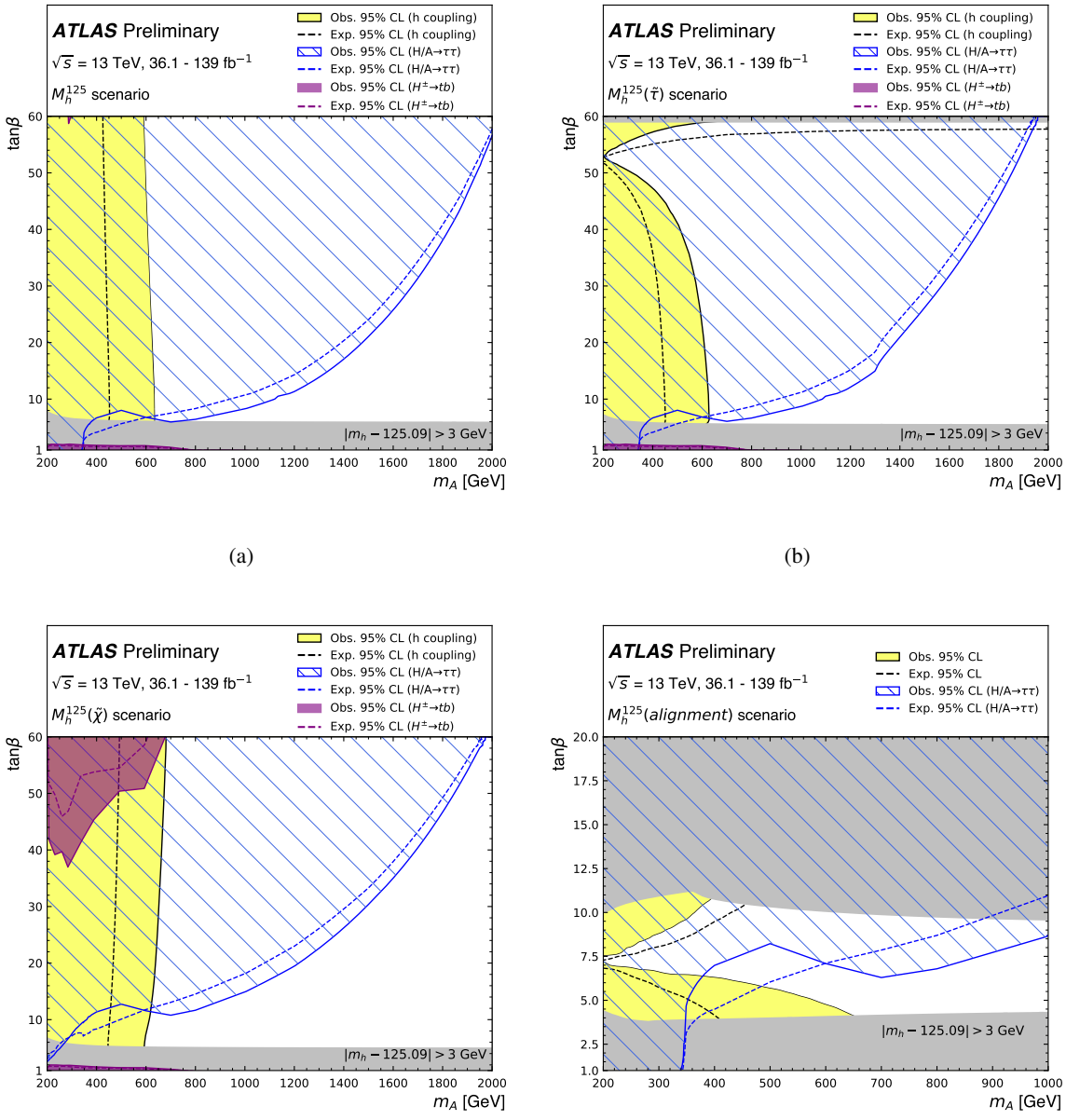

Figure 22: Observed (solid yellow area) and expected (dashed line) exclusion contours at 95% CL in the $(m_A, \tan\beta)$ plane for the (a) M_h^{125}, (b) $M_h^{125}(\tilde{\tau})$, (c) $M_h^{125}(\tilde{\chi})$ and (d) M_h^{125}(alignment) scenarios. The parameter space excluded by the condition $|m_h - 125.09\ \text{GeV}| < 3$ GeV is marked in gray. For comparison, the parameter space excluded by the searches for $H/A \to \tau\tau$ [172] and for $H^+ \to t\bar{b}$ [173] are overlaid in blue and purple, respectively. For the M_h^{125}(alignment) scenario, no constraints from the search for $H^+ \to t\bar{b}$ are available.

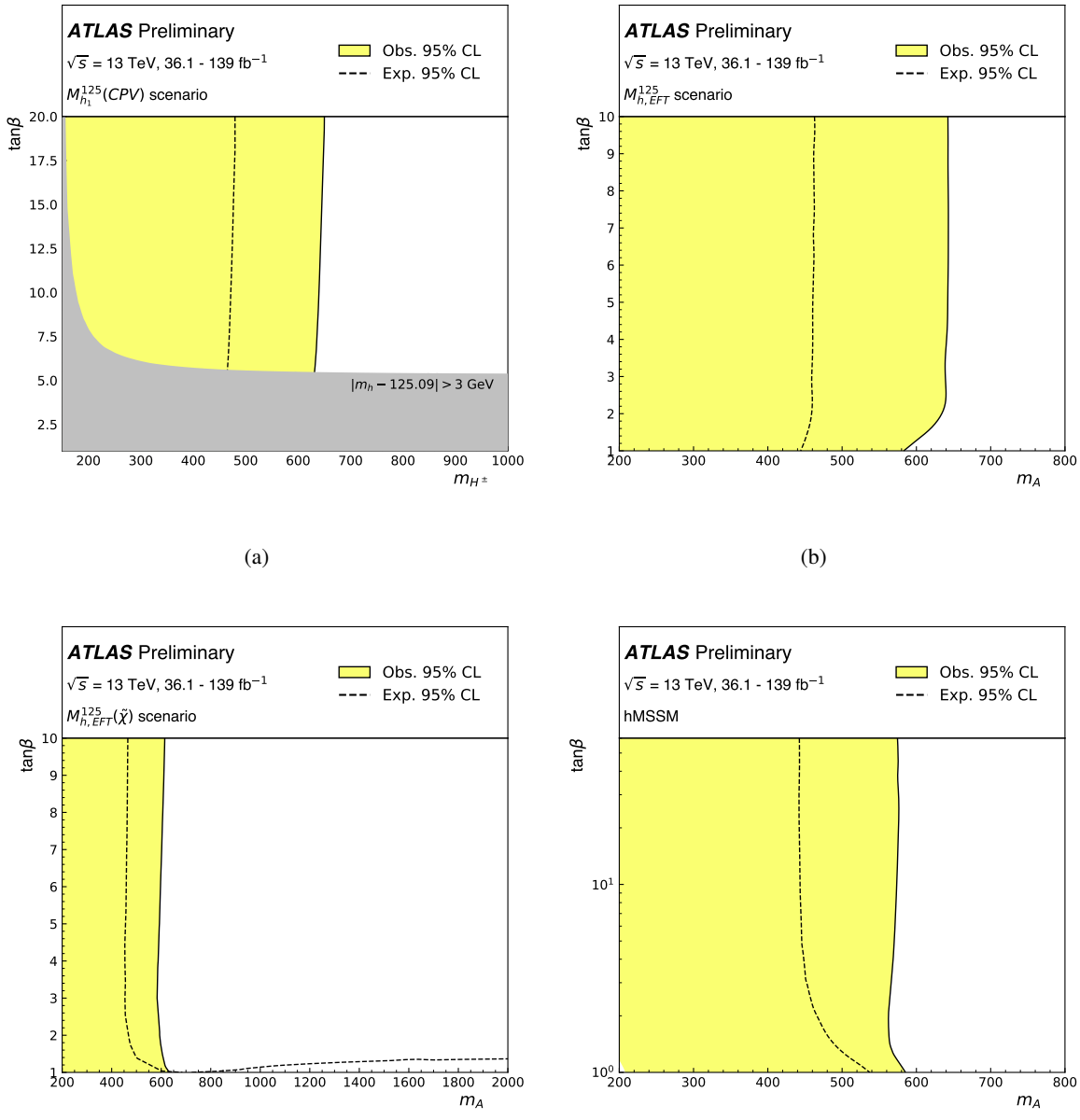

Figure 23: Observed (solid yellow area) and expected (dashed line) exclusion contours at 95% CL in (a) the $(m_{H^\pm}, \tan\beta)$ plane for the $M_{h_1}^{125}$(CPV) scenario and in the $(m_A, \tan\beta)$ plane for the (b) $M_{h,\mathrm{EFT}}^{125}$, (c) $M_{h,\mathrm{EFT}}^{125}(\tilde{\chi})$ and (d) hMSSM scenarios. In (a), the parameter space excluded by the condition $|m_h - 125.09\ \mathrm{GeV}| < 3$ GeV is marked in gray.

5 Conclusions

Novel interpretations of the recent combined ATLAS measurements of Higgs boson production and decay rates and simplified template cross-sections in several final states have been performed. Constraints on linear combinations of Wilson coefficients corresponding to SM Effective Field Theory operators in the Warsaw basis are reported. In this model-independent parametrization of BSM physics effects, no significant deviations from the SM have been observed. A comparison of results interpreted with a linearised SMEFT model that only considers terms suppressed by up to a factor Λ^{-2}, and a linear+quadratic variant that considers all available terms including those with suppression factor Λ^{-4}, shows that the effect of operators suppressed by Λ^{-4} can significantly affect constraints on Wilson coefficients for a mass scale of $\Lambda = 1$ TeV.

Constraints on a subset of these operators have also been set through a joint interpretation of the fiducial cross-section measurements of Higgs boson production as a function of transverse momentum in the $H \to \gamma\gamma$ and $H \to ZZ^* \to 4\ell$ final states. Three linear combinations of the Wilson coefficients of operators affecting these spectra can be simultaneously constrained. For two of these combinations the constraints are similar to those that can be derived from the interpretation of Higgs boson simplified template cross-section measurements in the same channels. The constraint on the top-gluon coupling is significantly stronger in the interpretation of simplified template cross-sections.

Finally, the Higgs boson production and decay rate measurements have been interpreted in the context of two-Higgs-doublet models and of eight benchmark scenarios of the minimal supersymmetrical model. Constraints have been set on the $(\cos(\beta-\alpha), \tan\beta)$ plane in 2HDM type-I, type-II, lepton-specific and flipped models, and on the parameters $(m_A, \tan\beta)$ of the MSSM in the eight benchmark scenarios. These results are complementary to limits from direct searches for additional Higgs bosons.

References

[1] F. Englert and R. Brout, *Broken Symmetry and the Mass of Gauge Vector Mesons*, Phys. Rev. Lett. **13** (9 1964) 321 (cit. on p. 3).

[2] P. W. Higgs, *Broken symmetries, massless particles and gauge fields*, Phys. Lett. **12** (1964) 132 (cit. on p. 3).

[3] P. W. Higgs, *Broken Symmetries and the Masses of Gauge Bosons*, Phys. Rev. Lett. **13** (16 1964) 508 (cit. on p. 3).

[4] G. S. Guralnik, C. R. Hagen and T. W. .B. Kibble, *Global Conservation Laws and Massless Particles*, Phys. Rev. Lett. **13** (1964) 585 (cit. on p. 3).

[5] P. W. Higgs, *Spontaneous Symmetry Breakdown without Massless Bosons*, Phys. Rev. **145** (1966) 1156 (cit. on p. 3).

[6] T. W. B. Kibble, *Symmetry Breaking in Non-Abelian Gauge Theories*, Phys. Rev. **155** (1967) 1554 (cit. on p. 3).

[7] ATLAS Collaboration, *Observation of a new particle in the search for the Standard Model Higgs boson with the ATLAS detector at the LHC*, Phys. Lett. B **716** (2012) 1, arXiv: 1207.7214 [hep-ex] (cit. on p. 3).

[8] CMS Collaboration,
Observation of a new boson at a mass of 125 GeV with the CMS experiment at the LHC,
Phys. Lett. B **716** (2012) 30, arXiv: 1207.7235 [hep-ex] (cit. on p. 3).

[9] ATLAS Collaboration,
A detailed map of Higgs boson interactions by the ATLAS experiment ten years after the discovery,
Nature **607** (2022) 52, arXiv: 2207.00092 [hep-ex] (cit. on pp. 3, 4, 9, 25, 42, 43).

[10] T. D. Lee, *A Theory of Spontaneous T Violation*, Phys. Rev. D **8** (1973) 1226 (cit. on pp. 3, 41).

[11] J. F. Gunion and H. E. Haber,
The CP conserving two Higgs doublet model: The approach to the decoupling limit,
Phys. Rev. D **67** (2003) 075019, arXiv: hep-ph/0207010 [hep-ph] (cit. on pp. 3, 41).

[12] G. Branco et al., *Theory and phenomenology of two-Higgs-doublet models*,
Phys. Rept. **516** (2012) 1, arXiv: 1106.0034 [hep-ph] (cit. on pp. 3, 41).

[13] LHC Higgs Cross Section Working Group, S. Heinemeyer, C. Mariotti, G. Passarino and R. Tanaka (Eds.), *Handbook of LHC Higgs Cross Sections: 3. Higgs Properties*,
CERN-2013-004 (2013), arXiv: 1307.1347 [hep-ph] (cit. on pp. 3, 42).

[14] P. Fayet, *Supersymmetry and weak, electromagnetic and strong interactions*,
Phys. Lett. B **64** (1976) 159 (cit. on pp. 3, 48).

[15] P. Fayet,
Spontaneously broken supersymmetric theories of weak, electromagnetic and strong interactions,
Phys. Lett. B **69** (1977) 489 (cit. on pp. 3, 48).

[16] G. R. Farrar and P. Fayet, *Phenomenology of the production, decay, and detection of new hadronic states associated with supersymmetry*, Phys. Lett. B **76** (1978) 575 (cit. on pp. 3, 48).

[17] P. Fayet, *Relations between the masses of the superpartners of leptons and quarks, the goldstino coupling and the neutral currents*, Phys. Lett. B **84** (1979) 416 (cit. on pp. 3, 48).

[18] S. Dimopoulos and H. Georgi, *Softly broken supersymmetry and SU(5)*,
Nucl. Phys. B **193** (1981) 150 (cit. on pp. 3, 48).

[19] ATLAS Collaboration, *Measurements of the Higgs boson inclusive and differential fiducial cross sections in the* 4ℓ *decay channel at* $\sqrt{s} = 13$ *TeV*, Eur. Phys. J. C **80** (2020) 942,
arXiv: 2004.03969 [hep-ex] (cit. on pp. 3, 5, 8).

[20] ATLAS Collaboration,
Measurements of the Higgs boson inclusive and differential fiducial cross-sections in the diphoton decay channel with pp *collisions at* $\sqrt{s} = 13$ *TeV with the ATLAS detector*, JHEP **08** (2022) 027,
arXiv: 2202.00487 [hep-ex] (cit. on pp. 3, 5, 8).

[21] ATLAS Collaboration,
Measurements of differential cross sections of Higgs boson production through gluon fusion in the $H \to WW^* \to e\nu\mu\nu$ *final state at* $\sqrt{s} = 13$ *TeV with the ATLAS detector*, (2023),
arXiv: 2301.06822 [hep-ex] (cit. on p. 3).

[22] ATLAS Collaboration,
Fiducial and differential cross-section measurements for the vector-boson-fusion production of the Higgs boson in the $H \to WW^*$ $e\nu\mu\nu$ *decay channel at* 13 *TeV with the ATLAS detector*, (2023),
arXiv: 2304.03053 [hep-ex] (cit. on p. 3).

[23] ATLAS Collaboration, *Higgs boson production cross-section measurements and their EFT interpretation in the 4ℓ decay channel at $\sqrt{s}$ = 13 TeV with the ATLAS detector*, Eur. Phys. J. C **80** (2020) 957, arXiv: 2004.03447 [hep-ex] (cit. on pp. 3, 5, 8, 9), Erratum: Eur. Phys. J. C **81** (2021) 29.

[24] ATLAS Collaboration, *Measurement of the properties of Higgs boson production at $\sqrt{s}$ = 13 TeV in the $H \to \gamma\gamma$ channel using 139 fb^{-1} of pp collision data with the ATLAS experiment*, CERN-EP-2022-094 (2022), arXiv: 2207.00348 [hep-ex] (cit. on pp. 3, 5, 8, 9).

[25] ATLAS Collaboration, *Measurements of WH and ZH production in the $H \to b\bar{b}$ decay channel in pp collisions at 13 TeV with the ATLAS detector*, Eur. Phys. J. C **81** (2021) 178, arXiv: 2007.02873 [hep-ex] (cit. on pp. 3, 5, 9).

[26] ATLAS Collaboration, *Measurement of the associated production of a Higgs boson decaying into b-quarks with a vector boson at high transverse momentum in pp collisions at $\sqrt{s}$ = 13 TeV with the ATLAS detector*, Phys. Lett. B **816** (2021) 136204, arXiv: 2008.02508 [hep-ex] (cit. on pp. 3, 5, 9).

[27] ATLAS Collaboration, *Measurements of Higgs bosons decaying to bottom quarks from vector boson fusion production with the ATLAS experiment at $\sqrt{s}$ = 13 TeV*, Eur. Phys. J. C **81** (2020) 537, arXiv: 2011.08280 [hep-ex] (cit. on pp. 3, 5, 9).

[28] ATLAS Collaboration, *Constraints on Higgs boson production with large transverse momentum using $H \to b\bar{b}$ decays in the ATLAS detector*, Phys. Rev. D **105** (2021) 092003, arXiv: 2111.08340 [hep-ex] (cit. on pp. 3, 5, 9).

[29] ATLAS Collaboration, *Measurement of Higgs boson decay into b-quarks in associated production with a top-quark pair in pp collisions at $\sqrt{s}$ = 13 TeV with the ATLAS detector*, JHEP **06** (2021) 097, arXiv: 2111.06712 [hep-ex] (cit. on pp. 3, 5, 9).

[30] ATLAS Collaboration, *Measurements of Higgs boson production cross-sections in the $H \to \tau^+\tau^-$ decay channel in pp collisions at $\sqrt{s}$ = 13 TeV with the ATLAS detector*, JHEP **08** (2022) 175, arXiv: 2201.08269 [hep-ex] (cit. on pp. 3, 5, 9).

[31] ATLAS Collaboration, *Measurements of Higgs boson production by gluon–gluon fusion and vector-boson fusion using $H \to WW^* \to e\nu\mu\nu$ decays in pp collisions at $\sqrt{s}$ = 13 TeV with the ATLAS detector*, CERN-EP-2022-078 (2022), arXiv: 2207.00338 [hep-ex] (cit. on pp. 3, 5, 9).

[32] ATLAS Collaboration, *A search for the $Z\gamma$ decay mode of the Higgs boson in pp collisions at $\sqrt{s}$ = 13 TeV with the ATLAS detector*, Phys. Lett. B **809** (2020) 135754, arXiv: 2005.05382 [hep-ex] (cit. on pp. 3, 5).

[33] ATLAS Collaboration, *A search for the dimuon decay of the Standard Model Higgs boson with the ATLAS detector*, Phys. Lett. B **812** (2021) 135980, arXiv: 2007.07830 [hep-ex] (cit. on pp. 3, 5).

[34] ATLAS Collaboration, *Measurements of gluon-gluon fusion and vector-boson fusion Higgs boson production cross-sections in the $H \to WW^* \to e\nu\mu\nu$ decay channel in pp collisions at $\sqrt{s}$ = 13 TeV with the ATLAS detector*, Phys. Lett. B **789** (2019) 508, arXiv: 1808.09054 [hep-ex] (cit. on p. 4).

[35] ATLAS Collaboration, *Evidence for the associated production of the Higgs boson and a top quark pair with the ATLAS detector*, Phys. Rev. D **97** (2018) 072003, arXiv: 1712.08891 [hep-ex] (cit. on pp. 4, 5).

[36] ATLAS Collaboration, *Combined measurements of Higgs boson production and decay using up to 80 fb^{-1} of proton–proton collision data at $\sqrt{s}$ = 13 TeV collected with the ATLAS experiment*, Phys. Rev. D **101** (2020) 012002, arXiv: 1909.02845 [hep-ex] (cit. on pp. 4, 50).

[37] A. Djouadi et al., *The post-Higgs MSSM scenario: habemus MSSM?*, Eur. Phys. J. C **73** (2013) 2650, arXiv: 1307.5205 [hep-ph] (cit. on pp. 4, 49).

[38] E. Bagnaschi et al., *MSSM Higgs boson searches at the LHC: benchmark scenarios for Run 2 and beyond*, Eur. Phys. J. C **79** (2019) 617, arXiv: 1808.07542 [hep-ph] (cit. on pp. 4, 48).

[39] H. Bahl, S. Liebler and T. Stefaniak, *MSSM Higgs benchmark scenarios for Run 2 and beyond: the low* $\tan\beta$ *region*, Eur. Phys. J. C **79** (2019) 279, arXiv: 1901.05933 [hep-ph] (cit. on pp. 4, 48).

[40] ATLAS and CMS Collaborations, *Combined Measurement of the Higgs Boson Mass in pp Collisions at $\sqrt{s}$ = 7 and 8 TeV with the ATLAS and CMS Experiments*, Phys. Rev. Lett. **114** (2015) 191803, arXiv: 1503.07589 [hep-ex] (cit. on p. 4).

[41] ATLAS Collaboration, *The ATLAS Experiment at the CERN Large Hadron Collider*, JINST **3** (2008) S08003 (cit. on p. 4).

[42] ATLAS Collaboration, *ATLAS Insertable B-Layer: Technical Design Report*, ATLAS-TDR-19; CERN-LHCC-2010-013, 2010, URL: https://cds.cern.ch/record/1291633 (cit. on p. 4), Addendum: ATLAS-TDR-19-ADD-1; CERN-LHCC-2012-009, 2012, URL: https://cds.cern.ch/record/1451888.

[43] B. Abbott et al., *Production and integration of the ATLAS Insertable B-Layer*, JINST **13** (2018) T05008, arXiv: 1803.00844 [physics.ins-det] (cit. on p. 4).

[44] ATLAS Collaboration, *Luminosity determination in pp collisions at $\sqrt{s}$ = 8 TeV using the ATLAS detector at the LHC*, Eur. Phys. J. C **76** (2016) 653, arXiv: 1608.03953 [hep-ex] (cit. on p. 4).

[45] G. Avoni et al., *The new LUCID-2 detector for luminosity measurement and monitoring in ATLAS*, JINST **13** (2018) P07017 (cit. on p. 4).

[46] ATLAS Collaboration, *Measurement of the production cross section for a Higgs boson in association with a vector boson in the $H \to WW^* \to \ell\nu\ell\nu$ channel in pp collisions at $\sqrt{s}$ = 13 TeV with the ATLAS detector*, Phys. Lett. B **798** (2019) 134949, arXiv: 1903.10052 [hep-ex] (cit. on p. 5).

[47] LHC Higgs Cross Section Working Group, D. de Florian and others (Eds.), *Handbook of LHC Higgs Cross Sections: 4. Deciphering the Nature of the Higgs Sector*, CERN-2017-002-M (2016), arXiv: 1610.07922 [hep-ph] (cit. on pp. 5, 6, 8, 9, 17).

[48] P. Nason, *A new method for combining NLO QCD with shower Monte Carlo algorithms*, JHEP **11** (2004) 040, arXiv: hep-ph/0409146 (cit. on p. 5).

[49] S. Frixione, P. Nason and C. Oleari, *Matching NLO QCD computations with parton shower simulations: the POWHEG method*, JHEP **11** (2007) 070, arXiv: 0709.2092 [hep-ph] (cit. on p. 5).

[50] S. Alioli, P. Nason, C. Oleari and E. Re, *A general framework for implementing NLO calculations in shower Monte Carlo programs: the POWHEG BOX*, JHEP **06** (2010) 043, arXiv: 1002.2581 [hep-ph] (cit. on p. 5).

[51] S. Alioli, P. Nason, C. Oleari and E. Re,
NLO Higgs boson production via gluon fusion matched with shower in POWHEG,
JHEP **04** (2009) 002, arXiv: 0812.0578 [hep-ph] (cit. on p. 5).

[52] K. Hamilton, P. Nason, E. Re and G. Zanderighi, *NNLOPS simulation of Higgs boson production*,
JHEP **10** (2013) 222, arXiv: 1309.0017 [hep-ph] (cit. on p. 5).

[53] K. Hamilton, P. Nason and G. Zanderighi,
Finite quark-mass effects in the NNLOPS POWHEG+MiNLO Higgs generator,
JHEP **05** (2015) 140, arXiv: 1501.04637 [hep-ph] (cit. on p. 5).

[54] S. Catani and M. Grazzini, *Next-to-Next-to-Leading-Order Subtraction Formalism in Hadron Collisions and its Application to Higgs-boson Production at the Large Hadron Collider*,
Phys. Rev. Lett. **98** (2007) 222002, arXiv: hep-ph/0703012 [hep-ph] (cit. on p. 5).

[55] K. Hamilton, P. Nason, C. Oleari and G. Zanderighi, *Merging H/W/Z + 0 and 1 jet at NLO with no merging scale: a path to parton shower + NNLO matching*, JHEP **05** (2013) 082,
arXiv: 1212.4504 [hep-ph] (cit. on p. 5).

[56] J. Butterworth et al., *PDF4LHC recommendations for LHC Run II*, J. Phys. G **43** (2016) 023001,
arXiv: 1510.03865 [hep-ph] (cit. on p. 5).

[57] C. Anastasiou, C. Duhr, F. Dulat, F. Herzog and B. Mistlberger,
Higgs Boson Gluon-Fusion Production in QCD at Three Loops,
Phys. Rev. Lett. **114** (2015) 212001, arXiv: 1503.06056 [hep-ph] (cit. on p. 6).

[58] C. Anastasiou et al.,
High precision determination of the gluon fusion Higgs boson cross-section at the LHC,
JHEP **05** (2016) 058, arXiv: 1602.00695 [hep-ph] (cit. on pp. 6, 50).

[59] S. Actis, G. Passarino, C. Sturm and S. Uccirati,
NLO electroweak corrections to Higgs boson production at hadron colliders,
Phys. Lett. B **670** (2008) 12, arXiv: 0809.1301 [hep-ph] (cit. on p. 6).

[60] C. Anastasiou, R. Boughezal and F. Petriello,
Mixed QCD-electroweak corrections to Higgs boson production in gluon fusion,
JHEP **04** (2009) 003, arXiv: 0811.3458 [hep-ph] (cit. on p. 6).

[61] M. Grazzini and H. Sargsyan, *Heavy-quark mass effects in Higgs boson production at the LHC*,
JHEP **09** (2013) 129, arXiv: 1306.4581 [hep-ph] (cit. on p. 6).

[62] P. Nason and C. Oleari,
NLO Higgs boson production via vector-boson fusion matched with shower in POWHEG,
JHEP **02** (2010) 037, arXiv: 0911.5299 [hep-ph] (cit. on p. 6).

[63] K. Hamilton, P. Nason and G. Zanderighi, *MINLO: multi-scale improved NLO*,
JHEP **10** (2012) 155, arXiv: 1206.3572 [hep-ph] (cit. on p. 6).

[64] M. Ciccolini, A. Denner and S. Dittmaier, *Strong and Electroweak Corrections to the Production of a Higgs Boson + 2 Jets via Weak Interactions at the Large Hadron Collider*,
Phys. Rev. Lett. **99** (2007) 161803, arXiv: 0707.0381 [hep-ph] (cit. on p. 6).

[65] M. Ciccolini, A. Denner and S. Dittmaier,
Electroweak and QCD corrections to Higgs production via vector-boson fusion at the CERN LHC,
Phys. Rev. D **77** (2008) 013002, arXiv: 0710.4749 [hep-ph] (cit. on p. 6).

[66] P. Bolzoni, F. Maltoni, S.-O. Moch and M. Zaro,
Higgs Boson Production via Vector-Boson Fusion at Next-to-Next-to-Leading Order in QCD,
Phys. Rev. Lett. **105** (2010) 011801, arXiv: 1003.4451 [hep-ph] (cit. on p. 6).

[67] O. Brein, A. Djouadi and R. Harlander,
NNLO QCD corrections to the Higgs-strahlung processes at hadron colliders,
Phys. Lett. B **579** (2004) 149, arXiv: hep-ph/0307206 (cit. on p. 6).

[68] A. Denner, S. Dittmaier, S. Kallweit and A. Mück, *Electroweak corrections to Higgs-strahlung off W/Z bosons at the Tevatron and the LHC with HAWK*, JHEP **03** (2012) 075,
arXiv: 1112.5142 [hep-ph] (cit. on p. 6).

[69] L. Altenkamp, S. Dittmaier, R. V. Harlander, H. Rzehak and T. J. E. Zirke,
Gluon-induced Higgs-strahlung at next-to-leading order QCD, JHEP **02** (2013) 078,
arXiv: 1211.5015 [hep-ph] (cit. on p. 6).

[70] J. Alwall et al., *The automated computation of tree-level and next-to-leading order differential cross sections, and their matching to parton shower simulations*, JHEP **07** (2014) 079,
arXiv: 1405.0301 [hep-ph] (cit. on pp. 6, 13).

[71] The NNPDF Collaboration, R. D. Ball et al., *Parton distributions for the LHC run II*,
JHEP **04** (2015) 040, arXiv: 1410.8849 [hep-ph] (cit. on p. 6).

[72] W. Beenakker et al., *NLO QCD corrections to $t\bar{t}H$ production in hadron collisions*,
Nucl. Phys. B **653** (2003) 151, arXiv: hep-ph/0211352 [hep-ph] (cit. on p. 6).

[73] S. Dawson, C. Jackson, L. Orr, L. Reina and D. Wackeroth,
Associated Higgs production with top quarks at the large hadron collider: NLO QCD corrections,
Phys. Rev. D **68** (2003) 034022, arXiv: hep-ph/0305087 [hep-ph] (cit. on p. 6).

[74] Y. Zhang, W.-G. Ma, R.-Y. Zhang, C. Chen and L. Guo,
QCD NLO and EW NLO corrections to $t\bar{t}H$ production with top quark decays at hadron collider,
Phys. Lett. B **738** (2014) 1, arXiv: 1407.1110 [hep-ph] (cit. on p. 6).

[75] S. Frixione, V. Hirschi, D. Pagani, H. S. Shao and M. Zaro,
Weak corrections to Higgs hadroproduction in association with a top-quark pair,
JHEP **09** (2014) 065, arXiv: 1407.0823 [hep-ph] (cit. on p. 6).

[76] M. Wiesemann et al., *Higgs production in association with bottom quarks*, JHEP **02** (2015) 132,
arXiv: 1409.5301 [hep-ph] (cit. on p. 6).

[77] NNPDF Collaboration, R. D. Ball et al., *Parton distributions with LHC data*,
Nucl. Phys. B **867** (2013) 244, arXiv: 1207.1303 [hep-ph] (cit. on p. 6).

[78] S. Dawson, C. Jackson, L. Reina and D. Wackeroth,
Exclusive Higgs boson production with bottom quarks at hadron colliders,
Phys. Rev. D **69** (7 2004) 074027, arXiv: hep-ph/0311067 [hep-ph] (cit. on pp. 6, 50).

[79] S. Dittmaier, M. Krämer and M. Spira,
Higgs radiation off bottom quarks at the Tevatron and the CERN LHC,
Phys. Rev. D **70** (7 2004) 074010, arXiv: hep-ph/0309204 [hep-ph] (cit. on pp. 6, 50).

[80] R. V. Harlander and W. B. Kilgore,
Higgs boson production in bottom quark fusion at next-to-next-to leading order,
Phys. Rev. D **68** (1 2003) 013001, arXiv: hep-ph/0304035 [hep-ph] (cit. on pp. 6, 50).

[81] H.-L. Lai et al., *New parton distributions for collider physics*, Phys. Rev. D **82** (2010) 074024, arXiv: 1007.2241 [hep-ph] (cit. on p. 6).

[82] F. Demartin, F. Maltoni, K. Mawatari and M. Zaro, *Higgs production in association with a single top quark at the LHC*, Eur. Phys. J. C **75** (2015) 267, arXiv: 1504.00611 [hep-ph] (cit. on p. 6).

[83] T. Sjöstrand, S. Mrenna and P. Skands, *A brief introduction to PYTHIA 8.1*, Comput. Phys. Commun. **178** (2008) 852, arXiv: 0710.3820 [hep-ph] (cit. on p. 6).

[84] ATLAS Collaboration, *Measurement of the Z/γ^* boson transverse momentum distribution in pp collisions at $\sqrt{s} = 7$ TeV with the ATLAS detector*, JHEP **09** (2014) 145, arXiv: 1406.3660 [hep-ex] (cit. on p. 6).

[85] ATLAS Collaboration, *ATLAS Pythia 8 tunes to 7 TeV data*, ATL-PHYS-PUB-2014-021, 2014, URL: https://cds.cern.ch/record/1966419 (cit. on p. 6).

[86] S. Agostinelli et al., *GEANT4 – a simulation toolkit*, Nucl. Instrum. Meth. A **506** (2003) 250 (cit. on p. 6).

[87] ATLAS Collaboration, *The ATLAS Simulation Infrastructure*, Eur. Phys. J. C **70** (2010) 823, arXiv: 1005.4568 [physics.ins-det] (cit. on p. 6).

[88] A. D. Martin, W. J. Stirling, R. S. Thorne and G. Watt, *Parton distributions for the LHC*, Eur. Phys. J. C **63** (2009) 189, arXiv: 0901.0002 [hep-ph] (cit. on p. 6).

[89] ATLAS Collaboration, *Summary of ATLAS Pythia 8 tunes*, ATL-PHYS-PUB-2012-003, 2012, URL: https://cds.cern.ch/record/1474107 (cit. on p. 6).

[90] ATLAS Collaboration, *The Pythia 8 A3 tune description of ATLAS minimum bias and inelastic measurements incorporating the Donnachie–Landshoff diffractive model*, ATL-PHYS-PUB-2016-017, 2016, URL: https://cds.cern.ch/record/2206965 (cit. on p. 6).

[91] J. R. Andersen et al., *Les Houches 2015: Physics at TeV Colliders Standard Model Working Group Report*, (2016), arXiv: 1605.04692 [hep-ph] (cit. on p. 8).

[92] N. Berger et al., *Simplified Template Cross Sections - Stage 1.1*, (2019), arXiv: 1906.02754 [hep-ph] (cit. on p. 8).

[93] S. Amoroso et al., 'Les Houches 2019: Physics at TeV Colliders: Standard Model Working Group Report', *11th Les Houches Workshop on Physics at TeV Colliders: PhysTeV Les Houches*, 2020, arXiv: 2003.01700 [hep-ph] (cit. on p. 8).

[94] ATLAS Collaboration, *Evaluation of theoretical uncertainties for simplified template cross section measurements of V-associated production of the Higgs boson*, ATL-PHYS-PUB-2018-035, 2018, URL: https://cds.cern.ch/record/2649241 (cit. on p. 8).

[95] I. Brivio and M. Trott, *The standard model as an effective field theory*, Phys. Rept. **793** (2019) 1, arXiv: 1706.08945 [hep-ph] (cit. on p. 13).

[96] ATLAS Collaboration, *Methodology for EFT interpretation of Higgs boson simplified template cross-section results in ATLAS*, ATL-PHYS-PUB-2019-042, 2019, URL: https://cds.cern.ch/record/2694284 (cit. on p. 13).

[97] B. Grzadkowski, M. Iskrzynski, M. Misiak and J. Rosiek,
Dimension-six terms in the Standard Model Lagrangian, JHEP **10** (2010) 085,
arXiv: 1008.4884 [hep-ph] (cit. on p. 13).

[98] D. Barducci et al.,
Interpreting top-quark LHC measurements in the standard-model effective field theory,
CERN-LPCC-2018-01 (2018), arXiv: 1802.07237 [hep-ph] (cit. on pp. 13, 15).

[99] I. Brivio, Y. Jiang and M. Trott, *The SMEFTsim package, theory and tools*, JHEP **12** (2017) 070,
arXiv: 1709.06492 [hep-ph] (cit. on pp. 14, 15).

[100] C. Degrande et al., *Standard Model Effective Theory at Next-to-Leading-Order in QCD*,
URL: http://feynrules.irmp.ucl.ac.be/wiki/SMEFTatNLO (cit. on p. 15).

[101] S. Dawson and P. P. Giardino,
Electroweak corrections to Higgs boson decays to $\gamma\gamma$ and W^+W^- in standard model EFT,
Phys. Rev. D **98** (2018) 095005, arXiv: 1807.11504 [hep-ph] (cit. on p. 15).

[102] S. Dawson and P. P. Giardino,
Higgs decays to ZZ and $Z\gamma$ in the standard model effective field theory: An NLO analysis,
Phys. Rev. D **97** (2018) 093003, arXiv: 1801.01136 [hep-ph] (cit. on p. 15).

[103] M. L. Mangano, M. Moretti, F. Piccinini and M. Treccani,
Matching matrix elements and shower evolution for top-quark production in hadronic collisions,
JHEP **01** (2007) 013, arXiv: hep-ph/0611129 (cit. on p. 15).

[104] S. Mrenna and P. Richardson,
Matching matrix elements and parton showers with HERWIG and PYTHIA, JHEP **05** (2004) 040,
arXiv: hep-ph/0312274 (cit. on p. 15).

[105] A. Buckley et al., *Rivet user manual*, Comput. Phys. Commun. **184** (2013) 2803,
arXiv: 1003.0694 [hep-ph] (cit. on p. 15).

[106] LHC Higgs WG,
URL: https://gitlab.cern.ch/LHCHIGGSXS/LHCHXSWG2/STXS/Classification
(cit. on p. 15).

[107] T. Corbett, A. Martin and M. Trott,
Consistent higher order σ ($\mathcal{GG} \to h$), Γ ($h \to \mathcal{GG}$) and $\Gamma(h \to \gamma\gamma)$ in geoSMEFT,
JHEP **12** (2021) 147, arXiv: 2107.07470 [hep-ph] (cit. on p. 15).

[108] T. Corbett and A. Martin,
Higgs associated production with a vector decaying to two fermions in the geoSMEFT, (2023),
arXiv: 2306.00053 [hep-ph] (cit. on p. 15).

[109] A. Martin and M. Trott,
More accurate $\sigma(\mathcal{G}\,\mathcal{G} \to h)$, $\Gamma(h \to \mathcal{G}\,\mathcal{G}, \mathcal{A}\mathcal{A}, \bar{\Psi}\Psi)$ and Higgs width results via the geoSMEFT,
(2023), arXiv: 2305.05879 [hep-ph] (cit. on p. 15).

[110] C. Degrande, B. Fuks, K. Mawatari, K. Mimasu and V. Sanz, *Electroweak Higgs boson production in the standard model effective field theory beyond leading order in QCD*,
Eur. Phys. J. **C77** (2017) 262, arXiv: 1609.04833 [hep-ph] (cit. on p. 16).

[111] S. L. Glashow and S. Weinberg, *Natural conservation laws for neutral currents*,
Phys. Rev. D **15** (1977) 1958 (cit. on p. 41).

[112] E. A. Paschos, *Diagonal neutral currents*, Phys. Rev. D **15** (1977) 1966 (cit. on p. 41).

[113] F. Monti et al., *Modelling of the single-Higgs simplified template cross-sections (STXS 1.2) for the determination of the Higgs boson trilinear self-coupling*, tech. rep., 2022, URL: https://cds.cern.ch/record/2803606 (cit. on p. 42).

[114] F. Arco, S. Heinemeyer and M. J. Herrero, *Exploring sizable triple Higgs couplings in the 2HDM*, Eur. Phys. J. C **80** (2020) 884, arXiv: 2005.10576 [hep-ph] (cit. on p. 42).

[115] S. Dawson, S. Homiller and S. D. Lane, *Putting standard model EFT fits to work*, Phys. Rev. D **102** (2020) 055012, arXiv: 2007.01296 [hep-ph] (cit. on pp. 43, 45).

[116] S. Dawson, D. Fontes, S. Homiller and M. Sullivan, *Role of dimension-eight operators in an EFT for the 2HDM*, Phys. Rev. D **106** (2022) 055012, arXiv: 2205.01561 [hep-ph] (cit. on p. 45).

[117] H. Bélusca-Maïto, A. Falkowski, D. Fontes, J. C. Romão and J. P. Silva, *Higgs EFT for 2HDM and beyond*, Eur. Phys. J. C **77** (2017) 176, arXiv: 1611.01112 [hep-ph] (cit. on p. 45).

[118] H. Miyazawa, *Baryon Number Changing Currents*, Prog. Theor. Phys. **36 (6)** (1966) 1266 (cit. on p. 48).

[119] P. Ramond, *Dual Theory for Free Fermions*, Phys. Rev. D **3** (1971) 2415 (cit. on p. 48).

[120] Y. A. Gol'fand and E. P. Likhtman, *Extension of the algebra of Poincare group generators and violation of P invariance*, JETP Lett. **13** (1971) 323, reprinted in Supergravities in Diverse Dimensions (1989) 20, URL: http://jetpletters.ru/ps/717/article_11110.shtml (cit. on p. 48).

[121] A. Neveu and J. H. Schwarz, *Factorizable dual model of pions*, Nucl. Phys. B **31** (1971) 86 (cit. on p. 48).

[122] A. Neveu and J. H. Schwarz, *Quark Model of Dual Pions*, Phys. Rev. D **4** (1971) 1109 (cit. on p. 48).

[123] J. Gervais and B. Sakita, *Field theory interpretation of supergauges in dual models*, Nucl. Phys. B **34** (1971) 632 (cit. on p. 48).

[124] D. V. Volkov and V. P. Akulov, *Is the neutrino a goldstone particle?*, Phys. Lett. B **46** (1973) 109 (cit. on p. 48).

[125] J. Wess and B. Zumino, *A lagrangian model invariant under supergauge transformations*, Phys. Lett. B **49** (1974) 52 (cit. on p. 48).

[126] J. Wess and B. Zumino, *Supergauge transformations in four-dimensions*, Nucl. Phys. B **70** (1974) 39 (cit. on p. 48).

[127] S. Weinberg, *Implications of dynamical symmetry breaking*, Phys. Rev. D **13** (1976) 974 (cit. on p. 48).

[128] E. Gildener, *Gauge-symmetry hierarchies*, Phys. Rev. D **14** (1976) 1667 (cit. on p. 48).

[129] S. Weinberg, *Implications of dynamical symmetry breaking: An addendum*, Phys. Rev. D **19** (1979) 1277 (cit. on p. 48).

[130] L. Susskind, *Dynamics of spontaneous symmetry breaking in the Weinberg-Salam theory*, Phys. Rev. D **20** (1979) 2619 (cit. on p. 48).

[131] H. Goldberg, *Constraint on the Photino Mass from Cosmology*, Phys. Rev. Lett. **50** (1983) 1419 (cit. on p. 48).

[132] J. Ellis, J. Hagelin, D. Nanopoulos, K. Olive and M. Srednicki, *Supersymmetric relics from the big bang*, Nucl. Phys. B **238** (1984) 453 (cit. on p. 48).

[133] S. Dimopoulos, S. Raby and F. Wilczek, *Supersymmetry and the scale of unification*, Phys. Rev. D **24** (1981) 1681 (cit. on p. 48).

[134] N. Sakai, *Naturalnes in supersymmetric GUTS*, Z. Phys. C **11** (1981) 153 (cit. on p. 48).

[135] L. Ibáñez and G. Ross, *Low-energy predictions in supersymmetric grand unified theories*, Phys. Lett. B **105** (1981) 439 (cit. on p. 48).

[136] M. Einhorn and D. Jones, *The weak mixing angle and unification mass in supersymmetric SU(5)*, Nucl. Phys. B **196** (1982) 475 (cit. on p. 48).

[137] W. J. Marciano and G. Senjanović, *Predictions of supersymmetric grand unified theories*, Phys. Rev. D **25** (1982) 3092 (cit. on p. 48).

[138] C. Giunti, C. W. Kim and U. W. Lee, *Running coupling constants and grand unification models*, Mod. Phys. Lett. A **06** (1991) 1745 (cit. on p. 48).

[139] J. Ellis, S. Kelley and D. Nanopoulos, *Probing the desert using gauge coupling unification*, Phys. Lett. B **260** (1991) 131 (cit. on p. 48).

[140] U. Amaldi, W. de Boer and H. Fürstenau, *Comparison of grand unified theories with electroweak and strong coupling constants measured at LEP*, Phys. Lett. B **260** (1991) 447 (cit. on p. 48).

[141] P. Langacker and M. Luo, *Implications of precision electroweak experiments for m_t, ρ_0, $sin^2\theta W$, and grand unification*, Phys. Rev. D **44** (1991) 817 (cit. on p. 48).

[142] LHC Higgs WG, *MSSM Neutral Higgs LHCXSWG3 Twiki page*, URL: https://twiki.cern.ch/twiki/bin/view/LHCPhysics/LHCHXSWGMSSMNeutral (cit. on p. 50).

[143] E. A. Bagnaschi, S. Heinemeyer, S. Liebler, P. Slavich and M. Spira, *Benchmark Scenarios for MSSM Higgs Boson Searches at the LHC*, LHCHWG-2021-001, 2021, URL: https://cds.cern.ch/record/2791954 (cit. on p. 50).

[144] S. Heinemeyer, W. Hollik and G. Weiglein, *FeynHiggs: a program for the calculation of the masses of the neutral CP even Higgs bosons in the MSSM*, Comput. Phys. Commun. **124** (2000) 76, arXiv: hep-ph/9812320 [hep-ph] (cit. on p. 50).

[145] S. Heinemeyer, W. Hollik and G. Weiglein, *The masses of the neutral CP-even Higgs bosons in the MSSM: Accurate analysis at the two loop level*, Eur. Phys. J. C **9** (1999) 343, arXiv: hep-ph/9812472 [hep-ph] (cit. on p. 50).

[146] G. Degrassi, S. Heinemeyer, W. Hollik, P. Slavich and G. Weiglein, *Towards high precision predictions for the MSSM Higgs sector*, Eur. Phys. J. C **28** (2003) 133, arXiv: hep-ph/0212020 [hep-ph] (cit. on pp. 50, 51).

[147] M. Frank et al., *The Higgs boson masses and mixings of the complex MSSM in the Feynman-diagrammatic approach*, Journal of High Energy Physics **2007** (2007) 047 (cit. on p. 50).

[148] T. Hahn, S. Heinemeyer, W. Hollik, H. Rzehak and G. Weiglein, *High-Precision Predictions for the Light CP-Even Higgs Boson Mass of the Minimal Supersymmetric Standard Model*, Phys. Rev. Lett. **112** (2014) (cit. on p. 50).

[149] H. Bahl and W. Hollik, *Precise prediction for the light MSSM Higgs boson mass combining effective field theory and fixed-order calculations*, Eur. Phys. J. C **76** (2016) 499, arXiv: 1608.01880 [hep-ph] (cit. on p. 50).

[150] H. Bahl, S. Heinemeyer, W. Hollik and G. Weiglein, *Reconciling EFT and hybrid calculations of the light MSSM Higgs-boson mass*, Eur. Phys. J. C **78** (2018) 57, arXiv: 1706.00346 [hep-ph] (cit. on p. 50).

[151] A. Djouadi, J. Kalinowski and M. Spira, *HDECAY: A program for Higgs boson decays in the Standard Model and its supersymmetric extension*, Comput. Phys. Commun. **108** (1998) 56, arXiv: hep-ph/9704448 (cit. on p. 50).

[152] A. Djouadi, J. Kalinowski, M. Muehlleitner and M. Spira, *HDECAY: Twenty++ years after*, Comput. Phys. Commun. **238** (2019) 214, arXiv: 1801.09506 [hep-ph] (cit. on p. 50).

[153] A. Bredenstein, A. Denner, S. Dittmaier and M. M. Weber, *Precise predictions for the Higgs-boson decay $H \to WW/ZZ \to 4$ leptons*, Phys. Rev. D **74** (2006) 013004, arXiv: hep-ph/0604011 [hep-ph] (cit. on p. 50).

[154] A. Bredenstein, A. Denner, S. Dittmaier and M. M. Weber, *Radiative corrections to the semileptonic and hadronic Higgs-boson decays $H \to WW/ZZ \to 4$ fermions*, JHEP **02** (2007) 080, arXiv: hep-ph/0611234 (cit. on p. 50).

[155] R. V. Harlander, S. Liebler and H. Mantler, *SusHi: A program for the calculation of Higgs production in gluon fusion and bottom-quark annihilation in the Standard Model and the MSSM*, Comput. Phys. Commun. **184** (2013) 1605, arXiv: 1212.3249 [hep-ph] (cit. on p. 50).

[156] R. V. Harlander, S. Liebler and H. Mantler, *SusHi Bento: Beyond NNLO and the heavy-top limit*, Comput. Phys. Commun. **212** (2017) 239, arXiv: 1605.03190 [hep-ph] (cit. on p. 50).

[157] M. Spira, A. Djouadi, D. Graudenz and P. Zerwas, *Higgs boson production at the LHC*, Nucl. Phys. B **453** (1995) 17, arXiv: hep-ph/9504378 (cit. on p. 50).

[158] R. V. Harlander and W. B. Kilgore, *Next-to-Next-to-Leading Order Higgs Production at Hadron Colliders*, Phys. Rev. Lett. **88** (20 2002) 201801, arXiv: hep-ph/0201206 (cit. on p. 50).

[159] C. Anastasiou and K. Melnikov, *Higgs boson production at hadron colliders in NNLO QCD*, Nucl. Phys. B **646** (2002) 220, arXiv: hep-ph/0207004 (cit. on p. 50).

[160] V. Ravindran, J. Smith and W. L. van Neerven, *NNLO corrections to the total cross-section for Higgs boson production in hadron hadron collisions*, Nucl. Phys. B **665** (2003) 325, arXiv: hep-ph/0302135 (cit. on p. 50).

[161] R. V. Harlander and W. B. Kilgore, *Production of a pseudoscalar Higgs boson at hadron colliders at next-to-next-to leading order*, JHEP **10** (2002) 017, arXiv: hep-ph/0208096 [hep-ph] (cit. on p. 50).

[162] C. Anastasiou and K. Melnikov, *Pseudoscalar Higgs boson production at hadron colliders in NNLO QCD*, Phys. Rev. D **67** (2003) 037501, arXiv: hep-ph/0208115 [hep-ph] (cit. on p. 50).

[163] U. Aglietti, R. Bonciani, G. Degrassi and A. Vicini, *Two-loop light fermion contribution to Higgs production and decays*, Phys. Lett. B **595** (2004) 432, arXiv: hep-ph/0404071 (cit. on p. 50).

[164] R. Bonciani, G. Degrassi and A. Vicini,
On the generalized harmonic polylogarithms of one complex variable,
Comput. Phys. Commun. **182** (2011) 1253, arXiv: 1007.1891 [hep-ph] (cit. on p. 50).

[165] C. Anastasiou et al., *Higgs Boson Gluon Fusion Production Beyond Threshold in N^3LO QCD*,
JHEP **03** (2015) 091, arXiv: 1411.3584 [hep-ph] (cit. on p. 50).

[166] C. Anastasiou et al.,
Soft expansion of double-real-virtual corrections to Higgs production at N^3LO,
JHEP **08** (2015) 051, arXiv: 1505.04110 [hep-ph] (cit. on p. 50).

[167] M. Bonvini, A. S. Papanastasiou and F. J. Tackmann,
Resummation and matching of b-quark mass effects in $b\bar{b}H$ production, JHEP **11** (2015) 196,
arXiv: 1508.03288 [hep-ph] (cit. on p. 50).

[168] M. Bonvini, A. S. Papanastasiou and F. J. Tackmann,
Matched predictions for the $b\bar{b}H$ cross section at the 13 TeV LHC, JHEP **10** (2016) 053,
arXiv: 1605.01733 [hep-ph] (cit. on p. 50).

[169] S. Forte, D. Napoletano and M. Ubiali,
Higgs production in bottom-quark fusion in a matched scheme, Phys. Lett. B **751** (2015) 331,
arXiv: 1508.01529 [hep-ph] (cit. on p. 50).

[170] S. Forte, D. Napoletano and M. Ubiali,
Higgs production in bottom-quark fusion: matching beyond leading order,
Phys. Lett. B **763** (2016) 190, arXiv: 1607.00389 [hep-ph] (cit. on p. 50).

[171] B. C. Allanach, A. Djouadi, J. L. Kneur, W. Porod and P. Slavich,
Precise determination of the neutral Higgs boson masses in the MSSM, JHEP **09** (2004) 044,
arXiv: hep-ph/0406166 (cit. on p. 51).

[172] ATLAS Collaboration, *Search for Heavy Higgs Bosons Decaying into Two Tau Leptons with the ATLAS Detector Using pp Collisions at $\sqrt{s} = 13$ TeV*, Phys. Rev. Lett. **125** (2020) 051801,
arXiv: 2002.12223 [hep-ex] (cit. on pp. 51, 52).

[173] ATLAS Collaboration, *Search for charged Higgs bosons decaying into a top quark and a bottom quark at $\sqrt{s} = 13$ TeV with the ATLAS detector*, JHEP **06** (2021) 145,
arXiv: 2102.10076 [hep-ex] (cit. on pp. 51, 52).

Appendix: Validity of Gaussian approximation of STXS measurements in SMEFT interpretation

The STXS SMEFT interpretation model presented constructs the likelihood function in terms of the fit basis parameters c' from three ingredients:

1. The likelihood function of the STXS measurements, measuring 78 cross-sections parameters, and featuring over a thousand nuisance parameters expressing systematic uncertainties.
2. A specification of the impact of all relevant CP-even Warsaw basis SMEFT operators on the SM predictions of these cross-sections, including acceptance corrections where necessary, *i.e.* Eq. (12), (13), using the coefficients $A_j^{\sigma_{i,k'}}$, $A_j^{\Gamma^{H\to X}}$, $B_{jl}^{\sigma_{i,k'}}$ and $B_{jl}^{\Gamma^{H\to X}}$ as defined in Eq. (8)-(11), and visualised in summary in Figure 5.
3. A rotation matrix from the 50 Warsaw basis parameters $\boldsymbol{c}$, which cannot be unambiguously constrained from the STXS data, to a fit basis $\boldsymbol{c'}$ for which all 19 parameters can be simultaneously constrained from the data, as shown in Figure 8.

An important upside of a likelihood model built this way is that all non-Gaussian effects in the STXS measurements are accounted for, and that the correlated effects of all experimental and theoretical systematic uncertainties are accounted at the level of detail implemented in the original underlying measurements. A downside of this likelihood model is that required complexity of its implementation prevents it from easily being made available.

An alternative likelihood function, based on a multivariate Gaussian approximation of the STXS measurements instead of the full measurement, with an identical SMEFT re-parameterization, can be constructed in a relatively straightforward way from the information provided and represents reasonably good approximation of the full likelihood. A comparison of the results obtained with this simplified Gaussian variant of the likelihood model and those obtained with the full likelihood function is shown in Figure 24 for the linear SMEFT model and in Figure 25 for the SMEFT model including the quadratic terms. Both comparisons indicate general good agreement between expected and observed parameter estimates and their 68% and 95% uncertainty intervals.

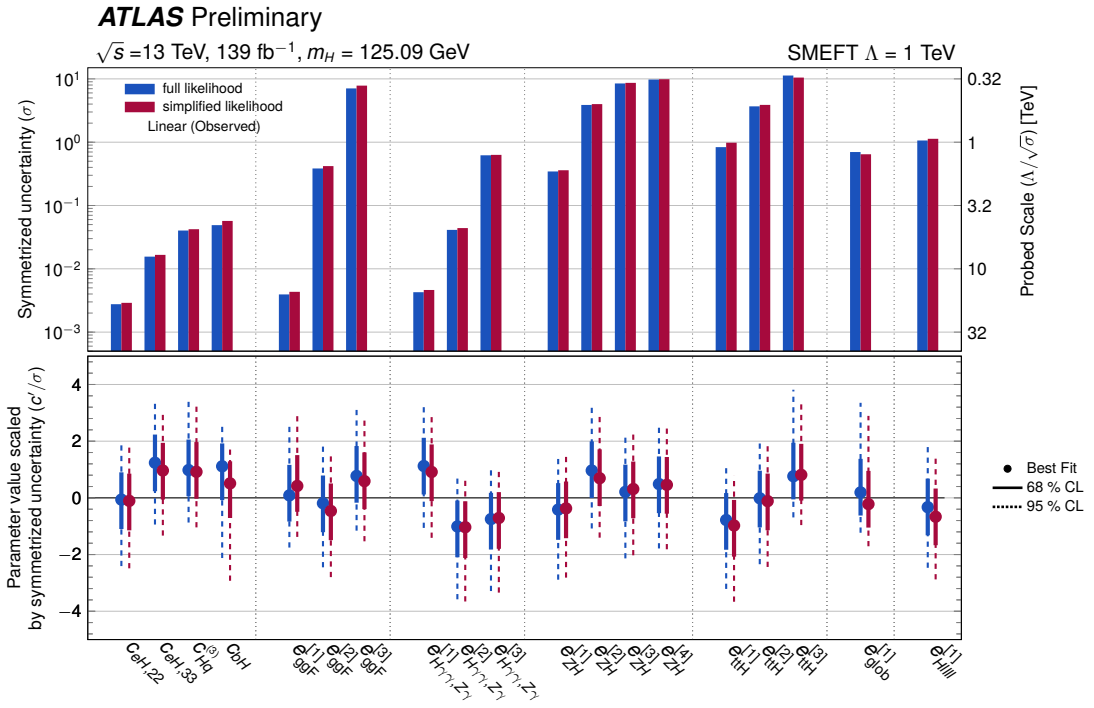

Figure 24: Comparison of the observed result from the full likelihood fit in the SMEFT fit basis with only linear terms (blue) to a fit based on a simplified likelihood constructed from the covariance matrix of the STXS measurements rotated to the same SMEFT fit basis (purple).

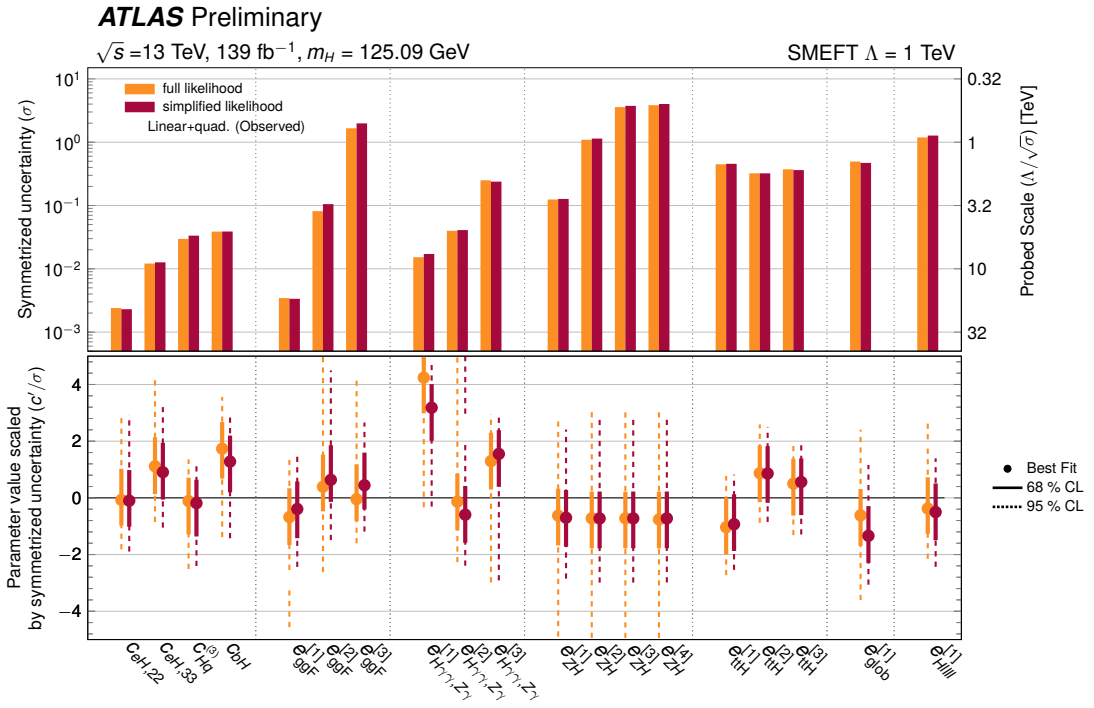

Figure 25: Comparison of the observed result from the full likelihood fit in the SMEFT fit basis with linear and quadratic terms (orange) to a fit based on a simplified likelihood constructed from the covariance matrix of the STXS measurements rotated to the same SMEFT fit basis (dark red).